

A 920 km Optical Fiber Link for Frequency Metrology at the 19th Decimal Place

Dissertation

der Fakultät für Physik
der Ludwig-Maximilians-Universität München



vorgelegt von
Katharina Predehl
aus München

München, den 23.04.2012

Erstgutachter: Theodor W. Hänsch
Zweitgutachter: Christian Lisdat
Tag der mündlichen Prüfung: 08.06.12

Abstract

With residual uncertainties at the 10^{-18} level [1], modern atomic frequency standards constitute extremely precise measurement devices. Besides frequency and time metrology, they provide valuable tools to investigate the validity of Einstein's theory of general relativity, to test a possible time variation of the fundamental constants, and to verify predictions of quantum electrodynamics [2, 3, 3, 4]. Furthermore, applications as diverse as geodesy, satellite navigation, and very long base-line interferometry may benefit from steadily improving precision of both microwave and optical atomic clocks [5].

Clocks ticking at optical frequencies slice time into much finer intervals than microwave clocks and thus provide increased stability. It is expected that this will result in a redefinition of the second in the International System of Units (SI) [6].

However, any frequency measurement is based on a comparison to a second, ideally more precise frequency. A single clock, as highly developed as it may be, is useless if it is not accessible for applications. Unfortunately, the most precise optical clocks or frequency standards can not be readily transported.

Hence, in order to link the increasing number of world-wide precision laboratories engaged in state-of-the-art optical frequency standards, a suitable infrastructure is of crucial importance. Today, the stabilities of current satellite based dissemination techniques using global satellite navigation systems (such as GPS, GLONASS) or two way satellite time and frequency transfer reach an uncertainty level of 10^{-15} after one day of comparison [7]. While this is sufficient for the comparison of most microwave clock systems, the exploitation of the full potential of optical clocks requires more advanced techniques.

This work demonstrates that the transmission of an optical carrier phase via telecommunication fiber links can provide a highly accurate means for clock comparisons reaching continental scales: Two 920 km long fibers are used to connect MPQ (Max-Planck-Institut für Quantenoptik, Garching, Germany) and PTB (Physikalisch-Technische Bundesanstalt, Braunschweig, Germany) separated by a geographical distance of 600 km. The fibers run in a cable duct next to a gas pipeline and are actively compensated for fluctuations of their optical path length that lead to frequency offsets via the Doppler-effect. Together with specially designed and remotely controllable in-line amplification this enables the transfer of an ultra-stable optical signal across a large part of Germany with a stability of 5×10^{-15} after one second, reaching 10^{-18} after less than 1000 seconds of integration time. Any frequency deviation induced by the transmission can be

constrained to be smaller than 4×10^{-19} .

As a first application, the fiber link was used to measure the 1S-2S two photon transition frequency in atomic hydrogen at MPQ referenced to PTB's primary Cs-fountain clock (CSF1) [8, 9]. Hydrogen allows for precise theoretical analysis and the named transition possesses a narrow natural line width of 1.3 Hz. Hence, this experiment constitutes a very accurate test bed for quantum electrodynamics and has been performed at MPQ with ever increasing accuracy. The latest measurement has reached a level of precision at which satellite-based referencing to a remote primary clock is limiting the experiment. Using the fiber link, a frequency measurement can be carried out directly since the transmission via the optical carrier phase provides orders of magnitude better stability than state-of-the-art microwave clocks.

The achieved results demonstrate that high-precision optical frequency dissemination via optical fibers can be employed in real world applications. Embedded in an existing telecommunication network and passing several urban agglomerations the fiber link now permanently connects MPQ and PTB and is operated routinely. It represents far more than a proof-of-principle experiment conducted under optimized laboratory conditions. Rather it constitutes a solution for the topical issue of remote optical clock comparison. This opens a variety of applications in fundamental physics such as tests of general and special relativity as well as quantum electrodynamics. Beyond that, such a link will enable clock-based, relativistic geodesy at the sub-decimeter level. Further applications in navigation, geology, dynamic ocean topography and seismology are currently being discussed. In the future, this link will serve as a backbone of a Europe-wide optical frequency dissemination network.

Zusammenfassung

Moderne Atomuhren haben relative Unsicherheiten von wenigen 10^{-18} in der Frequenz erreicht [1]. Damit werden sie zu unschätzbaren Hochpräzisionswerkzeugen zur experimentellen Untersuchung fundamentaler Fragen der Physik, wie zum Beispiel der Überprüfung von Einsteins Allgemeiner Relativitätstheorie, der Suche nach einer möglichen Drift der Naturkonstanten, oder der Validierung der theoretischen Voraussagen der Quantenelektrodynamik [2, 3, 3, 4]. Darüber hinaus profitieren noch viele weitere Anwendungen von der ständig wachsenden Präzision optischer sowie Mikrowellen-Atomuhren. Die prominentesten Vertreter sind hier sicherlich die Satellitennavigation, die Geodäsie und die astronomische Radiointerferometrie [5].

Optische Uhren zerteilen Zeitintervalle in wesentlich kleinere Untereinheiten, als es Mikrowellenuhren können. Sie sind daher intrinsisch wesentlich stabiler. Das hat unter anderem die Frage aufgeworfen, ob und wie die SI-Sekunde basierend auf einer optischen Primär-Referenz neu definiert werden kann [6].

Aufgrund dieser extrem hohen Stabilität können optische Uhren nur direkt aufeinander referenziert werden und eine Bestimmung ihrer Frequenz in absoluten Einheiten von Hertz ist nur unter großem Genauigkeitsverlust möglich. Leider gibt es zum heutigen Zeitpunkt noch keine transportablen optischen Uhren.

Um die wachsende Anzahl weltweiter Präzisions-Experimente miteinander zu vernetzen, ist eine geeignete Infrastruktur daher von größter Wichtigkeit. Für Uhrenvergleiche im Mikrowellenbereich wird traditionell Zwei-Wege-Übertragung per Satellit (TWSTFT) verwendet. Diese Übertragungsmethode erreicht relative Unsicherheiten von wenigen 10^{-15} nach einem Tag Mittelungszeit [7]. Damit ist sie für den Vergleich optischer Uhren nicht anwendbar.

Als vielversprechende Alternative wurden vor ein paar Jahren Glasfasernetzwerke als Übertragungsmedium vorgeschlagen, die normalerweise unter der Erde (und damit weitgehend isoliert von Umwelteinflüssen) vergraben sind. Das wurde inzwischen auf Teststrecken von bis zu 480 km erfolgreich experimentell untersucht. Um zu überprüfen, ob dieser Ansatz auch über weitere Entfernungen realisierbar ist, haben das Max-Planck-Institut für Quantenoptik (MPQ) in München und die Physikalisch-Technische Bundesanstalt (PTB) in Braunschweig eine 920 km lange Glasfaserverbindung zwischen den beiden Instituten aufgebaut. Aktive Rauschkompensation sowie fernsteuerbare optische Verstärkereinheiten entlang der Faserstrecke erlauben die Übertragung einer schmalbandigen optischen Frequenz mit einer relativen Instabilität von 5×10^{-15} in einer Sekunde,

die in weniger als 1000 Sekunden zu 10^{-18} mittelt. Jede mögliche systematische Abweichung vom übertragenen Frequenzwert konnte auf kleiner 4×10^{-19} limitiert werden.

Als erste Anwendung wurde der Link erfolgreich für die Präzisionsspektroskopie an atomarem Wasserstoff eingesetzt [8]. Die Frequenzmessung wurde am MPQ durchgeführt, war jedoch über den Link auf die primäre Cäsiumatomuhr der PTB referenziert[9].

Diese Ergebnisse werden den Anforderung an eine optische Präzisionsmessung zwischen zwei fast 1000 km entfernten Forschungsinstituten absolut gerecht. Der Faserlink, der sich quer durch einen großen Teil Deutschlands zieht und dabei mehrere Großstädte passiert, stellt damit mehr als ein Modellversuch dar, der unter optimalen Laborbedingungen unternommen wurde und bietet eine Lösung für das hochaktuelle Problem optischer Uhrenvergleiche. Dies ermöglicht eine Reihe von Anwendungen in der Fundamentalphysik, aber auch in angewandten Gebieten wie der Geologie, Ozeanographie und in der Erdbebenforschung. In Zukunft wird der Link als erstes großes Teilstück eines Europäischen Frequenzmetrologie- Netzwerkes eingesetzt werden.

Contents

1	Introduction: High Precision Clocks - not only for Timekeeping	7
2	State-of-the-art Frequency Standards	11
2.1	Clock Characterization	11
2.1.1	Stability	12
2.1.2	Accuracy	15
2.1.3	Measuring Phase and Frequency Noise	15
2.1.4	Phase Noise Measurements	18
2.2	Microwave Frequency Standards	18
2.2.1	Cesium Atomic Clocks	19
2.2.2	Masers	20
2.2.3	Novel Developments	21
2.3	The Latest Generation: Optical Clocks	21
2.3.1	Neutral Atom Clocks	22
2.3.2	Single Ion Clocks	23
2.4	Clocks in Research and in Everyday Life	24
2.4.1	Realization of the SI-second and UTC	24
2.4.2	Geodesy	25
2.4.3	Fundamental Constants and Cosmology	26
3	Long-haul Time and Frequency Dissemination	29
3.1	Satellite-based Techniques	29
3.1.1	Global Navigation Satellite System	29
3.1.2	Two-way Time and Frequency Transfer	30
3.1.3	Limitations	31
3.2	Transportable Atomic Clocks	33
3.3	Fiber based Frequency Dissemination	33
3.3.1	Transmission of Amplitude Modulated cw-Lasers of up to 86 km	34
3.3.2	Transmission of Pulsed Lasers of up to 50 km	35
3.3.3	Transmission of the Optical Phase of up to 480 km	35

4	Two 920 km Optical Fiber Links for Frequency Metrology	37
4.1	Transmission Scheme	37
4.2	Frequency Comb Systems	37
4.3	Transfer Laser Systems	39
4.3.1	Vertical Cavity Design: MPQ System	40
4.3.2	Horizontal Cavity Design: Transportable PTB System	41
4.4	Two 920 km Fibers connecting MPQ and PTB	43
4.5	Active Fiber Noise Cancellation	46
4.5.1	Noise Origins	46
4.5.2	Stabilization Scheme	47
4.6	Signal Amplification	49
4.6.1	Erbium doped amplifiers	49
4.6.2	Fiber Brillouin Amplifiers	52
4.6.3	Optical Remote Control	53
5	Optical Frequency Transmission over 920 km with 10^{-19} Uncertainty	55
5.1	Characterizing Test Links of up to 500 km	55
5.1.1	2m Link: Fiber Stabilization Noise Floor	55
5.1.2	10 km Link to Garching Computing Center	57
5.1.3	50 km Link around Braunschweig	58
5.1.4	146 km Link from PTB to University of Hanover and back	59
5.1.5	172 km Link from MPQ to Münchsmünster Repeater Station and back	60
5.1.6	480 km Link from PTB to LUH to PTB to Cörmigk Repeater Station and back	61
5.1.7	512 km Link from MPQ to University of Erlangen	62
5.2	Characterizing the Full 920 km Distance	63
5.2.1	Setup	63
5.2.2	Un-stabilized Link	63
5.2.3	Antiparallel Configuration	64
5.2.4	Parallel Configuration: Fiber Noise Correlation	69
5.2.5	Phase Noise Measurements	71
5.3	Discussion	72
6	Precision Spectroscopy on Atomic Hydrogen Referenced to a 600 km distant Frequency Standard	75
6.1	1S-2S Absolute Frequency Measurement	75
6.1.1	Experimental Setup	76
6.1.2	Uncertainty Budget	78
6.1.3	Results May 2010	78
6.2	1S-2S Absolute Frequency Measurement in Units of CSF1 at PTB	78

6.2.1	Frequency Map	78
6.2.2	Results November 2010	80
6.3	Testing Electron Boost Invariance with 1S-2S Hydrogen Spectroscopy . .	81
6.4	Discussion	82
7	Conclusion & Outlook	83
A	Signal Statistics	85
A.1	Signal Statistics in the Time Domain	86
A.2	Noise Sources	87
A.2.1	White Phase Noise (h_{-3})	87
A.2.2	Flicker Phase Noise (h_{-2})	87
A.2.3	White Frequency Noise (h_{-1})	88
A.2.4	Flicker Frequency Noise (h_0)	88
A.2.5	Random Walk of Frequency (h_1)	88
A.3	Signal Statistics in the Frequency Domain	88
A.4	Conversion from Time Domain to Frequency Domain	89
B	Optical Frequency Measurements	91
B.1	Optical Heterodyne Beat Detection	91
B.1.1	Optical Beat Notes	91
B.1.2	Signal-to-Noise Ratio	92
B.1.3	Measuring Weak Signals with a Strong Local Oscillator	93
B.1.4	Self-Heterodyne Beat Detection	94
B.2	Femtosecond Frequency Combs	95
C	Basics of Phase-locked Loops	97
D	Laser Stabilization: Pound-Drever-Hall Technique	99
E	Fiber Noise Cancellation: Phase-Locked-Loop with Delay	103
E.1	Delay Unsuppressed Fiber Noise	103
E.2	Loop Filter Design	106
	Bibliography	109
	List of Publications	122
	Acknowledgments	127

Chapter 1

Introduction: High Precision Clocks - not only for Timekeeping

In 1936, physicists from the Physikalisch-Technische-Reichsanstalt published the result of a two-year measurement that for a long time was strongly challenged by the community. They confirmed their results in 1950 and finally concluded [10, 11]:

“Thereby we observe that Earth in summer is up to 0.12 sec slow compared to the mean quartz clock.”

Their measurements proved that the duration of the day varies during one year on average by 30 ms caused by seasonal changes of the Earth’s moment of inertia. Its accuracy was thus measured to be limited to 10^{-8} . The sensational aspect about this measurement lies in the fact that the the solar day back then was used to define the second. For the first time, scientists faced the situation having developed a clock that was better than the actual definition of the unit of time.

Shortly after the invention of quartz clocks, atomic hyperfine transitions were suggested as atomic clocks that gave a much more stable timing signal as compared to the solar



second [12]. Immediately after the first demonstration at the National Physics Laboratory (NPL) in England in 1955 [13] cesium atomic clocks became widely accepted as master references in research institutes across the world.

Consequentially, the SI second was defined at the Thirteenth General Conference on Weights and Measures in 1967 as follows [14]:

The second is the duration of 9 192 631 770 periods of the radiation corresponding to the transition between the two hyperfine levels of the ground state of the cesium 133 atom.

Since then, the SI-second has become the most accurately realized physical unit. However, optical atomic clocks nowadays surpass the performance of cesium clocks (and hence the SI unit Hertz) by far and the current situation is similar as in the first half of the last century. However, to date a variety of optical clock systems has been developed based on different atom species, such as strontium, ytterbium, mercury, and aluminum [15, 16, 3, 1] based on trapped ions or on a large number of neutral atoms stored in an optical lattice. All of them have assets and drawbacks and the final decision of which optical clock is the most appropriate candidate has not been made. It will need mutual comparison between those clock systems in order to evaluate suited candidates for a next generation of optical primary time standards. As a result, this requires novel time and frequency dissemination techniques.

The present work provides extensive documentation of the establishment and characterization of a 920 km long purely optical fiber link adapted for the demands of optical clock comparison.

It gives an overview of state-of-the art frequency standards (Chapter 2) and of currently used frequency dissemination techniques (Chapter 3). The limitations of satellite-based schemes are discussed to clearly demonstrate the need of the novel fiber-based concepts.

Chapter 4 describes the experimental setup of the 920 km fiber link. Its characterization is examined and discussed in Chapter 5: Test links from 2 m to up to 500 km have been investigated before setting up and characterizing the whole link length.

As a first application, the link was used to perform high-precision spectroscopy of atomic hydrogen referenced to a 600 km distant cesium clock (Chapter 6). The results of the measurements allowed new boundaries to be set on the Lorentz electron boost invariance violation as postulated by the Standard Model Extension Theory.

Within the framework of this dissertation the following tasks have been performed:
The conditions for the 920 km fiber connection between the Max-Planck-Institute of

Quantum Optics (MPQ) and the Physikalisch-Technische Bundesanstalt (PTB) were negotiated with the German Research network *DFN* and the fiber provider *Gasline GmbH*. Together with PTB, numerous test links were established and characterized. At MPQ, the in-line amplifiers were conceived, developed, and deployed along the link. In collaboration with Menlo Systems GmbH, the amplifier remote control were designed, tested and implemented. Both groups at MPQ and PTB have established the full 920 km fiber connection step-by-step and extensively characterized. For the hydrogen measurement, the referencing of the MPQ H-maser to PTB's cesium fountain via the link has been assured and the corresponding data have been analyzed. This also included the coordination of the involved experiments.



Chapter 2

State-of-the-art Frequency Standards

Modern atomic clocks constitute extremely precise measurement devices that allow for an exhaustive investigation of fundamental questions of physics. To name a few examples, temporal or spatial drifts of the natural constants, the validity of Einstein's theory of general relativity, or the verification of theoretical predictions as given by quantum electrodynamics can be explored [2, 3, 4]. Moreover, atomic clocks have found wide applications in many aspects of our personal lives.

A relatively new generation of clocks based on optical atomic transitions can slice time into tiny intervals of a few tens of femtoseconds. Hence, they provide the potential for a dramatically increased frequency stability as compared to microwave clocks. Additionally, today's optical clock systems have reached relative uncertainties of less than 10^{-17} - a level at which height differences of less than one meter between two optical clocks become measurable due to the gravitational red shift [2]. A redefinition of the SI-second based on an optical transition frequency is expected to happen to account for this development in the near future [6].

2.1 Clock Characterization

A clock is comprised of a stable oscillator and a device to count the oscillator's cycles. Naturally, it can be used to generate a timing or a frequency signal. As stated before, the SI-second is defined as the duration of a well-defined number of cycles of the ground state hyperfine transition in cesium. Therefore, it is directly coupled with the atom's transition frequency $\nu(t)$. Even in the most advanced clock systems, this frequency is not constant in time but fluctuates by $\Delta\nu(t)$. It may further be shifted by $\Delta\nu_{shift}$ from its unperturbed value ν_0 due to systematic effects.

Not only the clock signal itself, but also many devices to generate or distribute it are based on frequency generation and -synthesis. Their performance relies on the local oscillators involved which are used to transform the signal of interest into a different frequency. In order to characterize and compare all these oscillators that usually operate at different frequencies, it is convenient to define the normalized frequency deviation $y(t)$:

$$y(t) = \frac{\Delta\nu(t) + \Delta\nu_{shift}}{\nu_0} = \frac{1}{2\pi\nu_0} \frac{d\varphi(t)}{dt} \quad (2.1)$$

with $\varphi(t)$ being the signal's instantaneous phase. $\Delta\nu_{shift}$ limits the oscillator's accuracy while $\Delta\nu(t)$ determines its stability. The mathematical formalism to describe both is given in the following sections (for a comprehensive description refer, for example to [17] pp. 47).

2.1.1 Stability

Time Domain: Allan Standard Deviation

Frequency fluctuations arise in various characteristics and may be caused either by broadband white noise or slower flicker noise (see also Appendix A). They determine the statistical uncertainty of the signal as a function of the averaging time τ . The residual frequency instability is commonly expressed by the *Allan Standard Deviation* $\sigma_y(\tau)$ (ADEV) [18]:

$$\sigma_y^2(2, \tau) = \frac{1}{2} \langle (\bar{y}_1(t) - \bar{y}_2(t))^2 \rangle \quad (2.2)$$

with the samples $\bar{y}_i(t)$ being the mean frequency deviations for different averaging times τ . To obtain a better confidence for long averaging times, one usually chooses the pairs to overlap [19]. The ADEV can be interpreted as the mean square of linearly filtered frequency fluctuations using different filter bandwidths that decrease with τ .

To illustrate this time-dependent signal filtering, Eq.2.2 can be re-written as:

$$\sigma_y(\tau) = \sqrt{\left\langle \left(\int_{-\infty}^{\infty} y(t') h(t-t') dt' \right)^2 \right\rangle} \quad (2.3)$$

2. State-of-the-art Frequency Standards

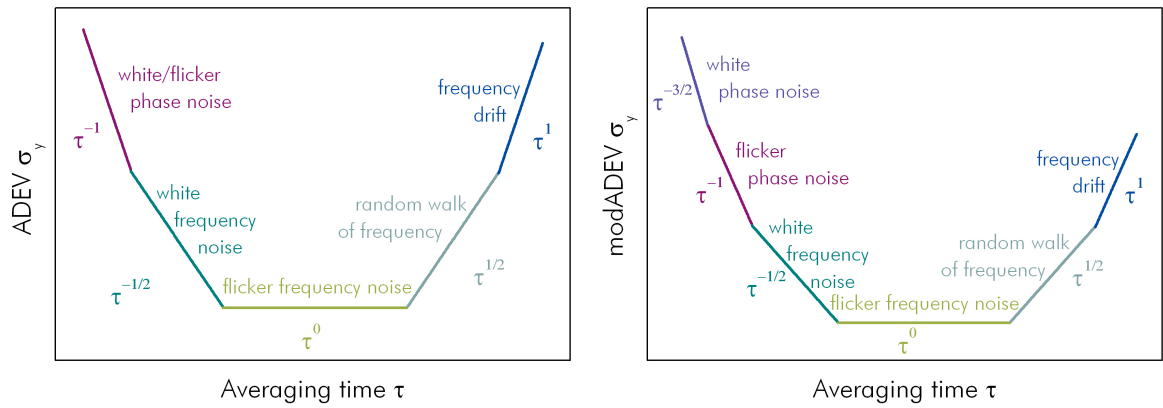


Figure 2.1: a) τ -dependence of the Allan deviation $\sigma_y(\tau)$. White phase noise is not distinguished from flicker phase noise. b) The modified Allan deviation allows for an unambiguous noise analysis as shown in b).

by introducing a filter function $h(t)$:

$$h(t) = \begin{cases} -\frac{1}{\sqrt{2}\tau} & \text{for } -\tau < t < 0 \\ \frac{1}{\sqrt{2}\tau} & \text{for } 0 \leq t < \tau \\ 0 & \text{otherwise} \end{cases} \quad (2.4)$$

The ADEV shows a characteristic τ -dependence for most contributing noise types (see Fig.2.1a) and Tab.2.1). However, it is ambiguous for flicker phase noise and white phase noise (both $\propto \tau^{-1}$). In order to overcome this deficiency, a modified ADEV with a higher sensitivity to white phase noise has been suggested [20]. It is calculated analogously to Eq.2.3 but features a triangular rather than a constant weighting function [17]:

$$h_{mod}(t) = \begin{cases} -\frac{1}{\sqrt{2}\tau^2}t & \text{for } 0 < t \leq \tau \\ \frac{1}{\sqrt{2}\tau^2}(2t - 3\tau) & \text{for } \tau < t \leq 2\tau \\ -\frac{1}{\sqrt{2}\tau^2}(t - 2\tau) & \text{for } 2\tau < t \leq 3\tau \\ 0 & \text{otherwise} \end{cases} \quad (2.5)$$

This is equivalent to performing an overlapping moving average over increasing time intervals τ . Other than the standard ADEV, the modADEV averages as $\tau^{-3/2}$ for white phase noise and as τ^{-1} for flicker phase noise (see Fig.2.1b)). Thus it provides more comprehensive information about the oscillator's noise as compared to the ADEV.

Frequency Domain: Phase Spectral Density

In order to obtain more detailed information about fast frequency noise it can be more convenient to analyze the oscillator signal in the frequency domain than in the time domain. This clearly reveals the Fourier frequencies at which the noise arises and gives a hint of the noise source (for example 50/60 Hz spikes originating from electronic ground loops or characteristic laser intensity noise peaks at several kHz).

The common measures to characterize phase or frequency fluctuations in the Fourier domain are the corresponding power spectral densities $S_\varphi(f)$ and $S_y(f)$ (PSD). They are given by the amount of phase (or frequency) noise power that spreads into the signal's Fourier sidebands:

$$S_\varphi(f) = |\tilde{\varphi}(f)|^2 \quad (2.6)$$

with $\tilde{\varphi}(f)$ being the Fourier transform of the signal's phase $\varphi(t)$ and

$$S_y(f) = \frac{f^2}{\nu_0^2} S_\varphi(f) \quad (2.7)$$

Eqs.2.6 and 2.7 are both commonly expressed in units of rad^2/Hz .

Conversion from Frequency to Time Domain

As derived in Appendix A the Allan deviation $\sigma_y(\tau)$ and the power spectral density $S_y(f)$ are related by

$$\sigma_y(\tau)^2 = \int_{-\infty}^{\infty} S_y(f) \frac{\sin^4(\pi\tau f)}{(\pi\tau f)^2} df \quad (2.8)$$

Hence, the Allan deviation can be interpreted as the temporal response of the accordingly filtered PSD. Similar to $\sigma_y(\tau)$, $S_y(f)$ exhibits a frequency dependence characteristic to the noise process (Tab.(2.1)).

Noise process	Origin	$\sigma^2(\tau)$	$S_y(f)$
Random walk of frequency noise	Environmental perturbations	$\propto \tau^1$	$\propto f^2$
Flicker frequency noise	Resonators	const.	$\propto f$
White frequency noise	Shot noise, Thermal noise	$\propto \tau^{-1}$	const.
Flicker phase noise	Electronics	$\propto \tau^{-2}$	$\propto f^{-1}$
White phase noise	Environmental perturbations	$\propto \tau^{-2}$	$\propto f^{-2}$

Table 2.1: *Noise sources (see also Appendix A) and corresponding τ -dependence of $\sigma^2(\tau)$ and f -dependence of $S_y(f)$.*

2.1.2 Accuracy

Though high stability is required in order to reduce the statistical uncertainty, the systematic uncertainty is the key characteristic of any oscillator. It states an upper limit for the oscillator’s accuracy and is determined by systematic effects that may be of technical origin or of fundamental nature (for examples see the next section) [21]. Together with the statistical uncertainty, all effects are summed up in quadrature to estimate the system’s total uncertainty. The single contributions are often listed in an uncertainty budget.

2.1.3 Measuring Phase and Frequency Noise

Time Domain: Frequency Counters

Time traces of frequency data are taken with electronic frequency counters. Here, the phase of the input signal is compared to a reference phase for a certain time interval, the gate time τ_{gate} . From the number of (not necessarily full) cycles the frequency value is calculated (see Fig.2.2).

Some counters exhibit dead time between two subsequent gate time windows. This results in loss of phase-coherence and should be avoided if continuous phase information is required [22].

The way the frequency counter internally processes the data can have a strong impact on the frequency resolution [23]. This especially affects the appearance of the signal stability. A frequency counter can be considered as a Π -type estimator if the signal is processed as described above without internal averaging. Using a Π -type counter, calculating the frequency stability according to Eq.2.2 gives the standard Allan deviation $\sigma_y(\tau)$ as described in Section 2.1. This holds only provided that there is no dead time between two measurement windows.

Some types of counters internally average the input signal to provide advanced frequency

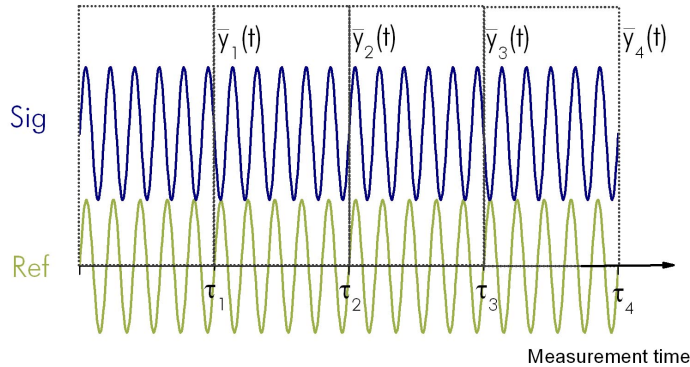


Figure 2.2: *Measurement principle of frequency counters: the signal's phase is compared to a reference phase. Frequency values \bar{y}_i are obtained by calculating phase differences $(\varphi_{i+1} - \varphi_i)/\tau$. The determination of φ_i depends on the type of counter and can be a non-weighted (Π -type) average or a weighted (Λ -type) average of the intermediate phase measurements.*

resolution. One very common averaging method can be approximated by an overlapping triangular weighting function that led to the denotation Λ -type counter. These counters sample the data with a given rate and measure many frequency intervals within one gate window. These values are averaged over the gate time with a filter function similar to Eq.2.5. Hence, applying Eq.2.2 to the frequency output of a Λ -type counter rather gives the modified Allan deviation than the regular ADEV. Other types of averaging can be reviewed in [23].

Of course, both Π -type and Λ -type counters deliver the same mean frequency. Moreover, if the gate time of the Π -counter is set equal to the sampling intervals of the Λ -counter the delivered data are exactly the same. The response is different only to high frequency noise components, i.e. if $f \gg 1/\tau_{gate}$ [23].

Cycle Slips

Frequency counting and frequency stabilization requires minimum signal-to-noise ratios (SNR) and power levels to correctly process the signal. For instance, digital phase comparators only work properly with an SNR must greater than 30 dB and an power level that exceeds -20 dB. Analog mixers often require power levels of 0 dB (LO -input) and -7 dB (IR -input).

If the signal amplitude drops below detection threshold, the counter has lost at least one cycle and thus phase coherence. This is denoted as cycle-slip (CS). In this case, the counter will return an arbitrary frequency value.

The accuracy of high precision measurements can strongly be limited by unidentified cycle-slips hidden in the signal's noise band. Further, as phase coherence gets lost, the data get statistically independent which changes the τ -dependence of the Allan deviation from τ^{-1} to $\tau^{-1/2}$ which increases the measurement time. One example how

2. State-of-the-art Frequency Standards

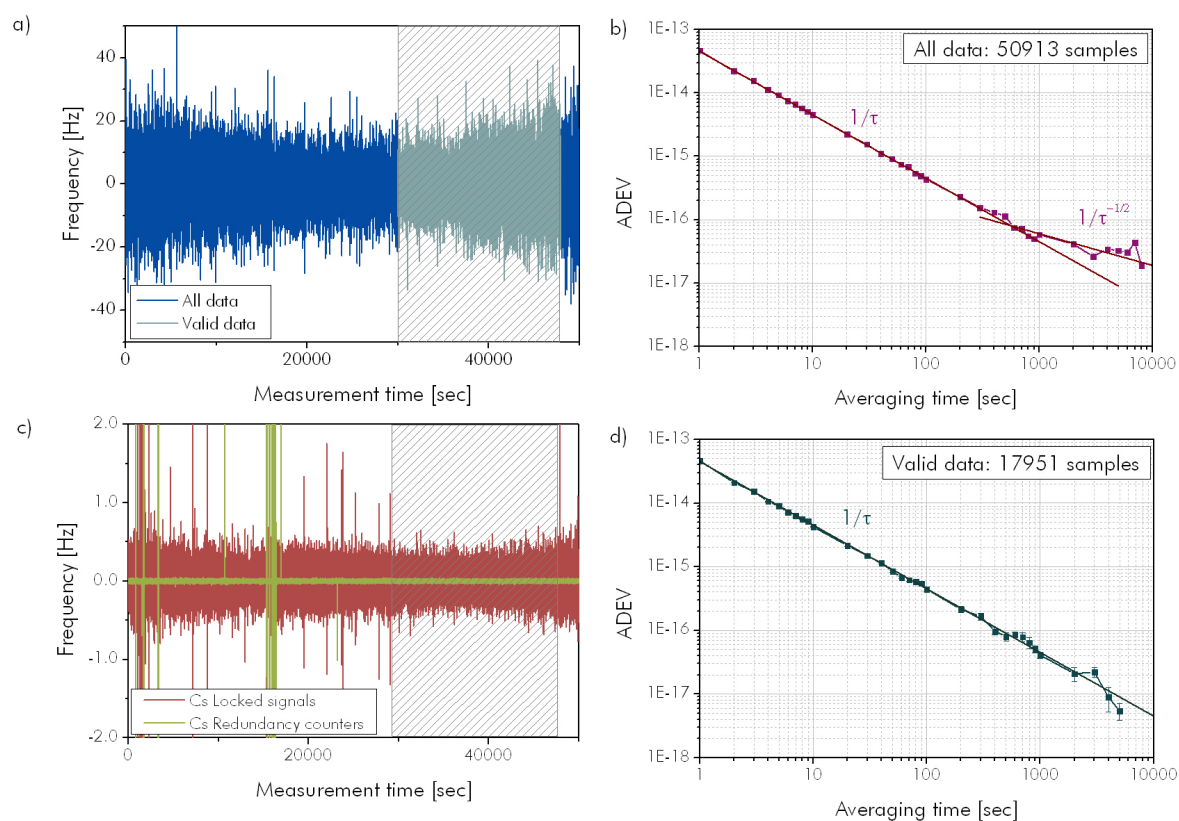


Figure 2.3: *Cycle - slip detection: a) Time trace of a phase locked signal, normal operation. b) Corresponding ADEV showing a bend-off after ~ 500 s. c) Cycle-slip detection as described in the text identifies the actual region of proper operation. d) Corresponding ADEV- no deviation from the expected τ^{-1} slope.*

unidentified cycle-slips may affect the Allan deviation is illustrated in Fig.2.3 showing frequency fluctuations of a phase-locked signal as routinely measured in the link experiment. Fig.2.3a) suggests normal operation, but the corresponding Allan deviation indicates noise other than white phase noise (see Fig.2.3b)). Cycle-slip detection as described below reveals numerous losses of phase coherence and limits the region of continuous valid data to about one third of the original trace (Fig.2.3c)). Within this region, the Allan deviation falls off as expected for a properly phase-locked signal (Fig.2.3d)).

To unambiguously distinguish between real signal spikes and cycle-slips, redundant counting is mandatory. Here, the detection arm is split in front of the first comparator and the same signal is counted on at least two channels. Disagreeing data are discarded. The threshold at which data are considered to be corrupted may be determined according to the required accuracy. Phase-locked signals are usually compared to their nominal value as this takes into account that also the phase-locked loop may lose cycles [24].

2.1.4 Phase Noise Measurements

Experimentally, the power spectral density (PSD) $S_\varphi(f)$ is determined by measuring the time dependent phase fluctuations and performing a Fast Fourier Transform (FFT) analysis. This can be performed using a sampling oscilloscope, or a vector voltmeter. Some rf- spectrum analyzers provide a phase-noise measurement option that automatically performs the FFT analysis.

However, what is actually measured are voltage fluctuations rather than phase fluctuations. Phase comparators as described in Appendix C translate phase into voltage according to:

$$V_{PD} = K_{PD} \cdot (\varphi(t) - \varphi_{ref}(t)) \quad (2.9)$$

by comparing the input phase to a reference phase. The resolution of the recording device may require pre-scaling by a factor K_{PS} of the input phase such that fluctuations can be resolved well within one cycle. This can either be done by choosing the conversion coefficient K_{PD} small or by dividing the input and the reference frequencies by the same factor.

The resulting PSD is then given by:

$$S_\varphi(f) = \frac{[\mathcal{FFT}(V_{PD}/(K_{PD} \cdot K_{PS}))]^2}{BW} \quad (2.10)$$

taking into account the recording bandwidth BW .

2.2 Microwave Frequency Standards

Today, cesium atomic clocks are firmly established not only in research but also in every day life. Another microwave frequency standard comprises rubidium gas cells [26]. Stable local oscillators such as active hydrogen masers and novel systems such as cryogenic sapphire oscillators or stable microwave generation using femtosecond frequency combs are helpful tools for microwave frequency comparisons or distribution.

2.2.1 Cesium Atomic Clocks

Cesium clocks operate by interrogating the ground-state hyperfine splitting of the ^{133}Cs isotope. Most of today's established commercial systems make use of Ramsey spectroscopy [27] on a thermal beam of Cs atoms. The setup of a thermal Cs beam clock is depicted in figure Fig.2.4 and can further be reviewed in [25, 28].

In clock operation, the center of the cavity tuning frequency is stabilized to the 9 192 631 770 Hz resonance frequency thus maximizing the signal current. The signal is used to steer a quartz-based local oscillator that generates the physical clock signal at a frequency between 1 Hz and 100 MHz. Thermal beam Cs clocks can reach stabilities of 8×10^{-14} after one hour and a residual uncertainty of 8×10^{-15} [29].

The so-called fountain clocks are comprised of complex experimental setups and are mostly employed in scientific environments. Here, the thermal beam is replaced by a laser-cooled cloud of atoms that is vertically tossed upwards and then dropped in gravity [30, 31]. The scheme is shown in figure Fig.2.5. The spectroscopy zone comprises the area between the microwave cavity and the top reversal point. This strongly increases the interrogation time and yields a better line resolution.

With this approach, Cs-fountain clocks have reached uncertainties in the lower 10^{-16} level with different clock systems showing similar performance [33, 34, 35]. Next generations of Cs-fountains hold the prospect of reaching accuracies on the level of 1×10^{-16} [28, 36]. The best short-term stability has been reported to be $4 \times 10^{-14} \text{s}^{-1/2}$ [37] (see Fig.2.7).

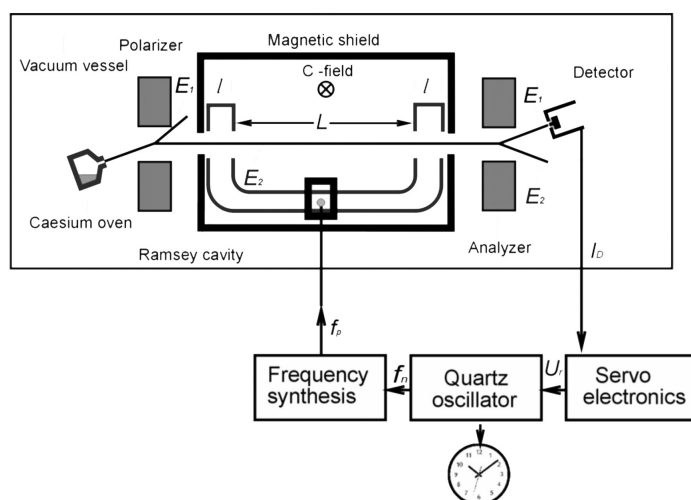


Figure 2.4: Schematic setup of a thermal beam cesium atomic clock. Due to atom velocities of ~ 100 m/s the line width of the transition is strongly broadened by the time of flight and thus inversely depends on the interrogation time. Therefore, Ramsey spectroscopy is applied for atom interrogation. Courtesy of A. Bauch [25].

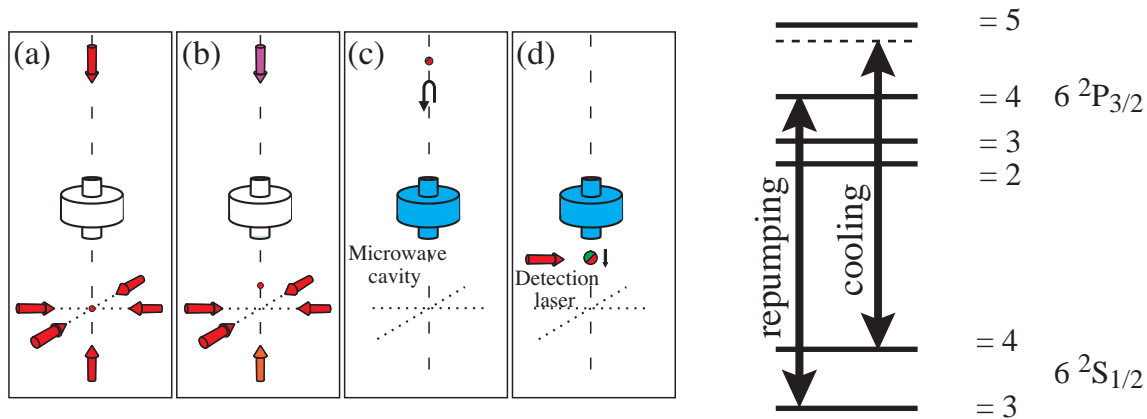


Figure 2.5: *The four cycling stages of interrogating the clock transition in a Cs fountain. a) Laser cooling to sub μK . b) Launching the atoms by slightly detuning the vertically directed laser beams. c) Switching off the lasers at an atom speed of about 4 m/s: the atoms escape vertically. Preparation of the clock state by a short microwave pulse. The Ramsey spectroscopy zone is passed twice on the atoms' flight in gravity. d) Detection of excited atoms measuring fluorescence light at 852.1 nm with subsequent de-excitation. Re-pumping and cooling as in a) (right view: level scheme) Courtesy of R. Wynands [32].*

2.2.2 Masers

A maser produces microwaves by amplified stimulated emission of radiation inside a resonator. The most commonly employed devices operate on a ground state hyperfine transition in atomic hydrogen having a frequency of 1 420 405 752 Hz. The scheme is shown in Fig.2.6 and can further be reviewed in [17] pp. 229.

The short-term stability of typically 10^{-13} after 1s is determined by white phase noise

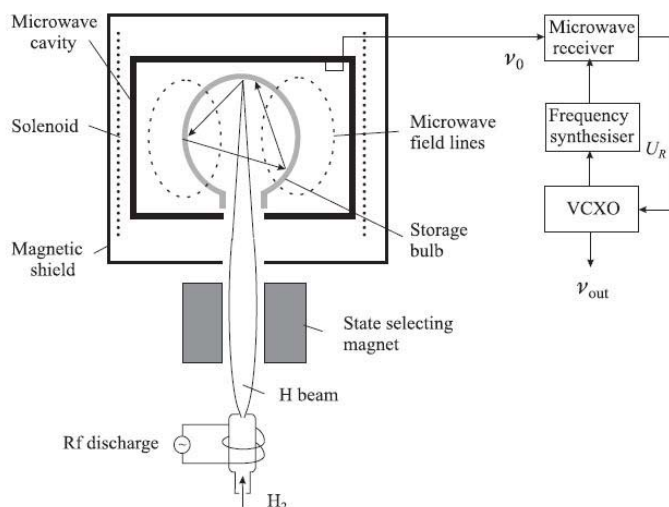


Figure 2.6: *Scheme of a hydrogen maser: H_2 -molecules are dissociated inside an rf- discharge tube to form atomic hydrogen. A magnetic state selector filters the atoms in the $F = 1$, $m_f = 0$ state that afterwards enter a microwave cavity tuned to the 1.42 GHz resonance. The radiation is used to tune a voltage controlled oscillator to generate the actual frequency output.*

due to length fluctuations of the cavity. For medium-term time scales thermal radiation causes a dominant white frequency noise contribution together with a flicker floor below 10^{-15} . For long time scales, the instability increases again as the cavity drifts. The overall stability can be significantly improved in cryogenic temperature environments.

2.2.3 Novel Developments

Cryogenic Sapphire Oscillators

Cryogenically cooled sapphire exhibits extraordinary low loss for microwave radiation. Given a suited geometry, it supports certain whispering gallery modes with high Q-factors $Q = \nu_0/\Delta\nu$ of about one billion. Together with the existence of a minimum around 4 K in the frequency-temperature dependence, this makes sapphire perfectly suited as resonator material in cryogenic sapphire oscillators (CSO) for microwave synthesis with very high frequency stability. An extended description about their functionality can be found in [38]. Among all of today's microwave standards, CSOs show the best short-term stability of below 10^{-15} after a few tens of seconds before a slow drift of 5×10^{-14} per day sets in [39].

Stable Microwave Generation Using Femtosecond Frequency Combs

Optical modes with Q-factors of 10^{11} can be excited in high-finesse Fabry-Pérot resonators. Stabilizing a continuous wave (c.w.) laser to such a cavity mode yields an optical frequency signal that can have a relative instability in the lower 10^{-16} range for averaging times up to 10 s [40] (see also Appendix 2.1.3). Femtosecond frequency combs can be used to divide this stable frequency output from the optical to the radio-frequency domain to derive a stable microwave source. Here, the short-term stability is comparable to those of the best cryogenic sapphire oscillators but can be achieved at room temperature (see e.g. [41]).

2.3 The Latest Generation: Optical Clocks

As most systematic shifts are independent from the transition frequency, optical atomic clocks having frequencies of several hundred THz hold the prospects to reduce the fractional residual frequency uncertainty $\Delta\nu_{shift}/\nu_0$ by 4 to 5 orders of magnitude as compared to state-of-the-art microwave clocks [42]. In their realization, the inventions of the laser-cooling technique [43] and femtosecond frequency combs [44] were important milestones. Since then, a rapid development has led to optical clock systems that surpass the accuracy of microwave clocks by nearly two orders of magnitude with residual uncertainties of well below 10^{-17} (Tab.(2.2)).

In general, the accuracy of an atomic clock is strongly limited by shifts of the transition frequency ν_0 that may arise from electromagnetic perturbations or Doppler shifts due to residual atomic motion. To reduce the Doppler shift, the atom's spatial confinement needs to be much smaller than the transition wavelength (so-called Lamb-Dicke regime). Therefore, today's optical clocks use trapped and cold atoms. Cooling is typically performed in several stages utilizing the Doppler-cooling technique. For clock operation, the frequency of a highly stable interrogation laser is referenced to a long lived atomic transition $\nu_0 = (E_b - E_a/h)$ between the two energy states $|a\rangle$ and $|b\rangle$. Here, h refers to the Planck constant. The population in $|b\rangle$ is usually measured indirectly by detecting a stronger fluorescence signal generated using a third auxiliary state $|c\rangle$. The clock state population is subject to statistical fluctuations which are commonly referred to as *quantum projection noise* (QPN). This can be a fundamental stability limit for certain clock systems [42].

The fractional frequency instability is in the QPN limit given by

$$\sigma_y(\tau) \propto \frac{1}{Q\sqrt{N\tau}} \quad (2.11)$$

Hence it benefits from a high transition frequency ν_0 and a small atomic line width $\Delta\nu$ as well as large atomic numbers N .

Basically two different concepts based on trapped single ions or large arrays of neutral atoms compete in reaching for the highest accuracies. Neutral atoms can be stored in large numbers and according to Eq.2.11 strongly reduce QPN, while single ions are strongly confined and well isolated from the environment. Both types will briefly be discussed in the following.

2.3.1 Neutral Atom Clocks

An early generation of neutral atom clocks is based on spectroscopy of cold but freely expanding Ca atoms (see e.g. [45] for further reading). Ca clocks are relatively simple and robust while having a high short-term stability [46]. However, remaining Doppler-shifts cause systematic uncertainties of several 10^{-15} - a value that is surpassed by many microwave clock systems. Hence, optical calcium clocks are nowadays mostly used as flywheels in applications requiring high short-term stability.

Optical lattices generated by two counter-propagating laser beams are well suited to trap a large number of neutral atoms within the Lamb-Dicke regime. This would not only suppress the Doppler shift but also QPN due to the large atomic numbers that can

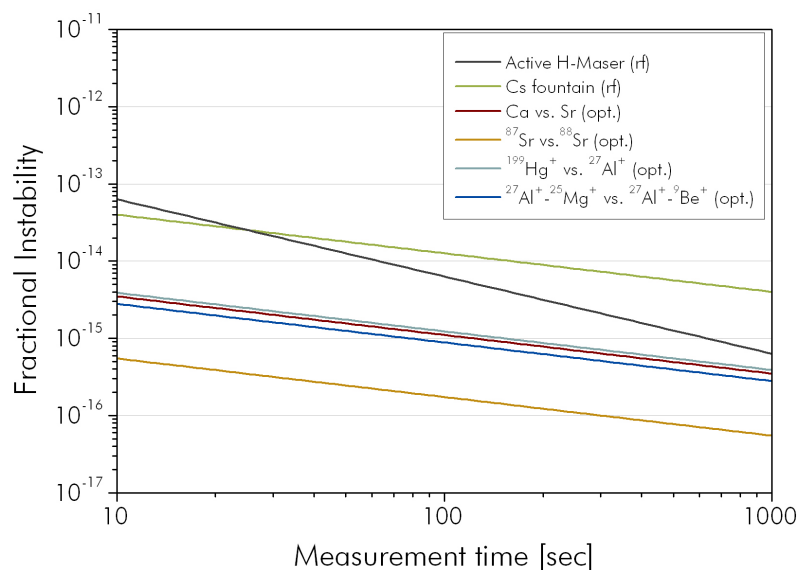


Figure 2.7: *Fractional frequency stabilities for state-of-the-art atomic clock systems (expressed as overlapping ADEV) [37, 48, 50, 51, 1].*

be stored in an optical lattice. However, the light field induces a Stark shift $\Delta\nu_{AC}$. It shifts the clock transition depending on the difference of the polarizabilities α_a and α_b of the two clock states.

Therefore, optical lattices were originally considered not to be suited as optical clock systems. In the late 1990, Katori and coworkers proposed a method to cancel this shift to first order using a clock laser at a *magic wavelength* for which $\alpha_a = \alpha_b$ [15]. The crucial improvement has not exactly been the cancellation of this shift as the uncertainty in the determination may not change. The improvement has been the conversion from an intensity measurement (ac-Stark shift) to a frequency measurement (clock laser frequency) that allows for a more accurate measurement of the residual uncertainty. This paved the way for optical lattice clocks.

The latest generation of strontium lattice clocks [47] shows a residual instability of $4 \times 10^{-16} \text{ s}^{-1/2}$. Its residual uncertainty has been measured to be 1.5×10^{-16} and is mainly determined by higher orders of the ac Stark shift (see Fig.2.7) and Tab.2.2).

2.3.2 Single Ion Clocks

Optical frequency standards based on single trapped mercury, ytterbium or aluminum ions promise high accuracy as they are highly immune against external field perturbations [3, 16]. While all relevant transitions in $^{199}\text{Hg}^+$ and Yb^+ are readily accessible, $^{27}\text{Al}^+$ does not exhibit a transition for cooling and fluorescence detection at a wavelength at which lasers are available. This is overcome by using an auxiliary logic ion with a more convenient cooling and detection transition to sympathetically cool the Al ion via Coulomb interaction [2]. Coupling to the same vibrational state with the logic

Frequency standard	Dominating uncertainty	tot. $\Delta\nu_{shift}/\nu_0$
Cs fountain	Distributed cavity phase - Microwave lensing	2.3×10^{-16}
Neutral Ca	1st order Doppler shift	7.5×10^{-15}
Sr lattice	Blackbody radiation shift	1.5×10^{-16}
Mercury ion	2nd Doppler - micromotion	1.9×10^{-17}
Aluminum ion	Micromotion	8.6×10^{-18}

Table 2.2: *Relative uncertainties for state-of-the art atomic clock systems [49, 48, 50, 3, 1].*

ion allows for indirect interrogation of the Al clock state. This technique is referred to as quantum logic spectroscopy. As of 2012, Al⁺ optical clocks represent the most accurate frequency standards in the world.

2.4 Clocks in Research and in Everyday Life

The unprecedented accuracy of atomic clocks allows for the most sensitive measurements that can be performed in laboratory experiments. Hence they help giving a deep insight into fundamental questions of modern physics. Atomic clocks have further found widespread applications in industry and society: Satellite navigation, the world-wide-web, cellular phones, even the electric power grid strongly rely on their high accuracy. Until the full establishment of a primary optical time standard, cesium atomic clocks will be present in every laboratory contributing to the world-wide realization of the SI-second.

All applications described below require appropriate linking of the involved clock systems. This can be accomplished straightforwardly if the clocks are located in neighboring labs or can be compared using well-established satellite based transmission schemes such as the Global Positioning System (GPS) and Two-Way Satellite Time and Frequency Transfer (TWSTFT) (see also next Chapter 3.1. However, to compare the latest optical clock systems neither GPS nor TWSTFT can provide sufficient stability and accuracy. These issues as well as the different approaches to solve it are described in the next Chapter 3.

2.4.1 Realization of the SI-second and UTC

The SI-second as defined by [14] is realized by standards institutes world-wide. Cs-fountain clocks provide the highest accuracy for realizing the SI-second but constitute complex experimental systems that are typically not operated continuously. Instead, they are used to calibrate a set of stable but not as accurate clocks such as commercial hydrogen masers and cesium beam standards that continuously produce a one pulse-



Figure 2.8: *World-wide locations of laboratories contributing to TAI in 2010. With kind permission of BIPM [53].*

per-second (pps) signal.

Their weighted average defines the national timing signal. In Germany, it is disseminated via a 77.5 kHz carrier signal using the DCF77 long-wave radio station close to Frankfurt a.M. [52]. More than 300 stable maser or cesium oscillators from 50 national metrology institutes contribute to the Temps Atomique International (TAI). The measurements are sent to the Bureau International des Poids et Mesures (BIPM) in Paris using two-way satellite communication (see Fig.2.8). TAI is published regularly through the Circular-T bulletin [53]. Primary standards from national physics laboratories in the United States, France, Italy, England, Germany, and Japan are contributing to the accuracy of TAI. The better known Coordinated Universal Time (UTC) is the time-of-day for many national and international civil organizations. It differs from TAI only by accounting for leap seconds.

2.4.2 Geodesy

Geodesy is the science of studying shape, size, and the gravitational field of Earth [54]. It thus helps to better understand the consequences of global warming, dynamic ocean topography and seismology and consequently to predict natural disasters such as earth-

quakes and tsunamis.

The establishment and linking of a Global Geodesy Observation System (GGOS) is currently being discussed to understand these effects in the global context [55]. One of the world-wide stations of GGOS will be established at the Wettzell station of the German Bundesamt für Kartographie and Geodäsie (BKG).

The observatory is comprised of a radio-telescope for Very Long Baseline interferometry, satellite laser ranging, a magnetometer, and a local gravity measurement system [56]. Basically all these system require precise time and frequency references. This is why BKG employs several Cs-clock and H-maser systems as well as a GPS-receiver.

One prerequisite of GGOS is a common reference height level that is undisturbed from tidal, geological, and atmospheric changes. This will require one master atomic clock in a suited location whose frequency defines the zero level gravitational potential. This could also be accomplished by employing one master clock in a spacecraft to define a true zero gravitational potential. Networks of ground optical clock systems - either transportable or linked via optical fibers - with uncertainties in the 10^{-18} regimes could then be used to link and synchronize all geodesy observatories world-wide.

2.4.3 Fundamental Constants and Cosmology

Drift of the Fine Structure Constant α

One of the most fascinating features of optical frequency metrology is its ability to probe the cornerstones of physical theories in a table top laboratory experiment. Testing these cornerstones implies the search for a time variation of the fundamental constants which provide the basic units for all physical systems - for experiment and theory alike. These constants are not deducible by theory. Thus, one has to rely on accurate experimental verification [57]. Here, dimensionless constants such as the fine structure constant α are of particular interest as they do not depend on the convention of units. These constants are referred to as *fundamental* constants.

A possible drift of the fine structure constant α was supposed to be observed in Quasar spectra at $\dot{\alpha}/\alpha=10^{-15}$ [58]. However, from recent laboratory experiments using optical clocks it could be shown that $\dot{\alpha}/\alpha$ is constrained to $1.6(2.3) \times 10^{-17}/\text{year}$ which is consistent to a zero drift [59, 60, 3].

Ultra-precise Tests of Special and General Relativity

Lorentz invariance is one of the cornerstones general relativity relies on. Its possible violation as proposed by string theory for example is systematically investigated by the

standard model extension theory as described in Chapter 6. Another condition that has to be fulfilled to validate general relativity is local position invariance. This implies not only the time independence of the fundamental constants as described above but also the universality of the gravitational red-shift (UGR). It is postulated to be violated by quantum gravity and string theory [61].

Hence, the investigation of UGR helps to test general relativity and to move towards a *theory of everything* that can incorporate both, general relativity and quantum mechanics.

Tests of UGR can be performed with high accuracy by measuring the frequency shift $\delta\nu_{red-shift}$ of two identical atomic clocks with frequency ν_0 in different gravitational potentials U_1 and U_2 . When placing the clocks with a height difference δh in Earth's gravitational field the following equation holds true:

$$\frac{\delta\nu_{red-shift}}{\nu_0} = (1 + \beta_{clock}) \frac{g\delta h}{c^2} \quad (2.12)$$

with c being the speed of light, g being the constant of gravitation and β_{clock} being a correction factor that accounts for a possible violation of UGR (i.e. if $\beta_{clock} \neq 0$).

As can be seen from Eq.2.12, these experiments benefit from high clock frequencies and from a large height difference. Clock comparisons between space and ground clocks are hence being planned such as, for example, the ACES project [62]. Experiments that confirm the UGR at a 7.0×10^{-5} uncertainty have been performed using H-masers and aluminum ion clocks [63, 2].

Chapter 3

Long-haul Time and Frequency Dissemination

Any frequency measurement requires comparing it with one or more, ideally more precise clocks. Hence, in order to link the increasing number of world-wide precision laboratories engaged in state-of-the-art time and frequency standards, a suitable infrastructure is of crucial importance. The stabilities of current satellite based dissemination techniques [25] using global satellite navigation systems or two way satellite time and frequency transfer reach an uncertainty level of 10^{-15} after one day of averaging. While this is sufficient for the comparison of most microwave clock systems, the exploitation of the full potential of optical clocks requires more advanced techniques.

3.1 Satellite-based Techniques

For time and frequency comparison using satellites, basically two different techniques are currently in use. One employs the *Global Navigation Satellite System* (GNSS) while the second utilizes geostationary telecommunication satellites for *Two-Way Satellite Time and Frequency Transfer* (TWSTFT).

3.1.1 Global Navigation Satellite System

The space-based Global Navigation Satellite Systems were originally developed for providing location and time information anywhere on Earth. The US version GPS (Global Positioning System) is currently the most used satellite based time and frequency dissemination system [64]. The techniques of the Russian system GLONASS and the future European GALILEO are very similar and can be reviewed in [65, 66].

GPS operates 24 satellites in three Earth orbits such that from each point on Earth at least 4 satellites are simultaneously in view. Each satellite carries one or more rubid-

ium or cesium microwave clocks on-board as a reference. Operating several clocks in sequences allows meeting the typical mission lifetime of approximately 8 years.

Two transmission carriers near 1.6 GHz and 1.2 GHz on the so-called *L1* and the *L2* bands are generated from the clock signal. Each satellite produces a unique code that contains detailed timing information. To allow all satellites to broadcast on the same carriers, the signals are phase-modulated with a pseudo-random noise code. Here, bit sequences of 0 and 1 correspond to 0° or 180° phase-shifts, respectively. The receiver possesses patterns of all satellite codes. Information is revealed only after cross-correlating the corresponding pattern with the signal. Among others, the satellite code comprises a logic 'tick' related to GPS time and also the satellite's clock relation to TAI (see Section 2.4) as timing information [67].

Two configurations can be employed for time and frequency comparisons between two remote user sites:

Common View (CV)

Two receivers record the data from the same satellite simultaneously. Here, satellite clock errors as well correlated fluctuations in the ionosphere cancel. The maximum distance that can be bridged between two remote sites is approximately 10,000 km.

All-in-View (AV)

Two receivers record the timing signals from all satellites in view. The receiver's clock signals are individually compared to the GNSS data and their differences are calculated based on these data. If the coordinates of a single receiver are well known their clock can be compared to the space clock ensemble and hence directly to TAI.

3.1.2 Two-way Time and Frequency Transfer

The principle of clock comparison using Two-way Satellite Time and Frequency Transfer (TWSTFT) is sketched in Fig.3.1. Similar to GNSS, signal transmission is accomplished by applying a pseudo-random noise modulation to the Ku-band (11 GHz for the down link and 14 GHz for the up link) and X- band (7 GHz for the down link and 8 GHz for the up link) carriers. Both ground stations *A* and *B* employ Time Interval Counters (*TIC*) that are started with the pps output of the local clock and stopped with the corresponding pulse of the transmitted clock, respectively. The timing information at each site is given by:

$$TIC(A) = A - B - d_{TB} + d_{BS} + d_{SBA} + d_{SA} + d_{RA} + S_B \quad (3.1)$$

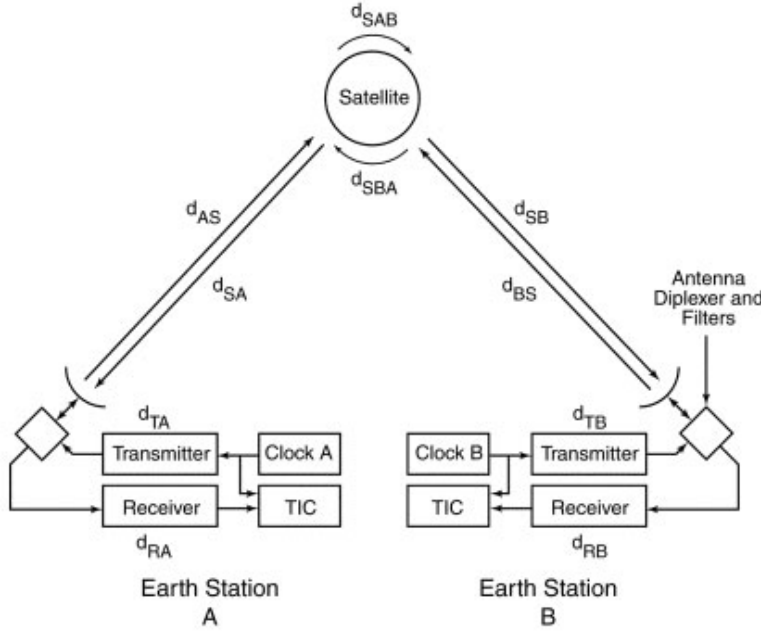


Figure 3.1: *Principle of Two-way Satellite Time and Frequency Transfer: Time Interval Counters (TIC) record the local clock signal as well as the transmitted clock signals at both sites A and B simultaneously. Various delays d_{xx} have to be taken into account (see text for details). With kind permission of M. Weiss [69].*

$$TIC(B) = B - A - d_{TA} + d_{AS} + d_{SAB} + d_{SB} + d_{RB} + S_A \quad (3.2)$$

with $TIC(A)$ and $TIC(B)$ being the counter readings, A and B being the local clock times, and d_{xx} being all propagation delays. This can be equipment delays in the receiver and transmitter electronics in the ground stations A and B or propagation delays between A , the satellite, and B . S_A and S_B are the Sagnac delays given by $2\omega A/c^2$. Here, ω is the angular velocity of Earth and c the speed of light. A is the area enclosed between the two clocks, the earth surface, and the satellite.

The clock difference can be obtained in two ways: either by post-processing or in real-time by sending the recorded data together with the timing pulses [69].

Due to the path reciprocity of this method, relative signal delays cancel to a large extent. Moreover, the Sagnac effect can be calculated with high accuracy even for only approximate knowledge of each location [70].

3.1.3 Limitations

The path lengths from the ground clocks to the space clocks are subject to fluctuations in the troposphere and in the ionosphere causing signal delays. Precise modeling of these atmospheric layers, which includes geographic and climate conditions, is of crucial

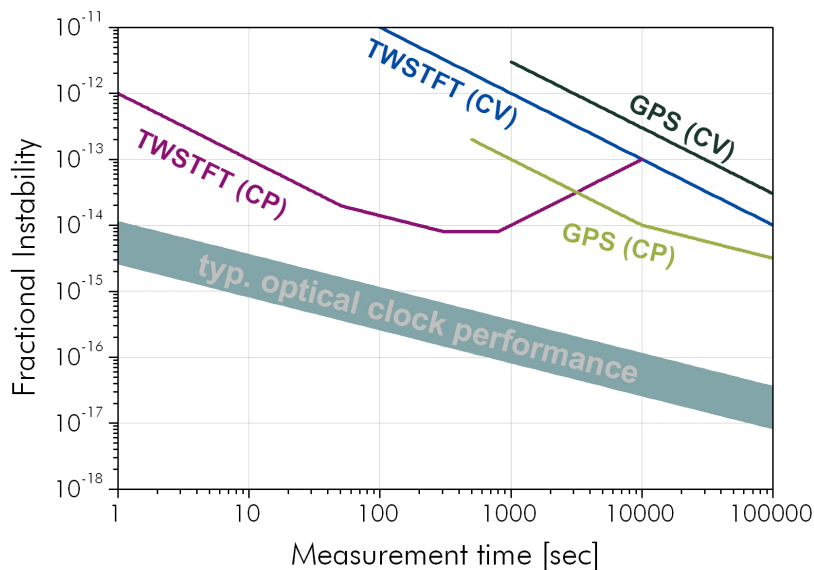


Figure 3.2: *Fractional instability of satellite-based time and frequency transmission for the common view (CV) and carrier-phase (CP) techniques. The deviation from a τ^{-1} -slope for GPS-CP is software-related. For TWSTFT-CP, the long-term stability is limited by unknown noise sources[70]. For comparison, typical optical clock performances are depicted as well.*

importance. Relativistic effects such as the first and second-order Doppler-effects as well as the gravitational red-shift have to be taken into account. They require precise knowledge of the satellite orbit and eccentricity. From the different dispersion for the $L1$ and $L2$ frequencies one can extract information about atmospheric fluctuations using GPS. This is why these frequencies are often measured simultaneously [68].

All these effects largely cancel when using the TWSTFT technique but a non-vanishing error remains due to the use of different carrier frequencies for the up link and the down link signals. Furthermore, any nonreciprocal delays that may occur in electronic components or due to residual satellite motion have to be taken into account as well as multi-path reflections due to objects nearby antennas or impedance mismatch at cable connections at the receiver's end. The latter are hard to estimate as they are often masked by other noise sources.

Both methods employ pseudo-random noise codes modulated onto carriers to transmit the timing information. Direct measurement of the carrier phase (CP) at a few GHz increases the frequency resolution by about a factor of 1000 as compared to code measurements thus providing a more stable clock comparison. However, the requirement to resolve identical cycles in the carrier phase limits the maximum distance between two remote users to about 50 km. Therefore, the common method to bridge larger distances is to average and fit the transmission code as to best match the CP data in order to help making the CP unambiguous [72].

Fig.3.2 shows the stability curves achievable with above named transmission methods. The minimum uncertainty achievable is 10^{-15} after one day of averaging [71].

This shows that satellite based transmission techniques do not provide sufficient stability and accuracy for the dissemination of the latest generation of time and frequency standards (see Section 2.3). Two alternative approaches have been discussed so far:

- a) *High end transportable clocks*
- b) *Time and frequency distribution using fiber networks*

3.2 Transportable Atomic Clocks

Instead of transmitting an optical atomic clock signal from one location to another the transportation of the clock itself is an intuitive option that is pursued by several research groups worldwide (e.g. [73]). Besides the calibration of other clock systems, their development represent a step towards space-borne optical clock systems. As discussed in the previous Chapter 2.4, space clocks could be used to measure Earth's geodetic profile with unprecedented precision. The prediction of earthquakes and volcanic eruptions could be another useful application. This scenario requires a network of ground space communication using both, telecommunication optical-fiber infrastructures as described below as well as high profile transportable clocks. Their employment will require a mutual development.

A unique atomic clock of interest is a portable cesium fountain clock developed by the French LNE-SYRTE for the PHARAO space project [74, 75]. It shows a comparable performance to laboratory systems [75] and is regularly compared to SYRTE's primary Cs fountain clocks FO₁ and FO₂. During the course of the year it travels to a variety of different locations to calibrate other clock systems or to participate on absolute frequency measurements such as the one described in Chapter 6 or in [76]. It is the only portable atomic fountain clock worldwide that contributes to TAI.

3.3 Fiber based Frequency Dissemination

Frequency dissemination via fiber networks has so far been investigated over regional distances of up to 480 km using three different methods for transmission: stable microwave transfer by means of an amplitude modulated laser, combined transfer of radio-frequency and optical signals by disseminating laser pulses, and transmission of an optical carrier wave. Naturally, only the latter provides the femtosecond resolution commensurate with the accuracy of optical clocks.

3.3.1 Transmission of Amplitude Modulated cw-Lasers of up to 86 km

The most straightforward method to obtain a precise microwave reference at the remote end of the fiber link is to send an amplitude modulated optical continuous wave laser. The remote user will not need much more than a fast photodiode to demodulate the sidebands of the optical signal in order to reconstruct the rf-signal [77]. Compared to a GPS transmission, measurement times will be significantly shorter and the microwave signal can be extracted after a few minutes of measurement time rather than after one day.

Fiber stabilization has to compensate for a group delay induced distortion of the microwave signal. This is usually performed using PZT fiber stretchers or temperature controlled fiber spools. Furthermore, this method is sensitive to *polarization mode dispersion* (PMD). Polarization scrambling reduces this effect [77].

As of 2012, the most precise rf-transmissions using AM-modulated lasers were performed in Paris between Laboratoire de Physique des Lasers (LPL) and the Systemes de Reference Temps Espace (SYRTE) on a 86 km fiber link. A 1 GHz signal was transmitted with a stability of 5×10^{-15} at one second integration time and a few 10^{-18} after one day. Advanced techniques such as fast polarization scramblers as well as sophisticated filtering were employed [78].

It is worth noting that this link was employed in a proof-of-principle experiment for the direct transfer of an optical carrier phase. Within the first attempt it showed similar results for the stability of the transmitted signal (see Fig.3.3) [79]. Above mentioned techniques to reduce PMD and AM-to-PM conversion were not applied here. This experiment already indicated the potential for the transmission of a purely optical signal.

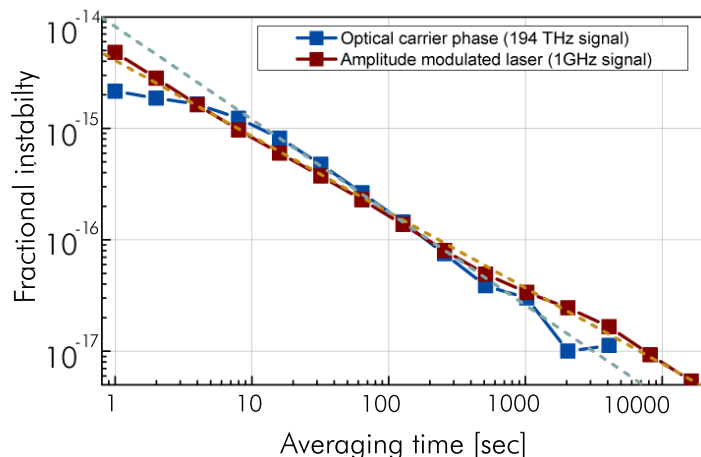


Figure 3.3: Transmission of a 1 GHz amplitude modulated cw laser signal via a 86 km optical fiber link in comparison to proof-of-principle optical transmission on the same link [78, 79].

3.3.2 Transmission of Pulsed Lasers of up to 50 km

Some applications may require the direct transmission of a femtosecond frequency comb (see Appendix B.2) which provides the user with both, an rf-reference and an optical signal at the same time.

Here, the repetition rate of the frequency comb and its harmonics can be extracted as a stable microwave signal while the optical comb modes provide a stable optical signal. All frequencies the comb spectrum covers can in principle be used at the remote user end [77]. The compensation of chromatic dispersion plays an important role for the quality of the transmitted signal since it will stretch the pulse duration. Similar to the transmission of an amplitude modulated carrier a delay line has to be implemented to balance the comb's group velocity. Care has further to be taken adjusting the average input power in order to reduce AM to PM conversion.

A 100 MHz repetition rate transmitted over a 50 km fiber link has been shown recently in [80] to have a stability of $4.6 \times 10^{-15} \text{ s}\tau^{-1}$, improving previous results from a 7 km fiber link by a factor of two [81].

3.3.3 Transmission of the Optical Phase of up to 480 km

The phase information of a frequency reference can also directly be linked to an ultra-stable optical carrier frequency. Using two frequency combs at each end of the link it allows for comparing various references in both, the microwave or optical regime. This method is advantageous since the influence of chromatic and PMD as well as amplitude-to-phase noise conversion is minimized for a cw signal. However, fluctuations of the optical path length due to temperature drifts or acoustic vibrations limit the achievable stability of the transmitted signal and require active stabilization (see next Chapter).

The transmission of optical carrier frequencies via stabilized urban fiber links of up to 172 km has been shown to have residual instabilities of a few parts in 10^{16} after 1 s which linearly decreases with the inverse integration time τ [82, 87, 84]. The longest fiber link investigated so far had a total length of 480 km [85]. The lowest fractional uncertainty of an optical signal transmitted over 146 km has been reported to be 1×10^{-19} [83]. Real-time comparison of two strontium optical clocks has been demonstrated over a distance of 120 km using optical telecommunication links [86].

All experiments performed during the course of this work were based on transmitting an optical carrier phase.

Chapter 4

Two 920 km Optical Fiber Links for Frequency Metrology

As described in Section 3.3, frequency dissemination via fiber networks has so far been investigated over regional distances of typically ~ 150 km. This chapter describes setup and characterization of the first purely optical fiber link for frequency comparison that reaches continental scales. The actively stabilized link consists of two dark fibers $F1$ and $F2$ connecting the Max-Planck-Institute of Quantum Optics (MPQ) and the Physikalisch-Technische Bundesanstalt (PTB). Therefore the link crosses a large part of Germany over a 920 km distance and in total comprises 20 remotely controllable optical amplifier systems.

4.1 Transmission Scheme

The principle of frequency comparison using an optical fiber link is shown in Fig.4.1: Two reference frequencies ν_1 and ν_2 are compared by using two frequency combs and two ultra-stable transfer laser systems as flywheels. Here, the frequency comb technique allows for a flexible choice of various types of frequency references (both, rf and optical) without having to change the setup. The building blocks of the transmission scheme will be described step by step in the following.

4.2 Frequency Comb Systems

A femtosecond frequency comb is a mode-locked laser which emits a pulse train with the characteristic feature of two subsequent pulses having a fixed phase relationship. This pulse train generates a periodic pattern in the frequency domain and forms a comb-like structure of equally spaced modes that are fully determined by two microwave frequencies f_{rep} and f_{ceo} . Any unknown optical frequency ν within the spectral range of

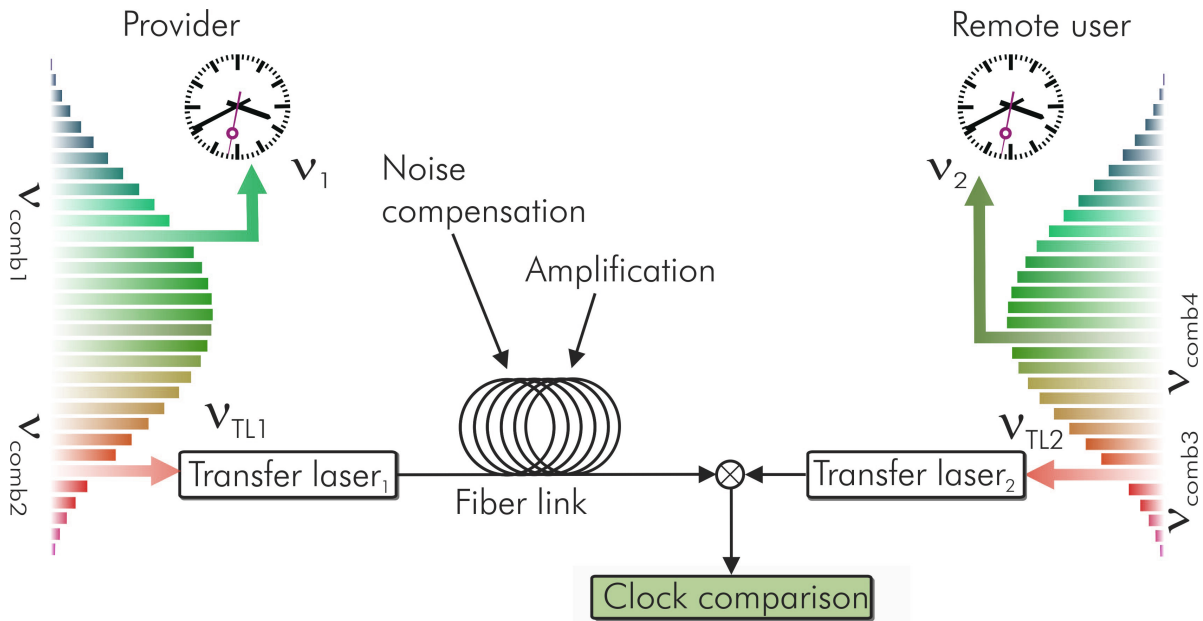


Figure 4.1: *Principle of frequency dissemination using an optical fiber link: The phase stability of a frequency reference ν_1 is linked to a stable optical carrier wave with frequency ν_{OC1} by means of a femtosecond frequency comb. This signal is transmitted on an actively noise-compensated fiber link that allows for repeated amplification. The remote user employs a similar laser system with frequency ν_{OC2} to establish, again by means of a frequency comb, the linking to their clock ν_2 .*

the comb can thus be deduced from three radio frequencies by measuring the beat note f_{beat} between ν and the closest comb mode $\nu_n = f_{ceo} + n \cdot f_{rep}$ (see Appendix B.2):

$$\nu = f_{ceo} + n \cdot f_{rep} + f_{beat} \quad (4.1)$$

with $n \in \mathbb{N} \sim 10^6$.

In this experiment, both PTB and MPQ employ erbium fiber laser based frequency combs [88] with offset frequencies $f_{ceo} = 30$ MHz. The MPQ system has a repetition rate f_{rep} of 250 MHz [89] while the PTB system operates at 100.003003 MHz [90].

4.3 Transfer Laser Systems

State-of-the-art stable laser systems usually employ high-finesse Fabry-Perot resonators that are used to stabilize the laser output. These lasers show residual short-term instabilities of up to a few 10^{-16} [40]. This corresponds to mirror displacement lengths in the femtometer range. Therefore, perfect isolation from environmental perturbations is of crucial importance.

Different strategies are pursued in order to minimize perturbations. Some cavities employ spacers made out of silicon and are operated in cryogenic environments to reduce thermal motion of the mirror atoms [91]. Other cavities have a special geometry to make them less sensitive to vertical acceleration and horizontal displacement alike. As an example, a spherical spacer is mounted at a magic angle at which horizontal and vertical displacements exactly cancel [92]. They are particularly suited to work in non-laboratory environments.

The cavities employed in the MPQ and PTB link laboratories consist of highly reflecting mirrors optically contacted to a spacer made out of *Ultra-Low Expansion* glass (ULE, manufacturer: *Corning*) for which the thermal expansion coefficient has a zero crossing around room temperature.

The finesse \mathcal{F} of the cavity is defined as the ratio of free spectral range to the width of the transmission maximum. It can be measured using the *ring down* technique. Here, the decay time τ_{RD} of the light inside the cavity is measured at which only a fraction e^{-1} of the initial intensity is left. The number of corresponding reflections can be estimated from the cavity length L_{cavity} and the phase velocity of the light $v_{ph} = c/n$:

$$N_{refl} = \frac{\tau_{RD} \cdot c}{n \cdot L_{cavity}} \quad (4.2)$$

From that one obtains the reflectivity $R = (1 - e^{-1})/N_{refl}$ of a single mirror and thus can determine the finesse of the two-mirror system to be:

$$\mathcal{F} = \frac{\pi(R_1 \cdot R_2)}{1 - (R_1 \cdot R_2)^2} \quad (4.3)$$

Each transfer laser system comprises a near-infrared distributed feedback (DFB) fiber laser (Koheras *ADJUSTIK*) at 1542.5 nm with ~ 100 mW output power and a free run-

ning line width of ~ 5 kHz (Full Width Half Maximum). Around this wavelength, fused silica fibers show a minimum in the attenuation. In the following, the lasers will be denoted as NIR_{MPQ} and NIR_{PTB} , respectively. Both lasers are stabilized to high-finesse Fabry-Pi $_{\frac{1}{2}}$ rot cavities with ultra-low expansion glass spacers (ULE) (see Appendix D) such that short-term laser noise becomes negligible compared to the phase noise of the free-running fiber link (see Appendix B.1.4).

Approximately $100 \mu\text{W}$ are coupled into each cavity. A fast Pound-Drever-Hall-lock (see Appendix D) controls an acousto-optic-modulator (AOM) behind the laser thus shifting the output signal with response times of nanoseconds (fast lock). In addition, slow thermal laser drifts are compensated by a piezo-electric transducer that controls the laser resonator length in order to keep the AOM center frequency. Both systems are actively temperature stabilized and in high vacuum. Decoupling from seismic noise is achieved by using active isolation platforms. Also, the laser intensity is stabilized as any change of the light power inside the cavity is directly converted into frequency fluctuations due to heating of the mirrors. An IR-sensitive CCD camera monitors the cavity transmission and is used to visualize the cavity TEM_{00} mode used to lock the laser.

4.3.1 Vertical Cavity Design: MPQ System

The MPQ cavity is set up in a vertical design [93]. In this configuration, a vertical displacement of the lower mirror comes with a vertical displacement of the upper mirror in the same direction. The cavity length is thus held constant to first order.

The two mirrors sit on a 77 mm long football-shaped spacer made out of ultra-low

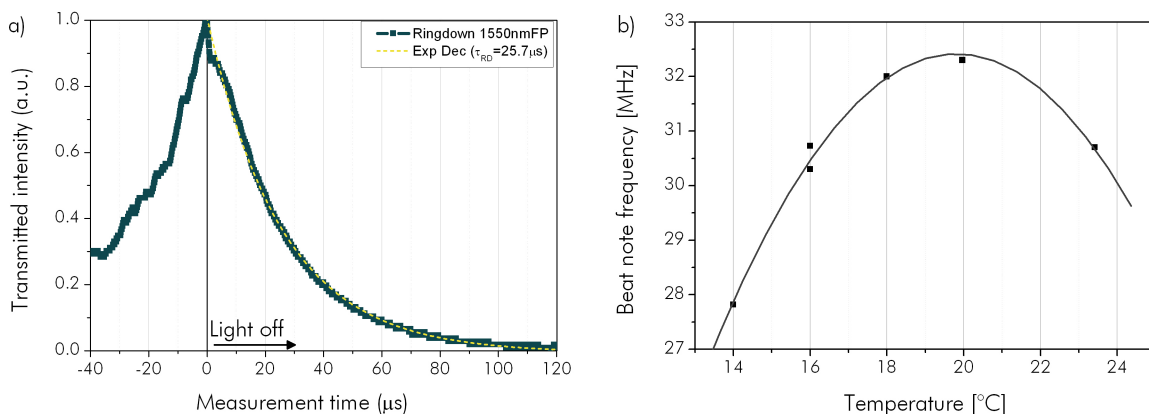


Figure 4.2: a) Ringdown measurement of the light intensity stored inside the MPQ cavity. b) Temperature dependence of the beat note between cavity stabilized laser and frequency comb. The temperature at which the spacer is largely insensitive to length changes is at 19.8°C .

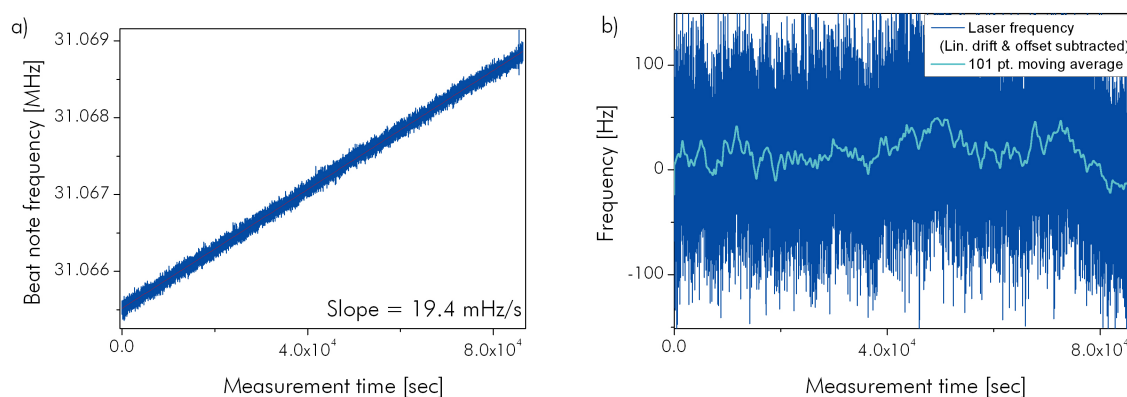


Figure 4.3: *Beat note between the cavity-stabilized laser frequency and a femtosecond frequency comb: a) Drift of 19 mHz/s at 19.81° C. b) Linear subtraction yields residual fluctuations of less than 50 Hz peak to peak over the duration of one day. The curve is averaged to reveal the laser fluctuations out of the comb noise.*

expansion glass (ULE) which is loosely mounted in the mid plane of the cavity. The system is similar to the one described in [94].

With a ring down time τ_{RD} of 26 μs (see Fig.4.2a)) the cavity finesse \mathcal{F} has been determined to be 251,549. The zero crossing temperature of the cavity spacer is 19.81°C (see Fig.4.2b)). Fig.4.3a) shows the drift at this temperature which is about 20 mHz/s. This is attributed to the aging process of the ULE spacer. After subtracting a linear drift the residual fluctuations are less than 50 Hz peak to peak over one day as shown in Fig.4.3b).

4.3.2 Horizontal Cavity Design: Transportable PTB System

Thomas Legero from PTB has developed a transportable transfer laser system based on a horizontally mounted ULE cavity which was especially optimized for rigidity and small vibrational sensitivity [95]. It has a finesse of $\sim 330,000$. The horizontal cavity design allows for a robust transportation mounting (see Fig.4.4). The complete laser system is installed in a compact mobile 19" rack weighting less than 150 kg.

To compare the two laser systems directly, the PTB laser system was moved from Braunschweig to Munich. The relative stability of the two lasers is depicted in figure Fig.4.5) and shows a 4×10^{-15} flicker floor after subtracting a third order drift.

This strongly nonlinear drift has been attributed to the ambient laboratory temperature during the measurement that was approximately 30°C due to a malfunction in the air conditioning system. The PTB laser cavity could hence not be operated at its zero

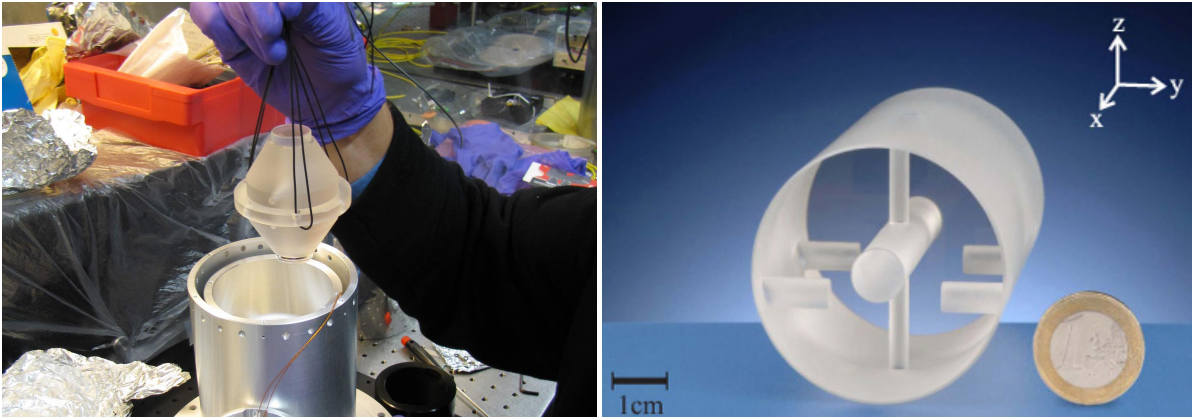


Figure 4.4: *Left panel: Vertical MPQ- cavity with football-shaped spacer. The cavity is mounted inside the vacuum chamber in the mid-plane of the spacer. Right panel: Cavity spacer of the transportable PTB laser system. Viton pins hold the cavity in four holes in the mid-plane. PTB Z.169 photography, S. Stork*

crossing temperature at these environmental conditions¹. Therefore the cavity resonance frequency was highly sensitive to temperature fluctuations.

The line-width of the beat note was measured to be 2 Hz using a spectrum analyzer with 1 Hz resolution bandwidth. Assuming equal performances and a Lorentzian line-shape the line-width of the individual lasers can be estimated as 1.5 Hz.

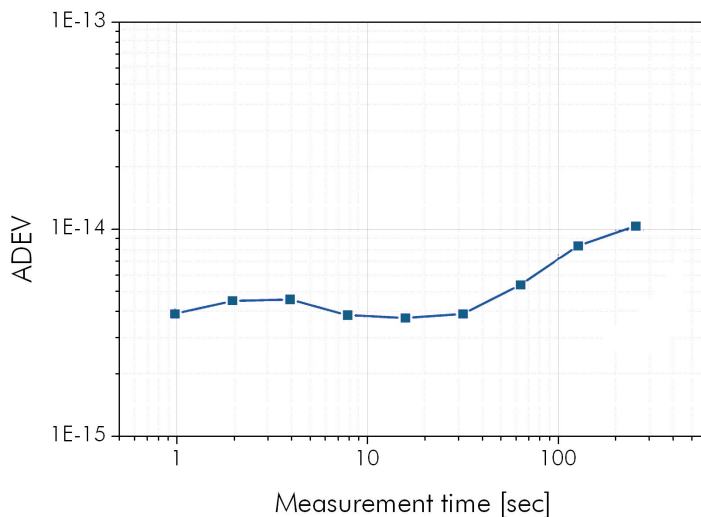


Figure 4.5: *Direct comparison between the MPQ laser system and the transportable PTB laser system.*

¹The temperature stabilization circuit was designed for heating to the zero-crossing temperature at about 28°C but not for cooling

4.4 Two 920 km Fibers connecting MPQ and PTB



The establishment of the two 920 km fibers connecting MPQ and PTB has been accomplished in collaboration with the German Science Network (DFN), the fiber provider Gasline GmbH, the Institute of Quantum Optics (IQ) at University of Hanover, *MenloSystems* GmbH and the Max Planck Institute of the Science of Light in Erlangen.

The link has backbones at several computing centers located at the Garching campus (LRZ), at University Erlangen, at University Leipzig, and at PTB. The fiber carrier Gasline GmbH is a subsidiary of the German energy provider EON Ruhrgas GmbH. Because of this, the fibers are laid next to gas pipelines most of the way. Installed at least one meter below ground and two meters away from the pipeline, the influence of temperature fluctuations and acoustic perturbations is reduced (see Fig.4.6).

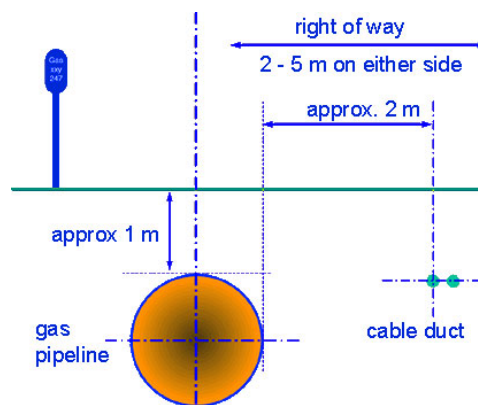


Figure 4.6: *Installation scheme of Gasline GmbH fiber links (according to municipal right of way). Courtesy of Gasline GmbH.*

Each fiber has a length of 916 km. All Gasline fibers are specified according to the ITU-T G.652 standard[96]. In particular, they have a core refractive index of $n = 1.4681$ at 1550 nm, an attenuation α of < 0.23 dB/km, and a chromatic dispersion D_C of 18 ps/(nm km).

The fibers are accessible about every 90 km via seven telecommunication containers and via two backbones in computing centers in Erlangen and Leipzig (see Fig.4.7 and Fig.4.8): left panel).

The access to the stations has to be announced in written form to *Gasline GmbH* at least two days in advance. A phone call in front of the station authorizes the entrance by remotely unlocking the door. Additionally, both link teams have been handed a key that opens all doors and also the gates to enter the areal.

Inside the containers the fibers end in outlets that are pre-assembled with E2000 connectors to enable installation of optical amplifier systems (see Fig.4.8: center panel).

The in-line amplifiers as described below were installed on both fibers within several extensive measurement campaigns. At least two members from the MPQ group and the PTB group met either in Garching or Braunschweig with two cars and redundant test equipment. The first team member installed the amplifier system in a certain repeater

4. Two 920 km Optical Fiber Links for Frequency Metrology

Location	Length [km]	Attn. [dB]	Delay [ms]
PTB	0	0	0
Ammensleben	92	22	0.45
Cörmigk	79	21	0.39
Leipzig	114	24	0.56
Zimmritz	119	25	0.58
Großbreitenb.	79	20	0.45
Ebersdorf	74	19	0.36
Erlangen	102	23	0.50
Beilngries	88	19	0.43
Münchsmünster	82	18	0.40
MPQ	87	21	0.43
tot.	916	212	4.55




Figure 4.7: Location, distance, attenuation, and light round-trip delay for the 9 repeater stations along the 920 km fiber link.

station while the second tested all settings in the previous station. A third person in the laboratory had to verify that the signal levels were appropriate after the two fibers were connected in the most distant station to form a loop. Due to the lack of cell phone connections in most stations, a fiber optic talk set (*GAO Fiber Optics 08311*) enabled the communication.



Figure 4.8: Left: View of the most southern repeater station near Münchsmünster 86 km north of Garching. Center: Fiber outlet with E2000 connectors. Right: Remotely controllable optical amplifier right before installation.

4.5 Active Fiber Noise Cancellation

Environmental perturbations that cause frequency shifts due to motion of the fiber atoms are commonly referred as *Doppler noise*. This especially concerns temperature fluctuations and acoustic vibrations that both cause severe limits on the achievable stability and accuracy of the transmitted signal.

4.5.1 Noise Origins

The optical path length of a medium with refractive index n and length L changes with temporal temperature fluctuations as:

$$\frac{d(nL)_T}{dt} = \left(L \frac{dn}{dT} + n \frac{dL}{dT} \right) \frac{dT}{dt} \quad (4.4)$$

The thermo-optic and the thermal expansion coefficient $\frac{dn}{dT}$ and $\frac{dL}{dT}$ can be found in the literature and are equal to $1 \times 10^{-5}/\text{K}$ and $6 \times 10^{-7} \text{ m/K}$ for fused silica, respectively [97]. For a signal with frequency ν_0 and vacuum wavelength λ_0 this results in a fractional frequency fluctuation :

$$y(t) = \frac{1}{\nu_0 \lambda_0} \frac{d(nL)_T}{dt} \quad (4.5)$$

The annual temperature variation in 1 meter soil depth is, for example, measured at the geodetic institute Potsdam Telegrafenberg [98] (see Fig.4.9). The mean varies between 20 °C in summer and 2°C in winter. This corresponds to a maximum heating rate of 2 $\mu\text{K/s}$ thus causing an optical frequency of 194 THz to shift by about 10 μHz per meter fiber length. For the 920 km link, this results in annual frequency variations of up to 10 Hz.

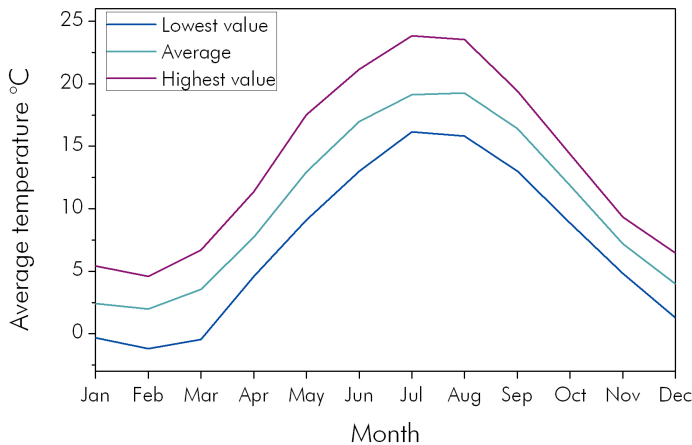


Figure 4.9: Averaged annual temperature variations (1894-2006) 1 m below ground measured at secular station Potsdam Telegrafenberg, Germany [98].

Acoustic waves with pressure P induce stress inside the fiber which also cause phase fluctuations of the signal. Analogous to Eq.4.4, the temporal change of the optical path length can be written as:

$$\frac{d(nL_P)}{dt} = \left(L \frac{dn}{dP} + n \frac{dL}{dP} \right) \frac{dP}{dt} \quad (4.6)$$

Assuming that the resulting strain is linear and isotropic and has no shear components dn/dP is in the order of 5×10^{-11} /Pa and dL/dP is approximately $dL/dP \sim 10^{-11}$ m/Pa [17]. The phase of a 1542 nm signal traveling in 1 m fiber with mean refractive index $n=1.47$ thus changes by 0.1 mrad/Pa. Fast acoustic pressure changes with frequencies between 20 Hz and 20 kHz hence cause frequency shifts between 0.3 mHz/Pa and 0.3 Hz/Pa.

4.5.2 Stabilization Scheme

As discussed above, both, the short- as well as the long-term stability of a fiber link will be strongly limited by Doppler noise. A widely used stabilization scheme that was originally developed by [99] relies on suppressing the optical path length fluctuations at the remote end by employing a phase-locked loop at the local end.

The experimental setup is sketched in Fig.4.10: frequency shifters such as for example acousto-optic modulators (AOM) are installed at the input and the remote site of the fiber allowing for heterodyne beat detection at a convenient radio-frequency (see Appendix B.1. At the remote end, a Faraday mirror reflects a fraction of the light back towards the input. Using a circulator that discriminates the light propagations directions, the round-trip signal is compared to a local copy of the original light. This beat note reveals information about the accumulated fiber phase-noise and is used to steer the AOM at the input of the fiber in order to compensate for it. While this AOM is used for frequency control, the second AOM at the remote site discriminates the desired reflection from the Faraday mirror from the backscattered light within the fiber and reflected light from connectors. The Faraday mirror rotates the signal polarization by 90° . This way, polarization rotation along the fiber is compensated on the way back and the signal arrives exactly 90° polarization rotated after one round-trip. The remote signal is now widely fiber noise compensated and can be used at the user's site.

The stabilization scheme can be considered as a Michelson interferometer with one short reference arm and one arm comprising the entire link.

The theory of the loop control is described in the Appendices C and E. A fundamental limit on the achievable degree of phase noise suppression is caused by the finite speed of light that imposes a delay between the remote and the round-trip signal. First, it

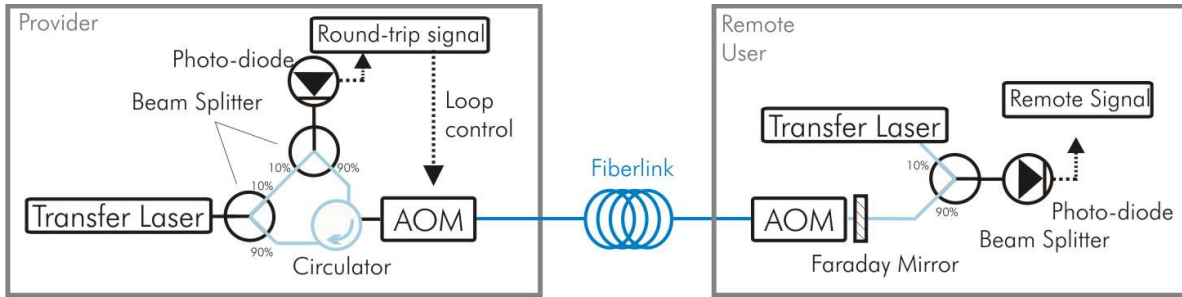


Figure 4.10: Mach-Zehnder interferometer for stabilization of an optical fiber path. See text for a detailed description.

directly affects the control bandwidth of the compensation loop and as a result, the total phase noise at high Fourier frequencies is given by unsuppressed noise of the fiber link. Second, the delay through the link results in an imperfect cancellation of the noise at the remote end. This imperfect cancellation of the one-way fiber noise due to the delay dominates at low Fourier frequencies and limits the attainable stability. Within the limit of stationary phase fluctuations, the residual one-way PSD of the stabilized link can be written as [100]:

$$S_{remote}(f) = \frac{4\pi^2}{3} \left(f \frac{nL}{c} \right)^2 S_{fiber}(f) \quad (4.7)$$

where L is the one-way physical path length, n the index of refraction, c the speed of light, and $S_{fiber}(f)$ denotes the phase noise of the un-stabilized link. Assuming that $S_{fiber}(f)$ is dominated by white frequency noise and scales proportionally to the link length, the attainable link instability in frequency comparisons increases as $L^{3/2}$ [100]. Hence, a fiber with large $S_{fiber}(f)$ may require several shorter subsequent stabilization loops in order to gain bandwidth and decrease the delay error.

Furthermore, laser phase noise has to be negligible in comparison to the fiber phase noise which is why both transfer lasers have been stabilized to ULE - cavities (see also Appendix B.1). Also, the interferometer comprises fiber parts that are not enclosed in the feedback loop (see Fig.4.10, light blue fiber paths). This requires passively stabilization as will be described in Section 5.1.

For the two 920 km links, random fiber noise results in fractional frequency excursions of about 5×10^{-14} (see next Chapter 5). Active fiber noise compensation has thus been a prerequisite for stable and accurate transmission.

Due to the round-trip time of 9.1 ms the stabilization bandwidth is limited to 56 Hz and the phase noise suppression at 1 Hz can according to Eq.4.7 be expected to be 36 dB for an ideal loop filter. A specially designed loop filter as suggested by [101] and described

in Appendix E could improve the fiber noise cancellation beyond the round-trip delay. However, the technical realization of this filter was very sensitive to slight changes in gain and did not allow for stable operation. Further refinement of the filter design would be necessary to make this a valuable tool for future experiments.

4.6 Signal Amplification

Over short distances, signal regeneration is not a critical issue and may be achieved without further in-line amplification. Over a 920 km distance, the inherent attenuation of 0.23 dB/km adds up to a total one-way attenuation of more than 200 dB. Hence, nine pairs of low noise bi-directional Erbium-doped fiber amplifier (EDFA) systems have been conceived, developed, and installed within the course of this work.

As the Doppler noise cancellation described above demands identical optical paths in both directions, the in-line amplifiers are operated bi-directionally. Their design has to assure appropriate power levels at the remote user end and a sufficient signal-to-noise ratio (SNR) for proper detection. Furthermore, fiber Brillouin amplifiers have been installed at both ends of the link in the MPQ and PTB laboratories.

4.6.1 Erbium doped amplifiers

Erbium doped amplifiers (EDFA) provide efficient amplification in the wavelength band around 1550 nm. They further consist of cost-effective telecommunication components and are straightforward to assemble. Yet, in long haul fiber link experiments they have to fulfill a set of requirements.

1. Small signal amplification

The most efficient nonlinear process inside an optical fiber is Stimulated Brillouin Scattering (SBS). It converts incoming signal photons into acoustic phonons that decay into Stokes- and anti-Stokes shifted, backscattered photons and thus get lost. The threshold power for the onset of SBS is given by [85]:

$$P_{th} = \frac{21 \cdot A}{\gamma L_{eff}} \left(1 + \frac{\Delta\nu_{signal}}{\Delta\nu_B} \right) \quad (4.8)$$

Here, A is the effective fiber mode area (10^{-10} m²), γ is the gain coefficient of the nonlinear process (5×10^{-11} m/W). The effective gain length is $L_{eff} = (1 - e^{-\alpha L})/\alpha$, which is ~ 21 km for $\alpha = 0.2$ dB/km. The Brillouin line width $\Delta\nu_B$ depends on the phonon life time τ_B : $\Delta\nu_B = 1/(\pi\tau_B)$. It was measured to be 20 MHz using an electronic spectrum analyzer. With a signal line width of 1.5 Hz the threshold power P_{th} can be estimated

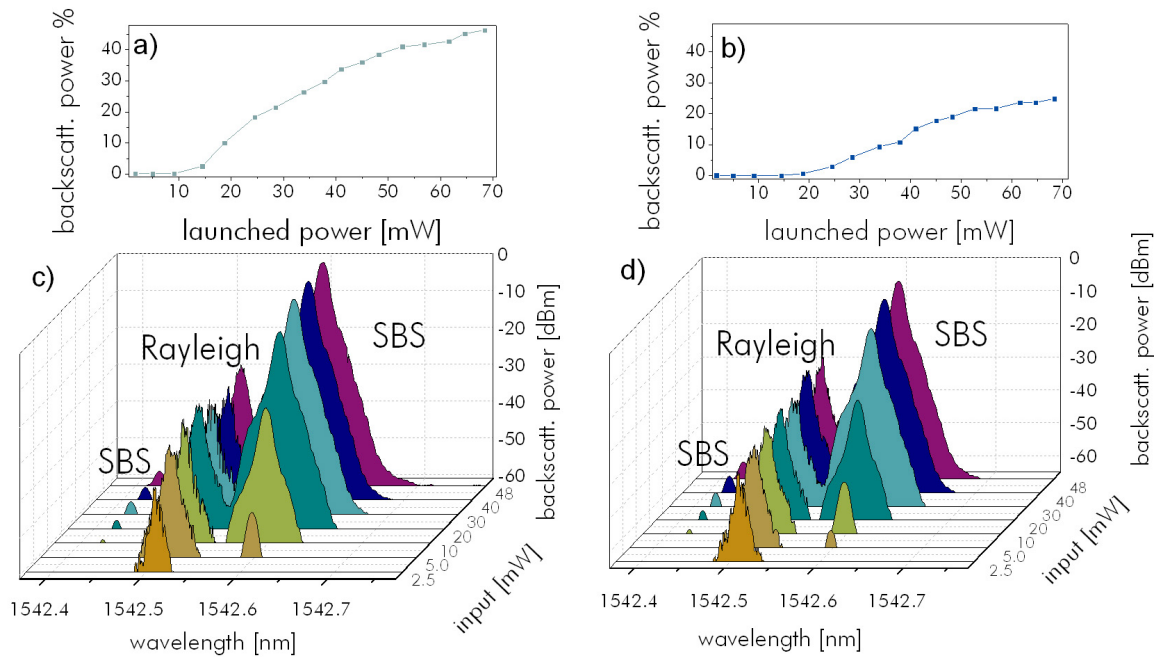


Figure 4.11: Backscattered light for different signal powers at 1542.5 nm injected into the 920 km fiber link measured with an optical spectrum analyzer (0.05 nm resolution bandwidth). The backscattered fraction of the launched power is shown for fiber F1 (a) and fiber F2 (b), respectively. Spectrally resolved observation of the backscattered light shows the increasing Brillouin Stokes and Anti-Stokes peaks as well as elastically backscattered light (Rayleigh scattering).

be 10 mW. By measuring the backscattered fraction of the signal the power that can be launched into the fibers has been limited to 6 mW (see Fig.4.11). Typical distances between two subsequent repeater stations of ~ 100 km thus resulting in μW -input signals each amplifier has to re-gain by minimum degeneration of the SNR.

2. Low Noise Figure

The main noise contribution decreasing the SNR of a signal passing an optical amplifier arises from *Amplified Spontaneous Emission* (ASE). The characteristic quantity to specify the degradation is the EDFA Noise Figure NF :

$$NF = \frac{SNR_{in}}{SNR_{out}} \quad (4.9)$$

which can be expressed as [102]:

$$NF \approx 2\eta_{SP} = 2N_2/(N_2 - N_1) \quad (4.10)$$

with the spontaneous emission factor η_{SP} N_1 , N_2 being the populations in the ground and the excited state of the gain fiber, respectively. Hence, the SNR of a signal passing

an amplifier is always decreased by at least 3 dB (for full inversion). The rate equations are given by [103]:

$$\dot{N}_2 = (\sigma_p^a N_1 - \sigma_p^e N_2) \Phi_p + (\sigma_s^a N_1 - \sigma_s^e N_2) \Phi_s - \frac{N_2}{\tau_{2-1}} \quad (4.11)$$

$$\dot{N}_1 = (\sigma_p^e N_2 - \sigma_p^a N_1) \Phi_p + (\sigma_s^e N_2 - \sigma_s^a N_1) \Phi_s + \frac{N_2}{\tau_{2-1}} \quad (4.12)$$

with the σ_i^j being the absorption and emissions probabilities, and $\Phi_i = P_i/(h\nu_i)$ the photon flux for the pump and seed light with powers P_i and frequencies ν_i , respectively. τ_{2-1} is the life time of the excited state which is for a 980 nm pumped EDFA ≈ 10 ms. For small input powers, a low NF can be achieved by low pump powers and low fiber doping together with an adapted gain fiber length. This avoids the creation of excess ASE.

The amplifiers employed in the experiment have been measured to have a noise figure of 4.1 for 1 μ W input power. To avoid the EDFAs saturating from broadband ASE, bi-directional narrow band optical band pass filters (100 GHz at 1542.5 nm) were installed in every second EDFA system. The final EDFA layout is shown in Fig.4.12.

3. Bi-directional operation and Back-Reflections

EDFAs are affected by randomly occurring back reflections from splices or due to Rayleigh scattering [105]. The onset of lasing may cause a sudden drop of the signal power if the gain of the amplifiers is too high resulting in a loss of phase coherence.

Thus, the EDFA gain settings are critical parameters for reliable and cycle-slip-free operation of the fiber link. Reflecting surfaces -where identified- were hence cleaned, polished and index-matching gel was applied. Unfortunately, the fibers are not always accessible leaving the system with remaining scattering centers or reflecting surfaces

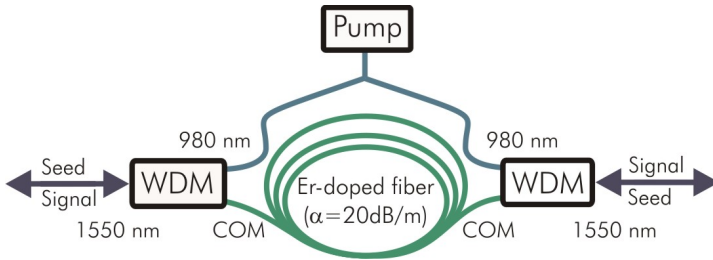


Figure 4.12: Final layout for the symmetric fiber link EDFAs. The 974 nm pump diode is split and equal parts of power are injected into the Erbium-doped gain fiber by a wavelength division multiplexer that combines the 1542 nm seed with the pump light. Due to the low doping the amplifier is specifically suited to re-generate small seed powers.

that could not be eliminated.

This required keeping the EDFAs below lasing threshold even though the signal strength may not be recovered. To fully regain the signal, the implementation of fiber Brillouin amplifiers (FBA) at both ends of the link in the PTB and MPQ laboratories has been mandatory. Together with the careful adjustment of the EDFA pump powers, this has been crucial for stable operation. The gain profiles of the bi-directional EDFAs as well as of the FBAs is shown in Fig.4.13.

4.6.2 Fiber Brillouin Amplifiers

SBS, as mentioned above, is typically an undesired nonlinear process in optical fibers. However, if generated in a targeted manner it can be utilized to amplify an optical signal in a normal fused silica fiber [104, 85].

Stimulated acoustic waves have a velocity $v_A = 6 \times 10^3$ m/s inside an optical fiber. They cause non-elastic scattering of signal photons and down-shift their frequency by $\nu_B = 2n_{eff}v_A/\lambda$. In the case of a 1542 nm signal this corresponds to an 11 GHz shift. The pump laser with power P_{pump} and a frequency ν_{pump} is injected into the fiber counter-propagating with the signal light. If the pump frequency is exactly shifted by the Brillouin Stokes-shift of the signal frequency it will cause a Brillouin gain G_B given by:

$$G_B = \frac{\gamma L_{eff} P_{pump}}{A} \quad (4.13)$$

with the earlier introduced gain coefficient γ , effective fiber mode area A , and the effective length L_{eff} . From Eq.4.13 a gain of ~ 10 dB /mW can be estimated. The actual signal with frequency ν_{sig} will be amplified if it propagates in the opposite direction and

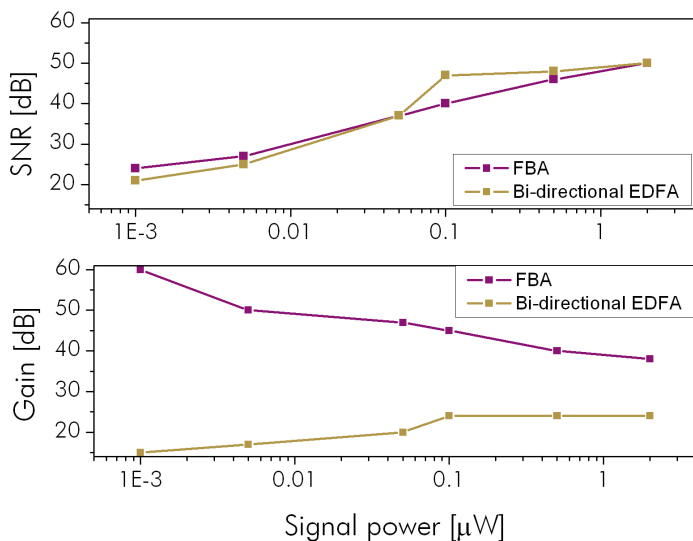


Figure 4.13: *Gain vs. input power for a fiber Brillouin amplifier. It can reach 60dB for nW signals. The SNR is on par with the bi-directional EDFAs designed for the presented setup [85].*

if the pump frequency matches the Brillouin shift:

$$\nu_{pump} = \nu_{sig} + \nu_B \quad (4.14)$$

FBAs allow for signal amplification with a gain up to 60 dB, which is nearly a 40 dB improvement over erbium-doped bi-directional amplifiers (see Fig.4.13). This way, FBAs have been demonstrated to regenerate signals over 500 km in a single step by [85]. However, as the Brillouin spectrum is so narrow, longer distances would require an in-line locking of the FBA to the incoming signal. This is why they have not been implemented as in-line amplifiers in the current setup.

4.6.3 Optical Remote Control

Being able to control and monitor the in-line EDFAs from the laboratory has been a prerequisite for the successful establishment and maintenance of the link. The EDFAs are connected to a micro-controller (μ C) inside the EDFA device (see Fig.4.8: right panel) that processes commands based on the RS-232 protocol. The μ C can read and write amplifier settings such as pump current and temperature control. As UMTS or mobile networks are often shielded inside the telecom containers the straightforward solution was to use the fiber link itself as a communication channel. The conversion from RS-232 to an optical signal has been accomplished by amplitude modulation of a 1310 nm laser diode. This signal is combined with the 1542 nm channel by means of a wavelength division multiplexer (WDM) and sent to the first container. There it is split from the 1542 nm signal (see Fig.4.14). A photodiode together with suitable electronics converts the modulated light back into the RS-232 signal to be processed by the μ C. Every amplifier is uniquely addressable. The controller forwards any message

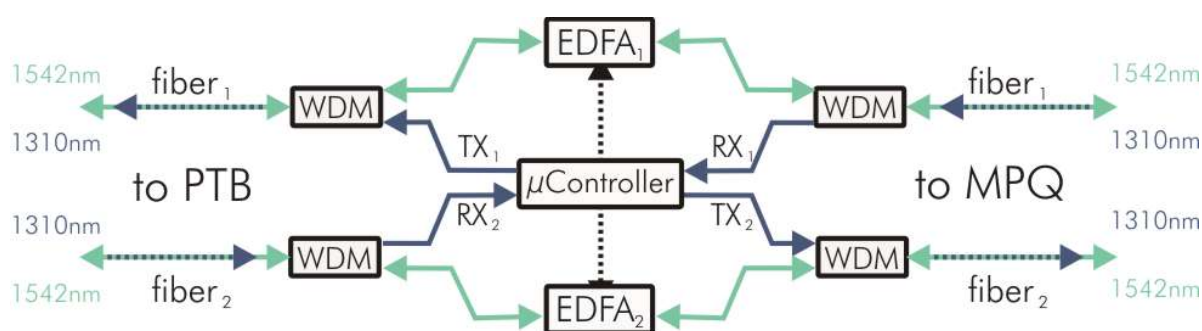


Figure 4.14: Schematics of the EDFA remote control. The 1542 transmission signal (turquoise) is amplified and sent to the next container station. The amplitude modulated 1310 nm signal (dark blue) is converted to an electrical signal (RX1) and communicates with the micro-controller. Messages are forwarded (TX1) and all replies from the next EDFA are received through RX2. TX2 sends replies back to prior containers or to the computers in the laboratory.

whose header does not contain the corresponding address to the next container or to the computer one of the two laboratories. The same applies for the replies such as status messages or alerts. This way, all EDFAs along the link are daisy-chained such that they can be controlled from both ends from the PTB and MPQ laboratories.

The availability of a remote control turned out to be far more important than initially supposed. Intended as a failure-identifier it was a precious tool to fine-adjust the EDFAs and thus to avoid signal breakdowns due to lasing to a large extent. This was a prerequisite for phase coherent measurements over several hours that led to extremely high long-term link stability (see next Chapter 5).

After careful installation and testing of all repeater equipment and also of the remote control, a first transmission signal was detected in February 2010. The beat note between the transmitted laser from PTB and the local MPQ laser is shown in Fig.4.15. A few weeks later, the full distance was stabilized for the first time.

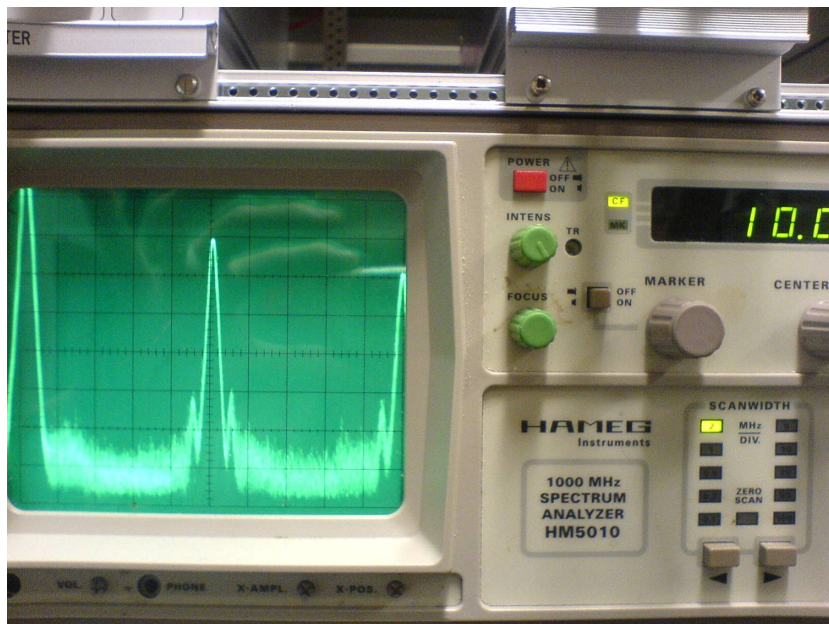


Figure 4.15: *First beat signal between the PTB laser transmitted via 920 km fiber and the local MPQ laser measured with a HAMEG spectrum analyzer with 20 kHz bandwidth.*

Chapter 5

Optical Frequency Transmission over 920 km with 10^{-19} Uncertainty

Both groups at MPQ and PTB have investigated frequency transmission on various loop-shaped test links of up to 500 km length that will be described in the following. The characterization of the full 920 km link between MPQ and PTB is discussed in the second half of this chapter and can further be reviewed in [106].

5.1 Characterizing Test Links of up to 500 km

A common method to characterize fiber links is to have provider and remote user in the same laboratory. Here, transfer and local frequency are provided by the same laser system and the measured self-heterodyne beat note contains information about the fiber link noise while laser phase noise fully cancels. The setup is shown in Fig.5.1.

5.1.1 2m Link: Fiber Stabilization Noise Floor

Short term phase fluctuations due to mechanic vibrations and temperature fluctuations in the out-of-loop fiber parts can easily decrease the stability of the fiber noise cancellation scheme by a factor of ten. For that reason, the MPQ fiber interferometer was designed to have short fiber lengths between the components. Spliced connections further avoid back-reflections that might cause interference and hence amplitude modulations. The interferometer has been placed in an aluminum box lined and covered with foam for further isolation. To characterize the fiber interferometer noise floor, a 2 m loop-shaped link was formed by directly connecting the two fiber-coupled AOMs.

The short term stability of the remote signal has a value of 2×10^{-17} (ADEV) in one second. Towards longer integration times τ , it follows a slope with an inclination slightly smaller than τ^{-1} (see Fig.5.2) which is approximately a factor of three higher than the

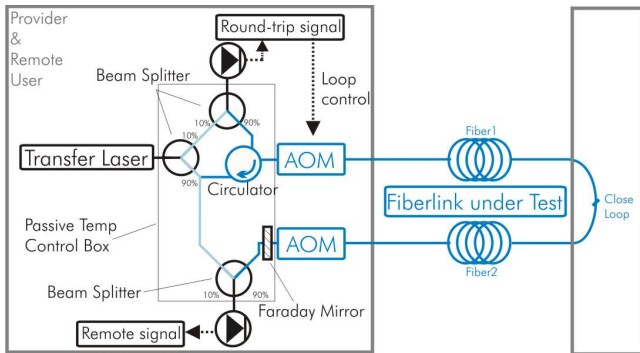


Figure 5.1: Setup to characterize the stability of an actively stabilized link using two fibers. The fibers are connected to form a loop (dark blue) and part of the transfer laser light is split as reference (light blue). Thus, provider and remote user are located in the same laboratory which cancels the influence of transfer laser noise.

counter resolution of $6 \times 10^{-18} \text{ s}\tau^{-1}$ (see Fig.5.3). After 1000 s, a slow temperature drift of the out of loop fibers becomes dominant. This drift might in future be better controlled by active temperature stabilization if required.

At PTB, components with 3mm thick fiber cables and additional housing were employed which resulted in a similar stability curve [83].

The round-trip signal used to extract the fiber noise information (see previous Chapter

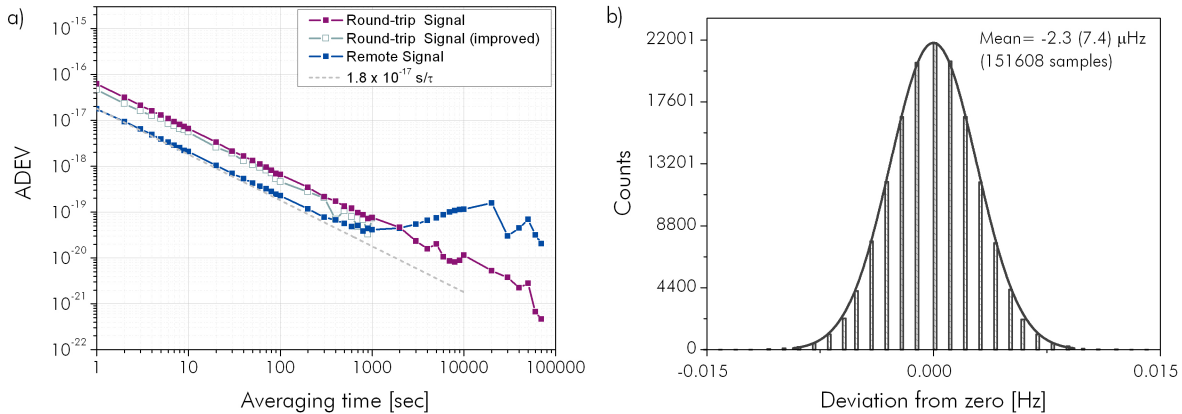


Figure 5.2: Interferometer noise floor of the Doppler-noise cancellation scheme as measured at MPQ: a) Allan standard deviation of the 10 MHz remote signal and the 20 MHz round-trip signal. The radio frequencies are determined by the sum of the AOM frequencies. The round-trip signal's instability of 6.3×10^{-17} was a factor 1.5 higher compared to what one would expect (see text). This was attributed to not perfectly balanced interferometer arms. Careful re-design with special attendance to equal and short uncompensated fiber paths resulted in an improved stability of 4.7×10^{-17} in one second. b) Remote signal deviation from 10 MHz and corresponding normal distribution. The frequency counting was discretized which caused the gaps in the histogram (Data taken at MPQ with continuous Π -type frequency counters, 1s gate time).

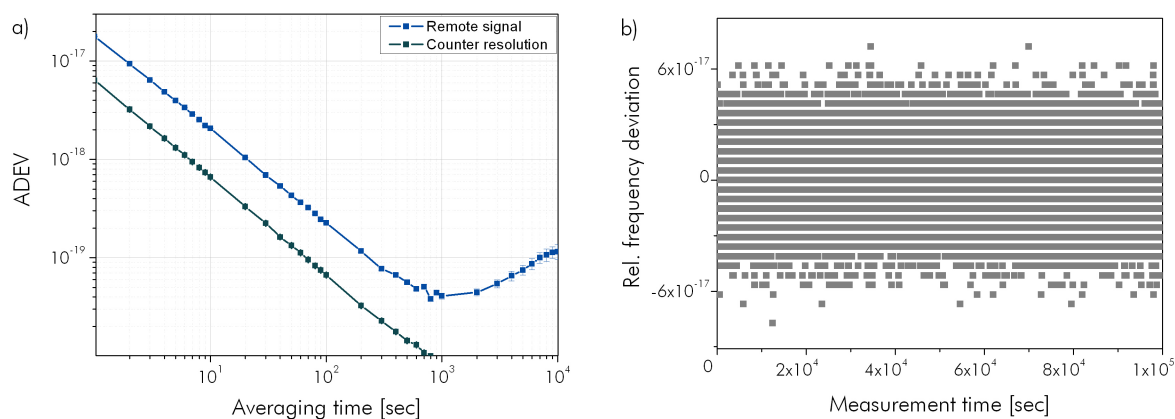


Figure 5.3: a) Stability of the remote signal in comparison to counter resolution. The counter resolution was measured by using the same H-maser as signal as well as reference (see Chapter 2.1.3). Since the counter resolution is 1 mHz the values are discretized (b)) (Data taken at MPQ with continuous Π -type frequency counters, 1s gate time).

4) is expected to be 3 dB less stable than the remote signal as it accumulates the residual phase-noise exactly twice while traveling twice the way. The measured value of $4.7 \times 10^{-17} s\tau^{-1}$ agrees well with this prediction.

The mean deviation between transmitted and local frequency was $-2.3(7.4) \mu\text{Hz}$, consistent to zero deviation. This corresponds to a relative accuracy of better than 3.8×10^{-20} .

The results show that a highly stable and accurate clock comparison with instabilities of less than $10^{-16} s\tau^{-1}$ is achievable for short fiber links that for example connect neighboring laboratories. This method was successfully applied in [2] over a distance of ~ 70 m to compare the -as of 2012- world's most precise optical clocks with a clock- determined stability of $2.8 \times 10^{-15} s\tau^{-1/2}$ (overlapping ADEV) and a residual uncertainty of $1.8 (0.7) \times 10^{-17}$.

5.1.2 10 km Link to Garching Computing Center

The MPQ Internet connection to the Garching computing center (RZG) comprises 10 single mode fibers that are currently not in use for regular data traffic. These fibers were alternately looped in a way to form a zigzag link that began and ended in the same laboratory. This link was the first test stretch at MPQ side.

The residual instability was as low as $8.5 \times 10^{-16} s\tau^{-1}$ as shown in Fig.5.4a). The stability of the round-trip signal is $1.4 \times 10^{-15} s\tau^{-1}$, about a factor 2 higher than the remote signal. The optical frequency was transmitted with a statistically limited accuracy of $360 \mu\text{Hz}$ or 1.9×10^{-18} (see Fig. 5.4b).

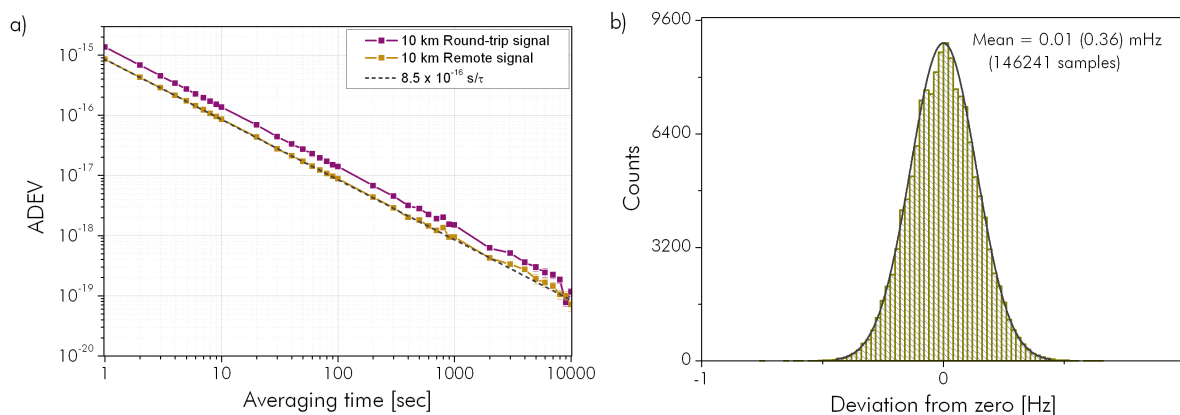


Figure 5.4: *Residual instability of the 10 km remote and round-trip signal at MPQ . b) Remote signal deviation from nominal value and corresponding normal distribution (Data taken at MPQ with continuous Π -type frequency counters, 1s gate time).*

5.1.3 50 km Link around Braunschweig

The very first tests at PTB side were performed in collaboration with the local energy supplier *EnBs* that provided a 50 km fiber link around Braunschweig. The link was only partly laid underground of Braunschweig city which represents a realistic scenario for urban frequency comparisons. The measurements are shown in Fig.5.5. It can be seen that the round-trip signal is not 3 dB less stable than the remote use signal as expected. This indicates that the locking electronics was not optimized and the gain was insufficiently low. However, the stability of $7.7 \times 10^{-15} \text{ s}\tau^{-1}$ was remarkably good even at this early stage of the experiment, motivating further investigations.

Distances of several kilometers represent typical on-campus distances. Different faculties

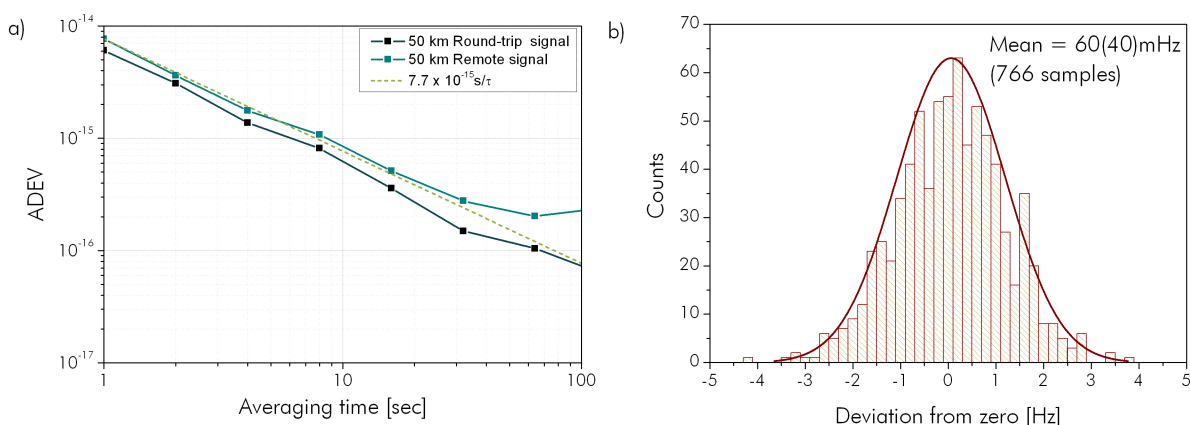


Figure 5.5: *Residual instability of the 50 km remote and round-trip signals around Braunschweig. b) Remote signal deviation from nominal value and corresponding normal distribution (Data taken at PTB with continuous Π -type frequency counters, 1s gate time).*

could take advantage of a reliable frequency distribution system that provides highly stable references for various types of experiments as e.g. realized by [107] at MPQ. Typically, the whole campus area is linked via a research fiber network that is administrated by the local computing center. The connections are usually easy to implement and cost-effective.

5.1.4 146 km Link from PTB to University of Hanover and back

Parallel to the development of the 920 km PTB-MPQ fiber link, PTB and Leibnitz University Hanover (LUH) have set up two 73 km dark fibers for the comparison of two optical frequency standards [108]. The characterization of these two link was published in [83] and is shown in Fig.5.6. At LUH, one bi-directional low-noise EDFA was implemented. Frequency transmission could be performed with a fractional instability of $3.3 \times 10^{-15} \text{ s}\tau^{-1}$. The mean frequency deviation induced by the transmission was determined to be $1.2 (3.6) \times 10^{-20}$ by evaluating 5 measurements each lasting $\sim 55,000$ s. As of today, this is the lowest uncertainty reported for frequency dissemination using optical fiber links.

The same link configuration has successfully been utilized to compare the optical clock lasers of the Yb^+ and Ca frequency standards at PTB [87] that are located in different laboratories: Their relative instability is known from direct comparison using 300 m stabilized fiber (see Fig.5.7, yellow curve). The NIR laser frequency stabilized to the Ca clock laser has been transmitted via the 146 km link and compared to the Yb^+ clock laser.

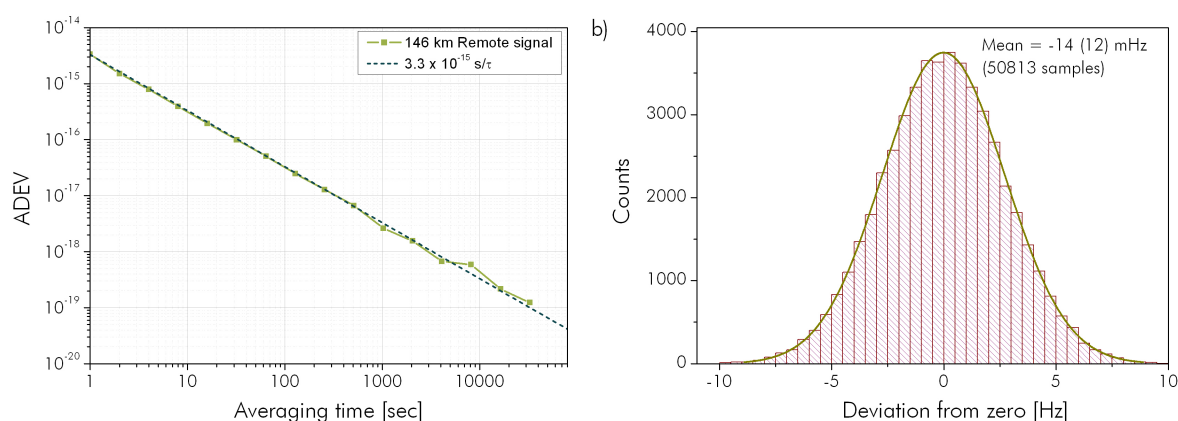


Figure 5.6: Residual instability of the stabilized 146 km remote signal from PTB to LUH and back. One low-noise EDFA was installed at LUH which is half the distance. b) Remote signal deviation from its nominal value and corresponding normal distribution (Data taken at PTB with continuous Π -type frequency counters, 1s gate time).

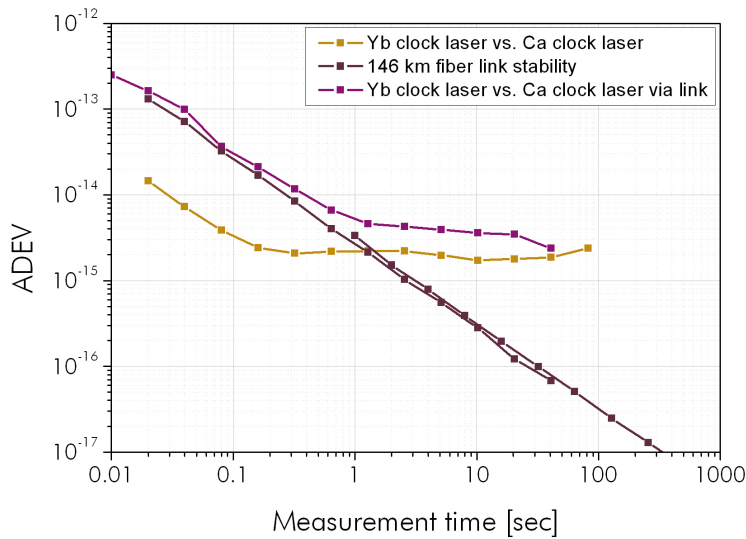


Figure 5.7: Comparison of two optical clock lasers at PTB: direct comparison (yellow curve) and comparison via the looped 73 km fiber link between PTB and LUH (purple curve). After a few seconds of integration time, the link becomes negligible (Data taken at PTB with continuous Π -type frequency counters, 1s gate time) [87].

At short averaging times < 1 s this measurement coincides with the measured instability of the stabilized 146 km fiber link of $\sigma_y(\tau) = 3.3 \times 10^{-15} \text{ s}\tau^{-1}$ (see Fig.5.7, purple curve). Within several seconds of averaging time the contribution of the fiber link to a clock comparison becomes negligible and the optical clock lasers can be compared directly.

5.1.5 172 km Link from MPQ to Münchsmünster Repeater Station and back

To set up the next test stretch from MPQ side, the first repeater station 86 km north of MPQ has been equipped with an EDFA and a loop was formed using the two fibers. The total link length was thus 172 km beginning and ending in the MPQ laboratory.

Fig.5.8 shows the short term stability for frequency transmission over the stabilized link of $2.6 \times 10^{-15} \text{ s}\tau^{-1}$. This is in good agreement with the results of the PTB-LUH-PTB link. The relative uncertainty of the transmission is $4(50) \times 10^{-18}$.

The above described fiber links are appropriate to bridge typical distances between academic institutions located in neighboring cities as shown by the clock laser comparison described above or the one reported in [84]. They have demonstrated performances by far sufficient for comparing optical clocks within very short integration times.

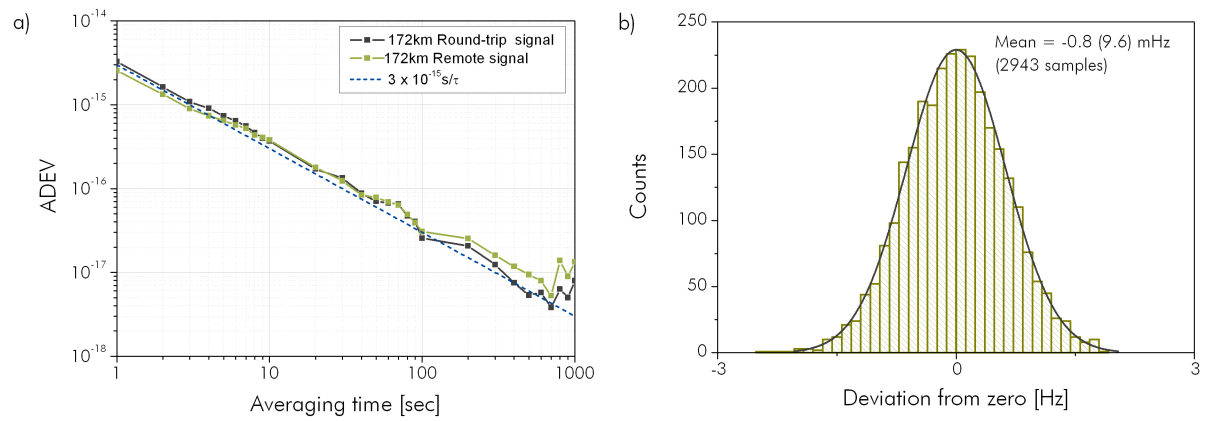


Figure 5.8: Residual instability of the stabilized 172 km remote and round-trip signals to the first southern container station Münchsmünster and back. The performance is comparable to the PTB-LUH-PTB link. b) Remote signal deviation from its nominal value and corresponding normal distribution (Data taken at MPQ with continuous Π -type frequency counters, 1s gate time).

5.1.6 480 km Link from PTB to LUH to PTB to Cörmigk Repeater Station and back

The fiber Brillouin amplifier technique has been developed and tested at PTB [85]. For characterizing the amplification, a 480 km fiber link reaching from PTB to Cörmigk Repeater Station and LUH was setup and stabilized using a single FBA.

The stability of the transferred frequency reaches $\sigma_y(t) = 2 \times 10^{-14} \text{ s } \tau^{-1}$ (ADEV) (see Fig.5.9). Comparing the achieved instability with the previous measurements over 146 km and 172 km shows very good agreement with the scaling law ($\sigma_y(t) \propto L^{3/2}$) derived in [100] (see also Appendix E) .

The mean value of the transmitted frequency is shifted from the reference laser frequency

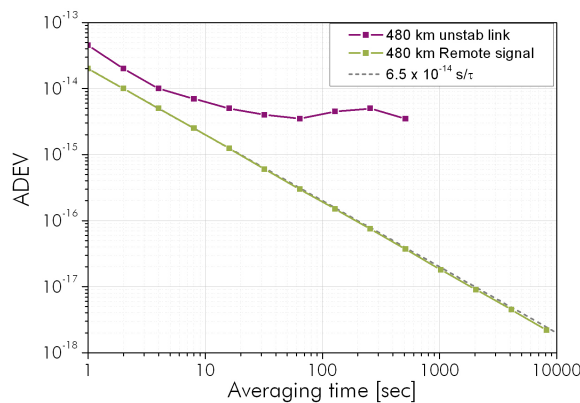


Figure 5.9: Residual instability of the un-stabilized and the stabilized 480 km links from PTB to Cörmigk Repeater Station to PTB to LUH and back [85].

by $64 \mu\text{Hz}$ with a statistical uncertainty of $54 \mu\text{Hz}$. This corresponds to a fractional frequency deviation of 3×10^{-19} .

5.1.7 512 km Link from MPQ to University of Erlangen

The third repeater station as seen from MPQ side is not located inside a container but at the computing center of University of Erlangen. Passing the containers in Münchsmünster and Beilngries a last test link was set up that comprised six EDFAs and had a total length of 512 km. The EDFA remote control as described in the previous Chapter 4 was employed for the first time.

The measurement results are shown in Fig.5.10. It can be seen that the stability of the transmitted signal of $6.5 \times 10^{-14} \text{ s}\tau^{-1}$ is less stable than in the previous experiments and does not follow the $L^{3/2}$ scaling law as proposed in Section 4.5. The increased runtime of the light in combination with inappropriate modification of the loop electronics resulted in an excess phase noise produced by the loop itself. Furthermore, the concatenation of several EDFAs led to signal breakdowns and thus to cycle slips as described in the previous Chapter 4. Both issues were understood later and solved for the 920 km link measurements.

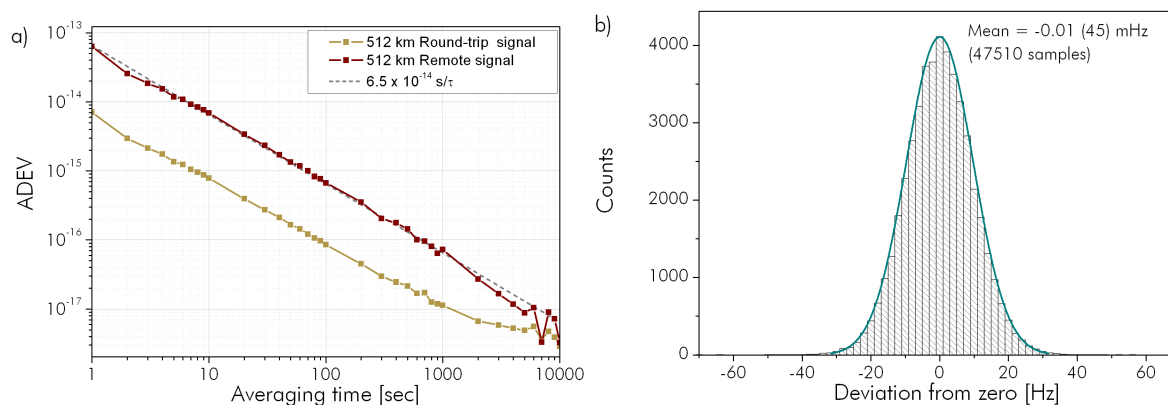


Figure 5.10: *Residual instability of the stabilized 512 km remote signal to University of Erlangen and back. Later understood runtime restrictions resulted in excess phase noise induced by the loop control. b) Remote signal deviation from its nominal value and corresponding normal distribution.*

5.2 Characterizing the Full 920 km Distance

Fiber loop test setups characterize the performance of the looped link, but do not allow for a frequency transfer between two remote users. In the case of the full fiber link stretch, two largely identical, but independent setups have been employed for comprehensive characterization of the frequency transfer between MPQ and PTB.

5.2.1 Setup

The setup to characterize the full 920 km distance with all building blocks described in Chapter 4 is shown in Fig.5.11. Having two identical fibers at hand allows for a widely redundant investigation of the link systematics. Two configurations, anti-parallel and parallel signal transmission using the fibers $F1$ and $F2$, have been tested.

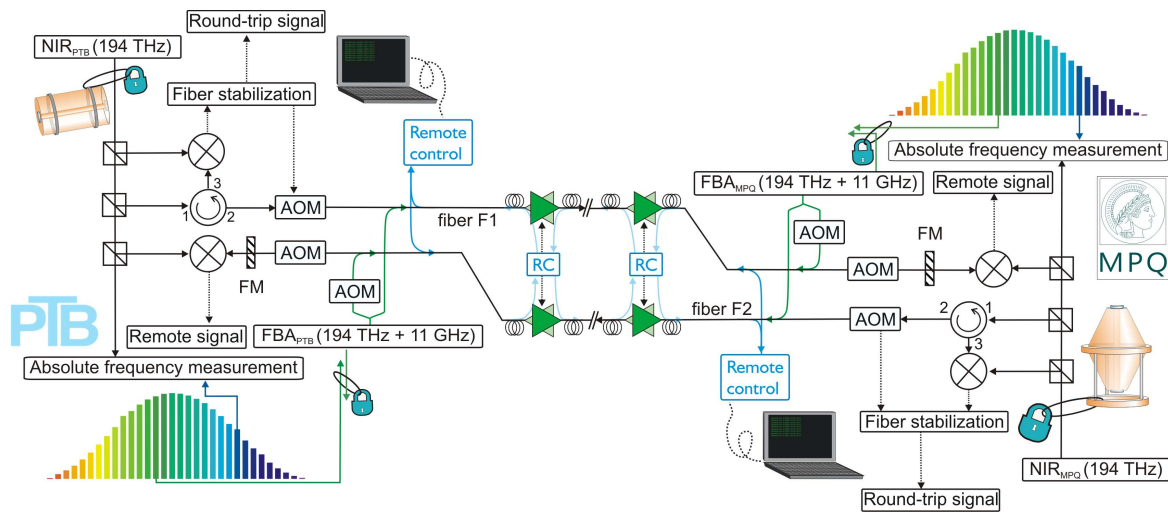


Figure 5.11: *Experimental setup for the characterization of two 920 km fiber links in anti-parallel configuration. See text for description.*

5.2.2 Un-stabilized Link

Since the fibers are buried below ground (see Chapter 4) they are widely unperturbed and the short-term stability of the un-stabilized link is better than 10^{-13} . However, as can be seen from Fig.5.12, on longer time scales temperature fluctuations become dominant resulting in a flicker floor of approximately 10^{-14} . The figure shows the round-trip signal of fiber F_1 as measured in April 2011. The round-trip signal was chosen in order to be independent from the laser drift. The transmitted frequency deviates by $-1.9(0.1)$ Hz from the local frequency. Deviations from up to ± 10 Hz have been observed. This is attributed to the annual temperature variations described in Section 4.5. The observed values are in good agreement with the estimations.

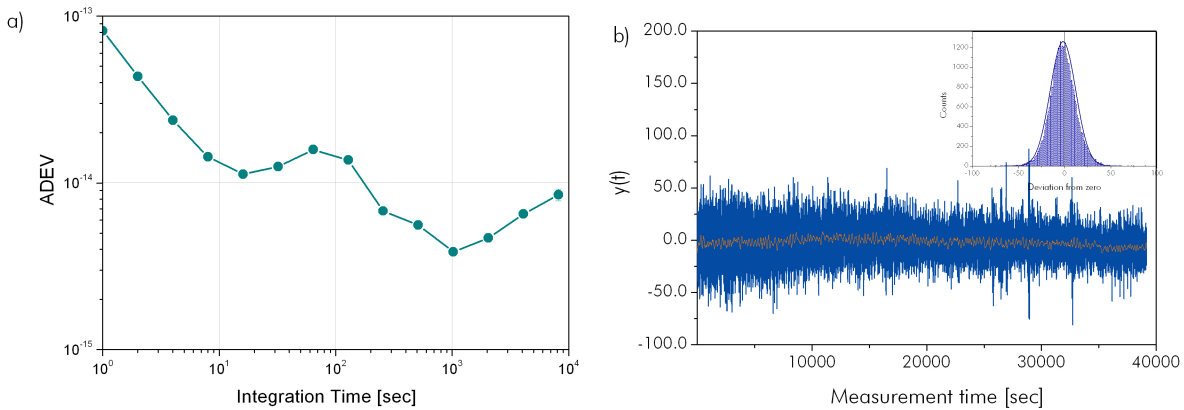


Figure 5.12: a) Allan deviation of round-trip signal sent along the un-stabilized 920 km link and back ($F1$, April 2011). b) Corresponding time-trace. A 100pt moving-average is shown to reveal the frequency fluctuations. The histogram is normally distributed but the mean is slightly shifted from zero (Data taken at MPQ with continuous Π -type frequency counters, 1s gate time).

5.2.3 Antiparallel Configuration

In the antiparallel configuration Fiber $F1$ has been used to transmit the optical frequency f_{PTB} of NIR_{PTB} to MPQ. $F1$ is actively stabilized in one single stretch and comprises 9 EDFAs. At MPQ, a heterodyne beat note $f_{F1} = f_{MPQ} - (f_{PTB} + \delta f_{Link_{F1}})$ is measured. Likewise, f_{MPQ} is transmitted via the actively stabilized fiber $F2$ from MPQ to PTB to generate a beat note $f_{F2} = f_{PTB} - (f_{MPQ} + \delta f_{Link_{F2}})$.

Calculating the difference $\Delta f_{\equiv} = f_{F1} - f_{F2}$ is equivalent to creating a virtual loop: the laser frequencies cancel while the noise δf_{Link} of both fibers adds. From that, an upper limit can be derived for the residual instability of each transmitted frequency. It depends on the degree of correlated noise in both fibers, as will be discussed below.

In this configuration all sources of common mode systematics are widely eliminated. Remaining contributions are highly correlated systematic effects affecting the transmission on $F1$ and $F2$ with opposite signs (the only known example would be the gravitational red-shift). It will need high-performance optical clocks at both ends of the link to substantiate the results for the transmission uncertainty derived below.

Timing Synchronization

Due to a slow relative laser drift with rate α any timing offset Δt between the frequency counter gate times at PTB and MPQ leads to an apparent frequency shift between the two signals f_{F1} and f_{F2} :

$$\Delta f = \alpha \times \Delta t \quad (5.1)$$

Unfortunately, the counters used in this experiment did not provide the opportunity to synchronize them externally. Hence, the synchronization offset Δt was determined from the measured frequency offset after applying a strong artificial well known frequency modulation α and measuring the corresponding frequency offset (see Fig.5.13). For the frequency comparison the relative frequency drift α was determined for every data point. Finally, the measured frequency difference between the signals $f_{F1}(t)$ and $f_{F2}(t)$ was corrected.

The uncertainty of the synchronization offset was determined to be 0.1 ms and Δt was periodically checked over the entire measurement period. For correction, the relative frequency drift α is determined for every data point and the measured frequency difference between the signals f_{F1} and f_{F2} is corrected accordingly. Without correction, a typical linear drift of the NIR frequencies of up to 100 mHz/s and an observed synchronization offset $\Delta t = 0.3$ s would lead to a systematic fractional frequency offset of 1.5×10^{-16} . After correction, it contributes less than 3 parts in 10^{19} to the total uncertainty.

Fig.5.14 shows the impact of the drift correction to $\Delta f_{\rightleftharpoons}$. For reasons that will be described below, phase-coherent intervals have been averaged as if measured with a 1000 s gate time. Since the drift is not linear, it is insufficient to apply a constant correction term to the averaged values. Rather, the 1 s values are corrected individually and averaged afterwards.

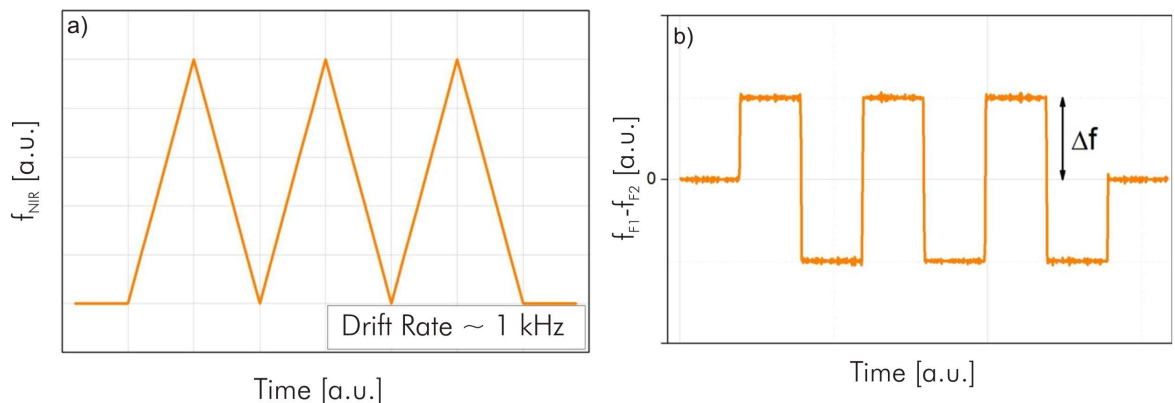


Figure 5.13: *Determination of the timing offset between two frequency counters. Applying a strong modulation to a signal that is measured with both counters (a) results in a frequency offset that allows for calculating the timing offset according to Eq.5.1 (b).*

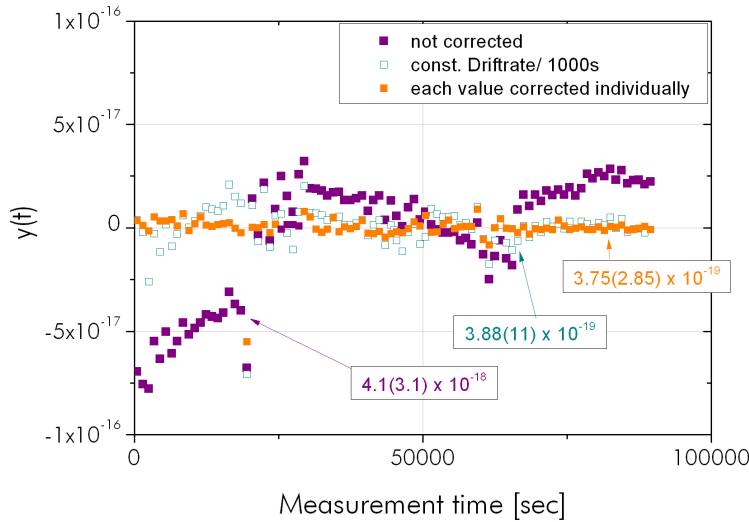


Figure 5.14: Influence of the drift correction to Δf_{\equiv} averaged as if measured with a 1000 s gate time. It can be seen, that a residual scattering of the data remains if a linear drift is assumed over each full 1000 s interval.

Data Acquisition

All frequency data have been measured as described in Section 2.1.3. Dead time free Π -type as well as Λ -type counters from $k\mathcal{E}k$ (FXM, FXE, FX80) with 1 s gate time have been used. The following signals have been recorded during each measurement at both ends of the link at PTB and MPQ:

- 1.) f_{F1} and f_{F2} (Comparison of local and transmitted laser)
- 2.) $f_{F1_{rt}}$ and $f_{F2_{rt}}$ (Frequency of the round-trip signal used to stabilize the fibers)
- 3.) $f_{NIR_{PTB}}$ and $f_{NIR_{MPQ}}$ (Absolute frequency of each transfer laser)
- 4.) Fiber stabilization AOM control signals at PTB and MPQ

For Cycle-Slip detection, Λ -type counters have turned out to be mandatory as the noise band of the data using Π -type counters was too broad to reveal cycle slips on the required confidence level. As discussed in Section 2.1.3, Λ -type counters average the data in analogous manner as the modified Allan deviation and hence suppress white phase noise very efficiently. Other types of noise and in particular cycle-slips are widely unaffected by this averaging method. This is the reason, why Λ -counters can discover cycle-slips that were originally hidden in the un-filtered data. For data evaluation, the following cycle-slip criteria have been well-proven:

- 1.) Transfer laser redundancy: The beat notes f_{F1} and f_{F2} are counted twice. The difference must be smaller than ± 0.5 Hz.
- 2.) Fiber stabilization: Round-trip signals equal 30 MHz ($F1$) and 20 MHz ($F2$) within 1 Hz, respectively.
- 3.) Time axis continuity: Comparison of recorded computer time to number of data

points ¹.

All data points that did not meet these criteria were discarded. On the other hand, no valid data points were ignored even when looking suspicious.

Under optimized conditions the rate of cycle-slips has been as low as a few per day and the signal phase could be continuously tracked for several hours. The main reason for cycle-slips is caused by changes in the polarization state of the fiber laser outputs or the fibers that are not actively stabilized such as for example the reference arm of the fiber noise interferometer. This results in a poor signal-to-noise ratio for both the round-trip and the remote signal. Regular adjustment is thus required to maintain optimized operation over several hours. In future, this may be automatized by active polarization stabilization.

Results: Stability

The fractional instability of the stabilized link is shown in Fig.5.15. The ADEV of $3.8 \times 10^{-14} \text{ s}\tau^{-1}$ of the stabilized link as shown for a 35000 seconds long dataset is due to the residual broadband fiber-noise. It drops off as τ^{-1} as expected for a perfectly phase stabilized fiber link. This agrees excellently with the $L^{3/2}$ scaling law when compared to the 150 km and 480 km fiber links investigated earlier. The Π - counter also allows for the calculation of the modified ADEV which is helpful to distinguish white phase noise from flicker phase noise. Fig.5.15 shows that the residual instability is mainly dominated by the former.

To demonstrate the link's instability floor and illustrate the potential of adapting the type of averaging to the dominant noise type, the signals were additionally measured with Λ -counters. As shown in Fig.5.15 for an 18000 seconds long dataset a residual instability (modADEV) of 5×10^{-15} in one second has been derived this way. It averages as $\tau^{-3/2}$ for up to 100 seconds and reaches 10^{-18} in less than 15 minutes. While the Λ - counter provides increased frequency resolution after 1 s integration time, the flicker floor is revealed at the same stability level independent from the type of counter (see Fig.5.15). The Λ - counter used in this experiment samples the incoming data with a rate of 1 kHz. Hence, one would expect the ADEV curve and the Λ - modADEV curve to cross at 1 ms integration time. This is obviously not the case and may be attributed to the fact, that the measurements were taken at different times (April and August, 2011, respectively).

¹Time traces taken with the FXM Π -counter at MPQ happened to have lost data points (i.e. cycles) from time to time. This has been software related.

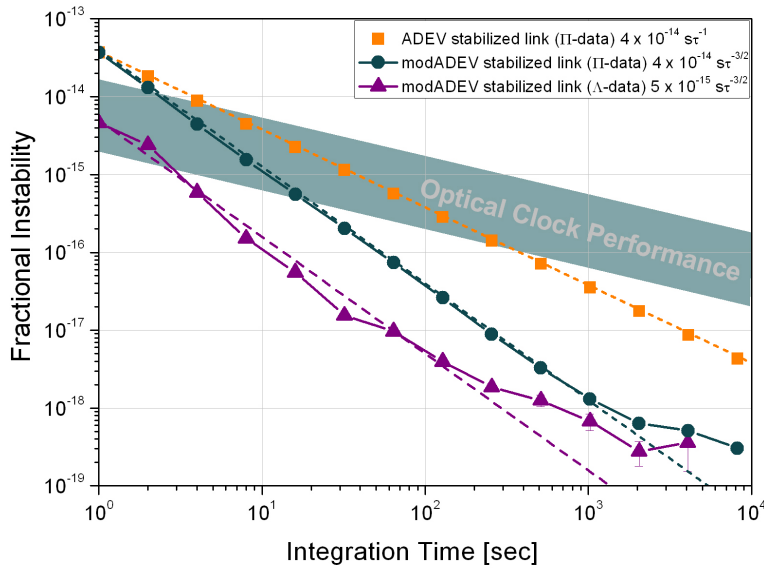


Figure 5.15: *Relative instability of the 920 km fiber link. Data are taken with Λ - as well as with Π - counters. The latter allow for the calculation of both, ADEV and modified ADEV. After 1 s, the Λ - counter shows strong suppression of white phase noise. For comparison, the typical performance of state-of-the-art optical clocks is shown as well.*

The deviation of the fractional instability from the $\tau^{-3/2}$ slope for $\tau > 300$ s is attributed to the MPQ interferometer that had not been optimized for a while and showed a higher temperature sensitivity as compared to earlier measurements. The corresponding uncertainty can be estimated according to Eq.4.4 assuming temperature drifts of 0.5 K / day and a fiber length mismatch of 10 cm. This way, the systematic frequency deviation due to the interferometer can be estimated to be smaller than 3×10^{-19} .

Fig.5.15 demonstrates that the fiber link instability does not contribute significantly to the uncertainty budget of a frequency comparison even of the world's most stable optical clocks [1] over a distance of 920 km.

Results: Accuracy

The accuracy of the transmitted signal may be compromised by systematic offsets that would not be observed in the instability analysis. Over a period of four days, data were taken with a Λ -type counter (see Fig.5.16a), green full circles). All phase-coherent sub-sets having a length of 1000 s were selected and the arithmetic mean was calculated to benefit from the strong suppression of white phase noise for longer integration times (see Fig.5.16a), blue full circles, different scaling!). It should be noted that this kind of averaging may be performed only on phase-coherent data measured with continuous counters that do not exhibit dead-time between two measurement windows (see Section 2.1.3). Here, 1000 s bins turned out to be the best compromise between the number of resulting data points and reduced statistical uncertainty.

The corresponding histograms are shown in Fig.5.16b). 0.1% of the total number of the 1s values were outliers (all having values of approximately ± 200 Hz) that were not identified by cycle-slip detection thus requiring further investigation. Hence, the normal

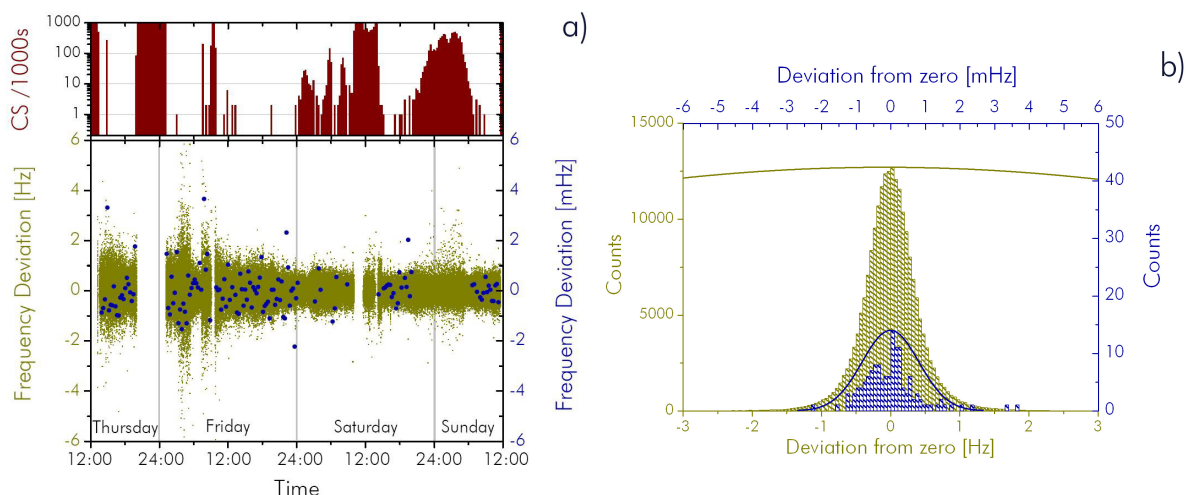


Figure 5.16: a) Four-day frequency comparison between highly stable lasers at MPQ and PTB (green data points, left frequency-axis). Cycle-slip rates per 1000 seconds are shown in the upper plot. Phase-coherent intervals have been binned into 1000 second long sequences and averaged (dark blue, right frequency-axis, enlarged scale). b) Corresponding histograms for the 1s values (green) and the 1000 s means (blue, enlarged horizontal axis). 0.1% of the total number of the 1s values are outliers (all having values of approximately ± 200 Hz) that were not identified by cycle-slip detection. Hence, the normal distribution is greatly enlarged.

distribution is greatly enlarged. Apparently, the outliers have averaged to a large extent after 1000s.

The resulting 135 data points have been evaluated as independent measurements and a statistical mean of $7 (37) \times 10^{-20}$ has been calculated. Thus, any deviations from the expected frequency value after transmission can be constrained to be less than 4×10^{-19} . This value exceeds the requirements posed by the most accurate atomic clocks to date by more than one order of magnitude.

5.2.4 Parallel Configuration: Fiber Noise Correlation

Originally implemented to facilitate the locking optimization, frequency transmission using a parallel link configuration also allowed for investigating the degree of correlation between the two fibers as any common noise cancels: The transfer laser signal was split at MPQ and sent to PTB on both fibers. Both fibers were stabilized independently. Both heterodyne beat notes f_{F1} and f_{F2} between the transmitted and the local NIR have been measured and compared at PTB. In this configuration, the difference $\Delta f_{\Rightarrow} = f_{F1} - f_{F2}$ yields the *difference* of the individual fiber noise contributions rather than the sum.

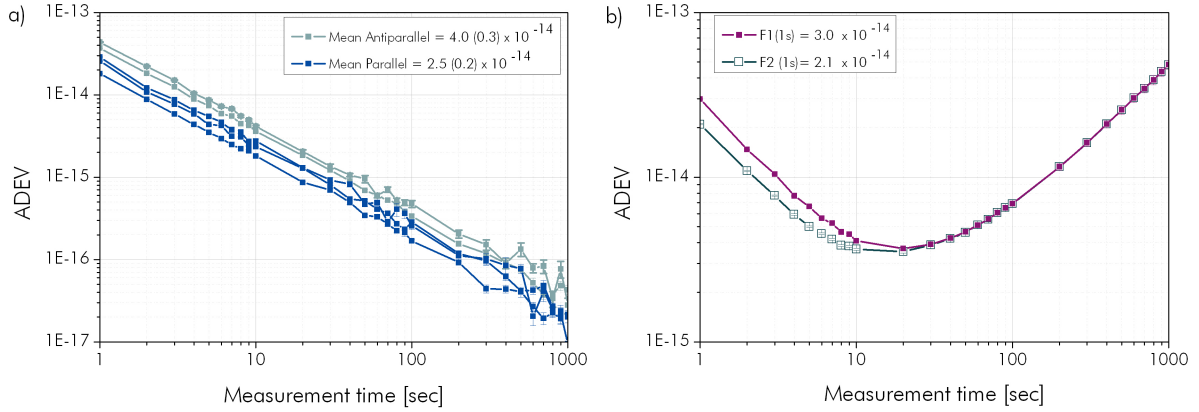


Figure 5.17: a) Relative stabilities of the 920 km fiber link in parallel configuration as compared to the anti-parallel configuration. b) Stabilities of each beat note between local and transmitted laser f_{F1} and f_{F2} . The link noise can be seen only at short integration times τ as the laser drift becomes dominant after approximately 10s.

Stability and Correlation

The typical residual instability of Δf_{\Rightarrow} is in parallel configuration 2.5×10^{-14} and hence a factor 1.6 smaller than Δf_{\Leftarrow} in anti-parallel configuration (see Fig.5.17a). Assuming equal fiber noise contributions ², Δf_{\Rightarrow} should approach zero for fully correlated noise while it should deliver the same 1 s value as Δf_{\Leftarrow} for fully uncorrelated noise.

In order to be independent from the frequency drift of NIR_{mpq} , rather than f_{F1} and f_{F2} the corresponding round-trip signals $f_{F1_{rt}}$ and $f_{F2_{rt}}$ have been evaluated. The linear correlation coefficient $\rho_{X,Y}$

$$\rho_{X,Y} = \frac{\text{cov}(X,Y)}{\sigma_X \sigma_Y} = \frac{\langle X - \bar{X} \rangle \langle Y - \bar{Y} \rangle}{\sigma_X \sigma_Y} \quad (5.2)$$

yields the linear stochastic dependency of X and Y. If the dependency of X and Y is time-shifted, the correlation is rather revealed by the cross-correlation function $R(t')$ than by $\rho_{X,Y}$:

$$R(t') = \int_{-\infty}^{\infty} X(t)Y(t-t')dt \quad (5.3)$$

Fig.5.18 shows a slight dependency $f_{F2_{rt}}(f_{F1_{rt}})$. The corresponding correlation coefficient is $\rho_{F1,F2}=0.25$. The cross-correlation function $R_{F1,F2}(t')$ shows that common noise arises simultaneously in both fibers.

²The instabilities of F_1 and F_2 are related by $\sigma_{F1}(1s) = 1.4\sigma_{F2}(1s)$ (see Fig.5.17b).

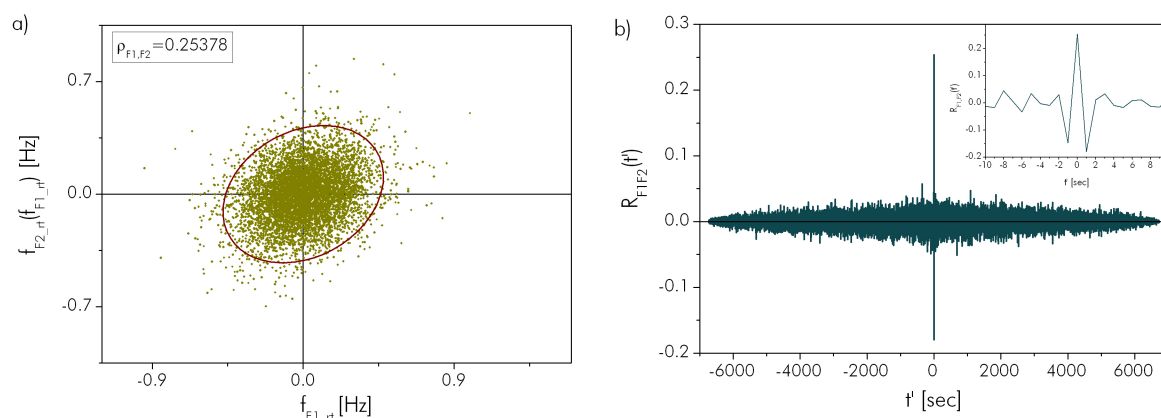


Figure 5.18: Degree of correlation between $F1$ and $F2$. To be independent on laser drift, the round-trip signals have been evaluated rather than f_{F1} and f_{F2} . a) $F2$ as a function of $F1$. The confidence ellipse contains 95% of the data points b) Cross-correlation function $R(\tau)$ between $F1$ and $F2$ showing a sharp peak for un-shifted time traces.

Accuracy

The uncertainty of the frequency transmission using the parallel configuration did not reveal any systematic effects. By evaluating a three day measurement according to the procedure described above a mean frequency deviation after transmission of $6.9 (22) \times 10^{-19}$ was obtained from 72 averaged data points.

5.2.5 Phase Noise Measurements

Fast phase fluctuations have been evaluated by Fourier analysis following the procedure described in Appendix 2.1.4 for the parallel as well as for the anti-parallel configuration (see Fig.5.19). For the parallel configuration, Δf_{\Rightarrow} could be measured directly. However, for the anti-parallel configuration only f_{F1} could be measured, in which the NIR laser noise is still present. In both curves, weak servo bumps arise at $= 48.5(7.5)$ Hz. This corresponds to a round trip time of 10.6 (1.6) ms. From that the link length is calculated to be 1079 (177) km which agrees with the specified link length of 920 km.

For the parallel configuration, phase noise is suppressed by up to 20 dB close to the carrier (0.1 Hz - 5 Hz). The un-stabilized power spectral density $S_{fiber}(f)$ is flat for Fourier frequencies below 1 Hz. As this is not observed in the anti-parallel configuration it may be attributed to common noise that cancels in Δf_{\Rightarrow} but not in Δf_{\Leftarrow} . As according to Eq.4.7 the delay unsuppressed fiber noise limit (see Appendix E) depends on the PSD of the un-stabilized link $S_{fiber}(f)$ it is lower for the parallel configuration than for the anti-parallel configuration.

For the anti-parallel configuration, phase-noise suppression is approximately 10 dB at

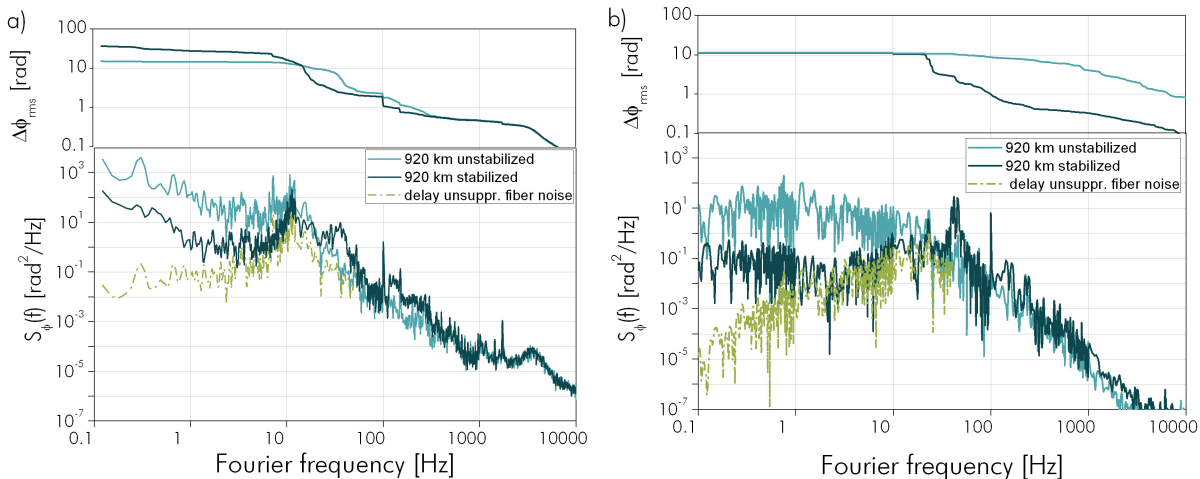


Figure 5.19: *Phase spectral density and rms-phase noise for sum (a) and difference (b) of two optical signals transmitted via 920 km actively stabilized fibers.*

Fourier frequencies within the locking band-width. This may be due to insufficient gain at low Fourier frequencies or caused by laser noise and will need further investigation.

Calculating the 1s ADEV from $S_{remote}(f)$ according to Eq.2.8 gives $\sigma_y(F1, 1s) = 2.2 \times 10^{-14}$. This represents the residual fiber noise on one single fiber. As described above, one would expect $\sigma_y(F1, 1s) = 3.8/\sqrt{(2)} \times 10^{-14} = 2.7 \times 10^{-14}$ for fully uncorrelated fiber noise. Taking into account that the fibers are slightly correlated this is a good agreement with the measured value.

5.3 Discussion

The link now permanently connects MPQ and PTB and is operated routinely. Using two anti-parallel fiber links frequency transmission with a fractional frequency instability (modADEV) of 5×10^{-15} after 1 s integration time has been demonstrated reaching 10^{-18} in less than 1000 s. For long integration times τ the deviation from the expected frequency value has been constrained to within 4×10^{-19} .

The results demonstrate that optical frequency comparisons can be performed even over continental distances with outstanding high stability and accuracy. The short-term stability is strongly limited by the runtime of the round-trip signal and confirms the $L^{3/2}$ scaling law derived in [100]. In future experiments, the short-term stability could be improved by concatenating several servo loops with larger bandwidth.

The measurements further demonstrate the importance of appropriate cycle-slip detection. The scheme applied here has been modified during the course of this experiment in

order to meet the ever increasing accuracy demands. It turned out to be robust against small changes of the CS-thresholds on the achieved uncertainty level. For reaching uncertainties below 10^{-19} , it will likely not provide sufficient confidence and more stringent cycle-slip criteria (such as, for example, three redundancy counters) will be required.

For a phase noise measurement in the time- domain, the choice of the frequency counter depends on the application (provided it has no dead time between the measurement windows). As discussed above, Λ - counters provide improved frequency resolution and hence allow for shorter measurement times. They further allow to calculate the modified Allan deviation that helps to distinguish between white and flicker phase noise which is an important prerequisite for the characterization of phase-locked signals. On the other hand, certain applications may require information about broadband noise or comparability to previous measurements. In this case, Π - type counters along with the well-known Allan deviation could be the better choice. Thanks to the work of [22] and [23] the scalability of the different variances measured with different counters is becoming common knowledge. For example, consider a signal dominated by white phase noise: Measuring the modified ADEV with a Λ -type counter with a sampling rate of 1 kHz should give a factor of $10^{3/2}$ improved stability after 1s as compared to the ADEV measured with a Π - type counter and 1ms gate time. However, this could unfortunately not be observed in this experiment and is surely worth further investigations.

The residual phase noise of two stabilized fibers laid within the same cable duct is weakly correlated. No unidentified systematic effects limit the accuracy at the 10^{-19} level. While leaving room for further improvement the performance is by far sufficient for comparing even the next generation of high-end optical clocks.

Fig.5.20 shows the obtained stability results in direct comparison to those of satellite-based transmission techniques. Going beyond a proof-of-principle experiment conducted under optimized laboratory conditions the 920 km fiber link hence constitutes a solution for the topical issue of remote optical clock comparison.

The fiber link thus allows to fully exploit the accuracy of optical atomic clocks for a variety of applications in fundamental physics such as tests of general and special relativity as well as quantum electrodynamics. Furthermore, this fiber link will enable clock-based, relativistic geodesy at the sub-decimeter level. Applications in navigation, geology, dynamic ocean topography and seismology are currently discussed (see chapter 2.4). Some of the future applications of optical clocks will be space-based and their operation will require ground-stations with access to ultra-stable frequency references linked to the best available clocks. In this respect optical links will also become of central importance.

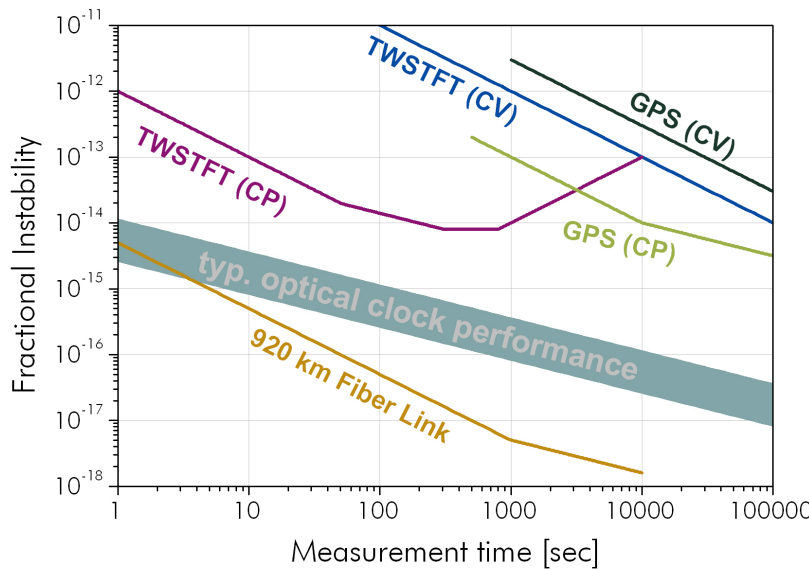


Figure 5.20: Fractional instability (modADEV) of state-of-the-art satellite-based time and frequency transmission [70] in comparison with the results obtained for the 920 km fiber link. Optical clocks can be compared directly for all integration times < 10 s using the link.

Scaling to larger distances will become challenging with an increasing number of bi-directional amplifiers. Though decreasing the distance between two subsequent amplifiers allows for increasing the total link length the limited amount of input power will finally determine the maximum distance that can be bridged using EDFAs [103]. Here, fiber Brillouin amplifiers could be advantageous but require increased technical demand to be operated in-line. Another option could be the installation of in-line stable lasers locked to the incoming signal used as intermediate oscillators that fully clean the signal from noise. These oscillators are preferably operated in a laboratory environment as they require the stabilization to an ultra-stable cavity as described in Chapter 4. This also raises the question about the architecture of a future European fiber network. Serial linking of research institutes is probably the most natural way to grow a fiber network but it may become inconvenient to provide the best clock signals to all remote users. A radial network with centers in Europe's standards institutes would better realize the idea of a frequency distribution service.

Chapter 6

Precision Spectroscopy on Atomic Hydrogen Referenced to a 600 km distant Frequency Standard

As a first application, the 920 km fiber link between MPQ and PTB has been used to measure the 1S-2S two-photon transition frequency in atomic hydrogen at MPQ using PTB's primary Cs-fountain clock (CSF1) as a reference.

The 1S-2S hydrogen experiment constitutes a very accurate test bed for quantum electrodynamics and has been performed at MPQ with ever increasing accuracy [109, 110, 4]. The latest measurements have reached a level of precision at which satellite-based referencing to a remote frequency standard would limit the experiment. As shown in the previous Chapter, the transmission over fiber is orders of magnitude more stable and accurate than even the best microwave clocks (see Chapter 2.2). Hence, using a fiber link a frequency measurement can be carried out straightforwardly without the need for transporting a frequency standard to the experiment. The results presented below can also be reviewed in [4] and [8]. An extensive description of the hydrogen experiment is presented in [111].

6.1 1S-2S Absolute Frequency Measurement

Frequency measurements of the 1S-2S transition and the 2S hyperfine structure in hydrogen and deuterium provide a variety of options for deducing fundamental atomic parameters such as the Rydberg constant, the deuteron structure radius, or the ground-state Lamb shift [112, 113, 114, 115]. Upper limits for a possible variation of the fine-structure constant have been derived [110]. Furthermore, two well-timed measurements of the same frequency were recently used to set new limits on the electron boost Lorentz invariance violation (see below) [8].

6.1.1 Experimental Setup

The experimental setup for the 1S-2S hydrogen experiment has been continuously improved for the last 35 years [120, 4]. The setup for to date latest measurements is briefly described in the following.

The dipole-forbidden 1S-2S transition is interrogated by two-photon absorption of 243 nm laser light. It has a life-time of about 143 ms which corresponds to a narrow natural line width of 1.3 Hz. Therefore, a stable laser system with an adequate amount of power to drive the two-photon transition is required to sample the line.

The spectroscopy laser setup comprises a 972 nm external cavity diode laser system (ECDL) that is frequency stabilized to a high-finesse ULE-cavity by means of the Pound-Drever-Hall-technique (see Appendix D). It yields a line width of ~ 0.5 Hz reaching a stability of 4×10^{-15} after 1000 seconds. The linear drift at zero crossing temperature was measured to be 50 mHz/s [94].

The laser is quadrupled in two frequency doubling stages to yield 243 nm light. This signal enters an enhancement cavity to form a standing wave for the two-photon transition and also to provide the required excitation intensity of 300 mW per direction (see Fig.6.1). A small fraction of light leaks through the cavity mirrors and is detected by a photo diode attached to an integrating sphere. From this, the intra-cavity power is determined and the line spectra calibration can be carried out.

Part of the stabilized 972 nm light is measured against the corresponding mode of a 250 MHz fiber laser-based frequency comb in order to relate the hydrogen resonance to

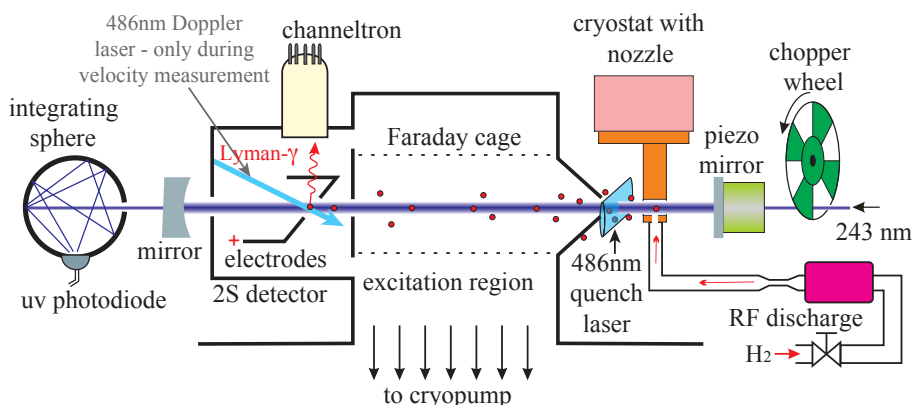


Figure 6.1: *Hydrogen spectrometer setup: Hydrogen atoms are dissociated by rf-discharge and then cooled down to cryogenic temperatures. 2S-atoms are detected by mixing the 2-S state with the 2P-state that decays via emission of Lyman- α photons [4].*

6. Precision Spectroscopy on Atomic Hydrogen Referenced to a 600 km distant Frequency Standard

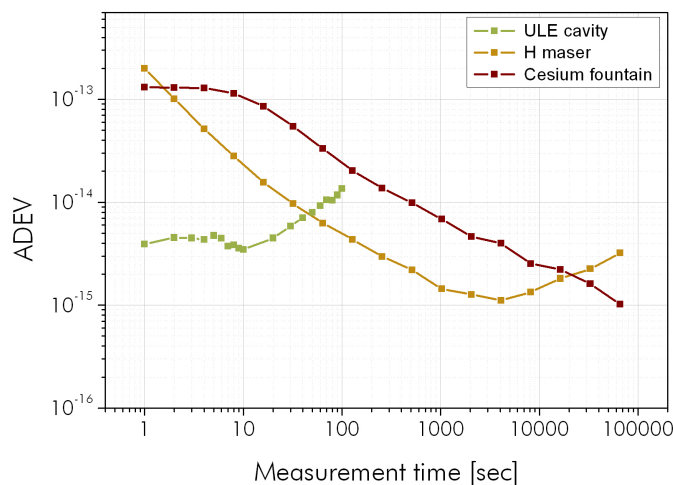


Figure 6.2: *Referencing the MPQ H-maser: The laser cavity has the lowest short-term instability but shows a strong drift. The plot shows the direct comparison of two cavity stabilized lasers with a linear drift subtracted. The maser provides better stability after 10 s. However, after ~ 10000 sec a slow drift becomes dominant. After this crossing point the Cs-clock represents the best reference.*

the microwave-reference (see Appendix B.2). The most precise rf-reference in the laser spectroscopy division at MPQ is a hydrogen maser (see Fig.6.2, yellow curve). Due to a slow drift, it is necessary to correct the maser frequency on long time scales to a more accurate reference such as a cesium fountain clock (see Fig.6.2, red curve). To optimize the referencing, the maser is additionally measured against the ULE-cavity stabilized laser for short integration times < 10 s. The Cs-fountain clock was previously provided by the portable FOM [74] (see 3.2) for all hydrogen measurement campaigns until May 2010. The latest measurement in November 2010 was referenced to PTB's primary Cs fountain clock [35] using the fiber link (see below).

A microwave discharge provides the needed dissociation energy that isolates the hydrogen atoms. Their subsequent path in the experiment is shown in Fig.6.1: To slow the atoms down they are cooled to 5-7 Kelvin by a copper nozzle. Directly after the nozzle, a 486 nm quench laser de-excites 2S-atoms produced within the nozzle. This 'reset' reduces the dc-Stark as well as the pressure shift that are both not controlled within the nozzle.

The cold 1S-beam then propagates along the optical axis of the enhancement cavity into the detection region. A graphite coated Faraday cage shields the atoms against stray electric fields to reduce the dc-Stark effect.

To scan the atomic line the laser frequency is randomly shifted across the resonance by a double-pass AOM. For detection, the 2-S state is mixed with the 2P-state by a dc electric field (10 V/cm). The 2P-state promptly decays into the ground state emitting a Lyman- α photon that is detected by a solar-blind photo-electron multiplier tube. The count rates of the multiplier are recorded in direct relation to the scanned laser frequency.

All beat signals for the absolute frequency measurement have been recorded with continuous Λ -counters to yield advanced frequency resolution (see Appendix 2.1.3). For cycle-slip detection, all signals have been counted redundantly. A comb-comb comparison has proven that the detection scheme is able to identify cycle slips with a sufficient reliability for this experiment [90].

6.1.2 Uncertainty Budget

The two major systematic effects that are currently limiting the accuracy of the 1S-2S experiment at MPQ are the 2nd order Doppler shift and the quadratic AC-Stark shift that contribute as 1.1×10^{-15} and 2.4×10^{-15} to the uncertainty budget, respectively.

The next significant contribution is given by the cesium reference with a relative uncertainty level of $\sim 8 \times 10^{-16}$. This clearly shows how close the accuracy of hydrogen spectroscopy experiment to the accuracy limit of rf-clocks has been pushed.

6.1.3 Results May 2010

In May 2010, the centroid of the 1S-2S transition frequency in atomic hydrogen was determined to be

$$\nu_{1S-2S}^{May} = 2\,466\,061\,413\,187\,035\,(10)\text{ Hz}$$

This has been a threefold improvement in accuracy compared to previous measurements at MPQ and represents the most accurate value of the 1S-2S transition frequency in atomic hydrogen as of today (see Fig.6.6 on page 81).

6.2 1S-2S Absolute Frequency Measurement in Units of CSF1 at PTB

6.2.1 Frequency Map

In order to link the hydrogen maser at MPQ to the cesium clock at PTB the transmission scheme described in Chapter 4 was used. The frequency map that illustrates the conversion from the rf-clock signals to the transfer laser frequencies is shown in Fig.6.3.

Both rf-clocks are linked to the transfer laser systems using femtosecond frequency combs. At MPQ, comb and transfer laser are located in different laboratories connected via a phase noise compensated optical fiber of approximately 50 m length. The measurement was performed using the parallel link configuration (see Section 5.2).

6. Precision Spectroscopy on Atomic Hydrogen Referenced to a 600 km distant Frequency Standard

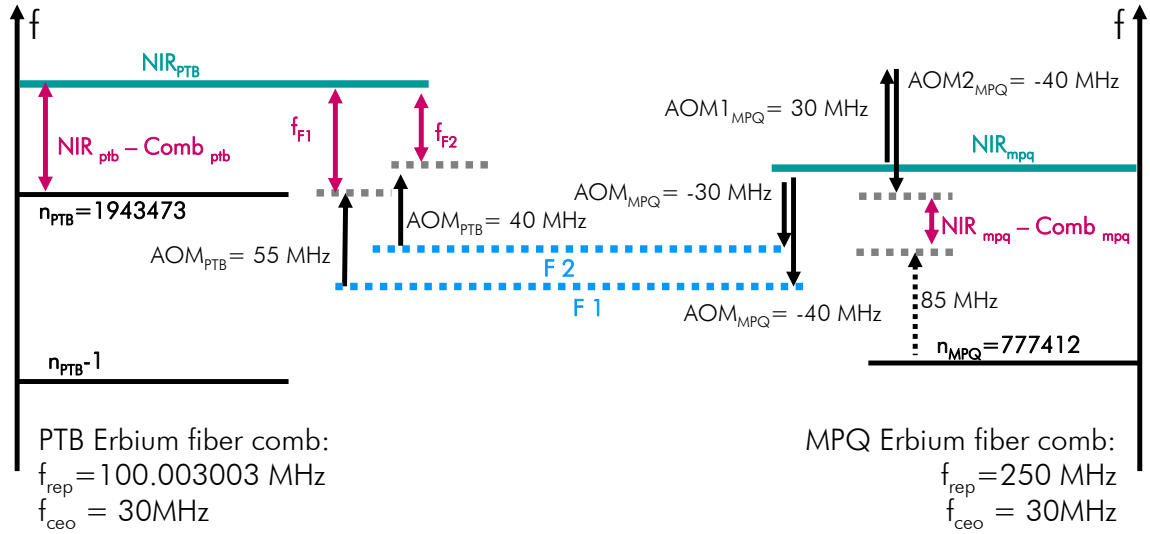


Figure 6.3: *Frequency map for the correction of MPQ's H-maser to PTB's Cs-fountain as required for the absolute frequency measurement of the 1S-2S transition in atomic hydrogen (not to scale). Both rf-clocks are linked to the transfer laser systems using femtosecond frequency combs as described in Chapter 4.*

The H-maser fluctuations in units of CSF1 can be derived by measuring the absolute frequency NIR_{PTB} at PTB and at MPQ in units of the respective local rf reference. Taking into account all fixed radio frequencies such as AOMs and rf-synthesizers shown in Fig.6.3 yields:

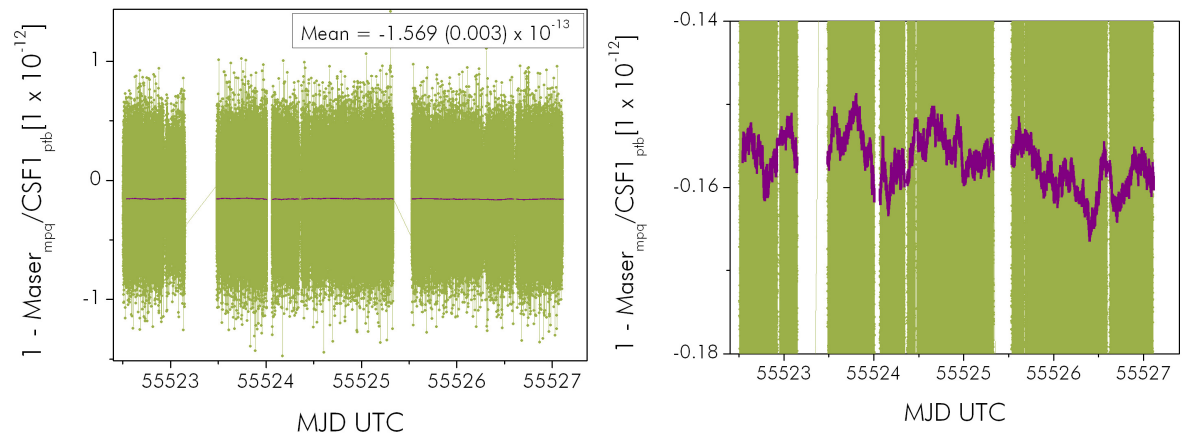


Figure 6.4: *Comparison of the MPQ hydrogen maser to PTB's primary Cs-fountain clock CSF1 during the 1S-2S measurements in November 2010 (green curve) and 10,000s moving average (purple curve). Left: time trace in full scale. Right: $75 \times$ zoom to better illustrate the H-maser fluctuations.*

$$1 - \frac{f_{maser}}{f_{CSF}} = \frac{NIR_{PTB} - NIR_{MPQ} - f_{F1}}{1.94353206 \times 10^{14} Hz} \quad (6.1)$$

6.2.2 Results November 2010

The absolute frequency of the 1S-2S frequency has been determined in analog manner as described above. Line spectra for different atom velocities are shown in Fig.6.5. Due to the lack of a comprehensive line shape model the experimental data are fitted by a Lorentzian which represents a good approximation. For high velocities the second order Doppler effect causes an asymmetry which is why they are not evaluated. A small residual asymmetry for the slower atoms is determined and taken into account by comparing with a Monte-Carlo simulation [111].

The value :

$$\nu_{1S-2S}^{Nov} = 2\,466\,061\,413\,187\,017\,(11)\text{ Hz}$$

is in good agreement with the May value (see Fig.6.6).

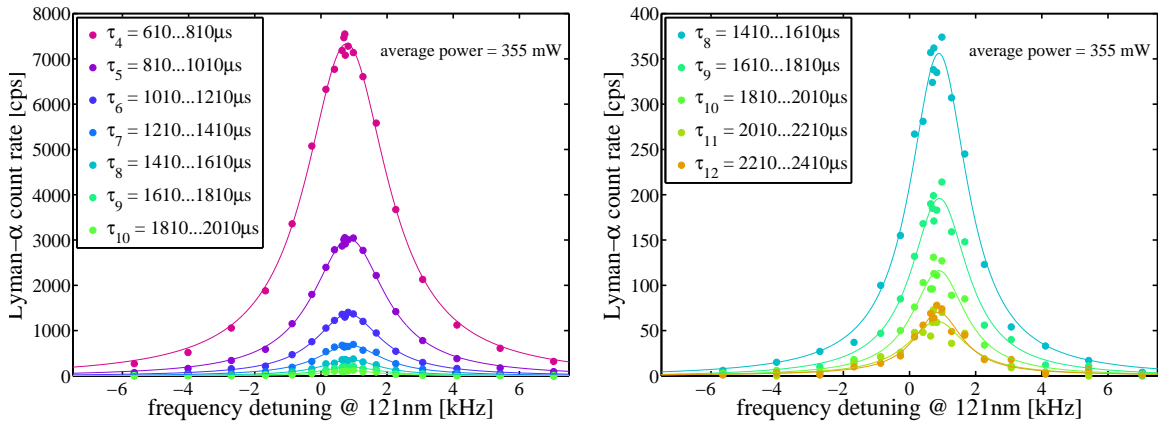


Figure 6.5: 1S-2S atomic line spectra for different velocities together with a Lorentzian fit. Here, velocities are measured as delays τ from excitation to detection. The right plot shows the same data as the left one but with enlarged vertical axis [111]. With kind permission of C. Parthey.

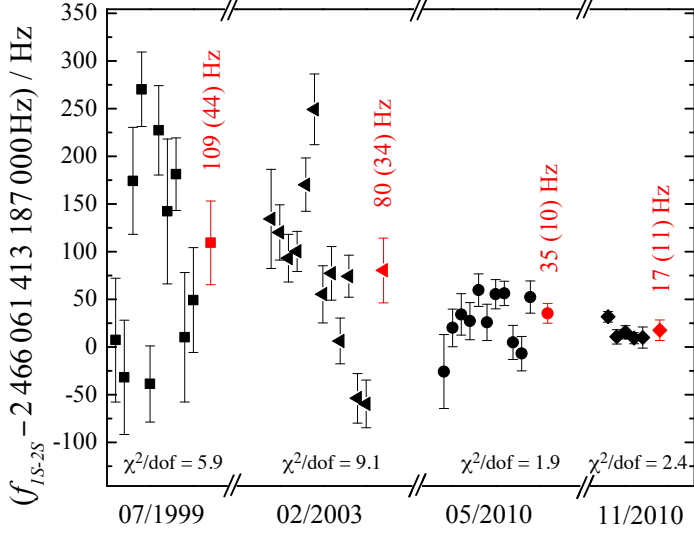


Figure 6.6: Absolute frequency measurements of the 1S - 2S transition in atomic hydrogen in 1999, 2003, and 2010. Red dots represent the mean over the respective measurement campaign [4].

6.3 Testing Electron Boost Invariance with 1S-2S Hydrogen Spectroscopy

The unification of general relativity and the Standard Model remains one of the major unsolved problems in theoretical physics. It is assumed that both theories merge within the frame of a superior quantum gravity theory which will supposedly become dominant at energy levels at the Planck scale of $\sim 10^{19}$ GeV. Direct experimental verification of promising theory candidates such as string theory or quantum loop gravity is thus hard to realize. However, it has been shown that both, string theory and quantum loop gravity can lead to a violation of Lorentz symmetry which is not included in the Standard Model [121, 122]. The strategy of the Standard Model Extension (SME) is therefore to identify all parameters that would measurably affect a particle's fundamental properties by Lorentz invariance violation. This also includes violation of the charge conjugation, parity, and time reversal (CPT) symmetry.

The above mentioned advantages of 1S-2S spectroscopy on atomic hydrogen (simple system, high spectral purity) make it also an attractive candidate for measuring Lorentz symmetry violation. Especially the electron boost symmetry violation parameter $c^{\nu\mu}$ can be probed by measuring the frequency difference of the 1S-2S transition at different times of the year [123].

The difference of the May and November measurements together with the average Earth velocity difference in May and November hence yields a bound for one linear combination of the $c_{(TJ)}$ coefficient [8]

$$0.95c_{(TX)} - 0.29c_{(TY)} - 0.08c_{(TZ)} = (2.2 \pm 1.8) \times 10^{-11} \quad (6.2)$$

which is a 4 fold improvement compared to previous measurements. Other linear combinations of the $c_{(TJ)}$ coefficient could be constrained by repeating this measurement again [123].

6.4 Discussion

Above derived fractional frequency instability of the fiber link of $3.8 \times 10^{-14} \text{ s}\tau^{-1}$ exceeds the requirements of the rf-clock comparison by at least one order of magnitude for all integration times longer than 1 second. Therefore, it allows for a direct comparison between the MPQ H-maser and PTB's CSF1. As the link as well as the two rf-clocks are operated more or less on a continuous basis CSF1 can be provided for high precision experiments at MPQ as a permanent service.

Frequency measurements such as the one described in this chapter, put lower demands on the performance of the link than the phase-coherent measurements discussed in Chapter 5. Here, cycles may be lost during transmission. As long as detected, they will only affect the statistical uncertainty and not systematically shift the transmitted frequency.

Next generation hydrogen experiments are expected to possess an accuracy improved by up to one order of magnitude. This will surpass Cs-fountain clocks as suited references making the usage of optical references compulsory. By then, the fiber link connecting the MPQ hydrogen experiment to a standards institute such as PTB will even more become a mandatory prerequisite for providing a remote optical reference for hydrogen spectroscopy. Future link applications might hence employ PTB's Sr or Yb⁺ standards [124, 16] that allow for even higher accuracies.

Chapter 7

Conclusion & Outlook

The work presented here encompasses the implementation, characterization and application of a 920 km long optical fiber link for phase-coherent transmission of a stable reference oscillator. It proved that fiber links are perfectly suited for comparing even the most accurate optical clocks available [2].

The fiber link was successfully utilized to provide a 600 km distant precise microwave reference for high precision spectroscopy on atomic hydrogen. Due to the simple level structure, spectroscopy on atomic hydrogen is one of the most important experiments to test QED and accurate referencing is a crucial prerequisite to fully explore its capabilities. Both rf-clocks - a cesium fountain clock and a hydrogen maser - were compared in real time as the link stability supersedes the clock stability by at least one order of magnitude on all time scales longer than one second. By performing this experiment exactly half a year later than a previous hydrogen measurement, new limits on the electron boost Lorentz invariance violation could be set.

The negotiations for an extension of the link to Paris have already started. This would enable cross-border optical clock comparisons between the Physikalisch-Technische Bundesanstalt (PTB) and the French institute for Systèmes de Référence Temps-Espace (LNE-SYRTE) over even larger distances (~ 1500 km). Several research facilities along the link have already announced their interest to get connected. Hence, the foundation for a continental scale research fiber network has been laid.

Dark channels will be more likely employed than the dark fibers used in this experiment as they are more easily available. New technical challenges will arise due to cross talk and severe restrictions for input power and transmitted frequency. However, French researchers have already demonstrated that this will be a solvable issue [144].

Future generations of fiber links will implement technical improvements of the ampli-

fication and stabilization scheme, which may include some of the following aspects. Brillouin amplifiers show a larger gain and a significantly narrower ASE band compared to bi-directional EDFAs but require a reliable non-laboratory locking scheme. Raman amplifiers that show a broader gain spectrum could be an alternative and will be tested at MPQ in the near future.

The fiber noise cancellation for the long links is strongly limited by the runtime of the light of ~ 10 ms. In this experiment, this was not an obstacle because the link itself was rather undisturbed. A more noisy system might require concatenated stabilization stages that do not necessarily have to have equidistant lengths. Combining short and fast locking stabilization stretches (passing urban agglomerations, for example) with longer quiet distances that mainly compensate for slow temperature drifts could further increase the stability of the transmission.

In the near future, a large number of long-haul synchronization applications will strongly benefit from optical fiber links. Examples, aside from time and frequency metrology, are next-generation linear colliders [145] and large astronomical antenna arrays such as the Atacama Large Millimeter Array [146], both demanding low-noise frequency dissemination systems with minimal phase drifts and errors. The stable synchronization afforded by the transmission of an optical carrier frequency will also foster new developments in very long baseline interferometry (VLBI) astronomy such as large-aperture VLBI in the near-infrared and optical wavelength range. Here, the combination of high frequencies and long interferometric base lines requires the distribution of a local oscillator with low phase noise and low phase drift through the array [147]. For the Deep Space Network of NASA, a system of optical fiber links has been developed to distribute reference signals from a hydrogen maser for antenna synchronization [148].

The implementation of a European fiber network for highly stable optical frequency transmission would boost the field of time and frequency metrology. In particular, the network would enable stability tests of satellite-based time transfer techniques and of the timing facilities of the global navigation satellite systems GPS, Glonass, and Galileo [149].

Several fundamental physics research programs would benefit from the ability to compare distant optical frequency standards through optical fiber links without any significant loss in accuracy or stability. Prominent examples are tests on possible violations of the equivalence principle of general relativity and the possible drift of the fine structure constant [149]. Clearly, the ability to perform comparisons between distant optical clocks at the highest possible accuracy level is also a prerequisite for a possible redefinition of the SI second on the basis of an optical clock.

Appendix A

Signal Statistics

The characterization of stable oscillators such as the atomic clocks and stable lasers described in this work is equivalent with the analysis of phase and frequency noise. Hence, the following sections provide both, the mechanisms that lead to phase and frequency fluctuations in a periodic signal as well as the mathematical background to describe them. Let therefore

$$V(t) = A(t) \cdot \sin(2\pi\nu_0 t + \varphi(t)) \quad (\text{A.1})$$

be the signal of a stable oscillator with time-dependent amplitude $A(t)$, nominal frequency ν_0 , and phase excursions $\varphi(t)$. Fig.A.1 illustrates how a modulation of A or φ with a constant modulation period changes the characteristics of the sinusoid.

In the frequency domain the spectral features of the oscillator are given by the signal's Fourier transform:

$$\tilde{V}(f) = \int_{-\infty}^{\infty} V(t) \cdot e^{-i2\pi ft} dt \quad (\text{A.2})$$

Modulations as described above will result in the spectra shown in Fig.A.2: Amplitude modulation will cause single sidebands at the modulation frequency f_{AM} around the carrier frequency.

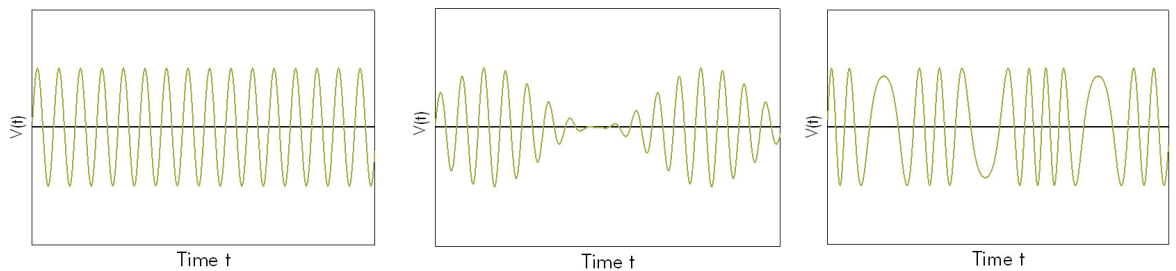


Figure A.1: *Temporal behavior of a sinusoid that is a) amplitude modulated or b) phase modulated*

Harmonic phase modulation results in a more complex spectrum with an infinite number of sidebands at frequencies $n \cdot f_{PM}$ and peak amplitudes described by Bessel functions. However, for small modulation depths most of the power is found to be in the carrier and in the first order sidebands. Hence, the instantaneous frequency is given by:

$$\nu(t) = \nu_0 + \frac{d\varphi(t)}{2\pi dt} \quad (\text{A.3})$$

For better comparability between different systems it is common use to state *fractional* phase $x(t)$ and frequency deviations $y(t)$:

$$x(t) = \frac{\varphi(t)}{2\pi\nu_0} \quad (\text{A.4})$$

and

$$y(t) = \frac{1}{2\pi\nu_0} \frac{d\varphi}{dt} \quad (\text{A.5})$$

A.1 Signal Statistics in the Time Domain

Consider a time series of frequency values y_i measured with a frequency counter as described in Appendix 2.1.3. For a purely stochastic process and a sufficient large number N of measured samples, the oscillator is well characterized by the mean

$$\bar{y} = \frac{1}{N} \sum_{i=1}^N y_i \quad (\text{A.6})$$

variance and standard deviation

$$\sigma_{StVar} = \sigma_{StDev}^2 = \frac{1}{N-1} \sum_{i=1}^N (y_i - \bar{y})^2 \quad (\text{A.7})$$

and the standard deviation of the mean

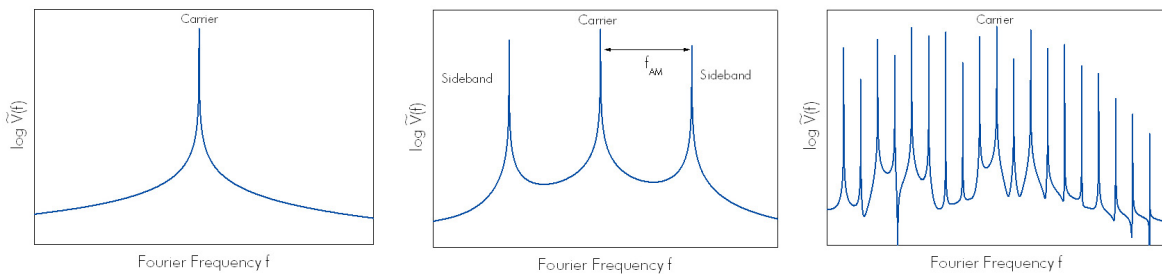


Figure A.2: Sideband generation by a) amplitude modulation or b) phase modulation of a sinusoidal function.

$$u = \frac{\sigma_{StDev}}{\sqrt{N}} \quad (\text{A.8})$$

However, for certain correlated noise types, such as frequency drifts Eqns. A.6- A.8 diverge. Therefore, two-sample variances such as the Allan deviation and the modified Allan deviation have been suggested to characterize frequency fluctuations [18, 20]:

$$\sigma_y(\tau) = \sqrt{\frac{1}{2} \langle (\bar{y}_1(t) - \bar{y}_2(t))^2 \rangle} \quad (\text{A.9})$$

$$\sigma_{mod}(\tau)^2 = \frac{1}{2} \left\langle \left[\frac{1}{N} \sum_{i=1}^N \left(\frac{1}{N} \sum_{k=1}^N \bar{y}_{i+k+N, \tau_0} - \frac{1}{N} \sum_{k=1}^N \bar{y}_{i+k, \tau_0} \right) \right]^2 \right\rangle \quad (\text{A.10})$$

with \bar{y}_i being the measurement samples averaged over increasing integration times τ and τ_0 being the frequency counter gate time. The modified ADEV is preferable to use if a high sensitivity to white phase noise is required.

A.2 Noise Sources

Most random frequency fluctuations can be described as a linear combination of five independent processes that affect the oscillator's stability (modified Allan variance) obeying a power law:

$$\sigma_{mod}^2(\tau) \propto h_\alpha \tau^\alpha \quad (\text{A.11})$$

with $\alpha = -3, -2, \dots, 1$. These noise types often have characteristic origins and the corresponding instability curve can help identify excess noise in the system.

A.2.1 White Phase Noise (h_{-3})

White phase noise is broadband noise and normally distributed. Out of all noise types it has the strongest dependence on the averaging time τ and hence most quickly reveals possible systematic effects. For white phase noise and corresponding measurement times, the Allan deviation differs from the standard deviation only by the constant factor $\sqrt{2/3}$ [125]. A properly phase-locked system is, for example, subject to white phase noise.

A.2.2 Flicker Phase Noise (h_{-2})

Flicker noise is literally ubiquitous: it can be found in every electronic device but also in biological systems, in economics, in language and music and even in psychology [126, 127, 128, 129]. No mathematical formalism has been developed so far to describe flicker noise thoroughly. It is found in electronic systems and in particular in active resonators and amplifiers.

A.2.3 White Frequency Noise (h_{-1})

White frequency noise often represents a fundamental feature in frequency standards. Quantum projection noise is for example a white frequency noise source. A shot noise limited light source can turn into one where intensity fluctuations turn into frequency fluctuations.

A.2.4 Flicker Frequency Noise (h_0)

Every oscillator exhibits a flicker 'floor' at which the stability is independent from the averaging time τ . This may be due to thermal or power supply voltage fluctuations, magnetic field fluctuations, or changes in microwave power [130].

A.2.5 Random Walk of Frequency (h_1)

Environmental parameters such as temperature fluctuations and mechanic vibrations cause a random walk of frequency [17]. Proper isolation or active stabilization can mitigate this effect.

A.3 Signal Statistics in the Frequency Domain

In the Fourier domain, phase (or frequency) fluctuations are characterized by means of the power spectral density

$$S_\varphi(f) = |\tilde{\varphi}(f)|^2 \quad (\text{A.12})$$

and

$$S_y(f) = \frac{f^2}{\nu_0^2} S_\varphi(f) \quad (\text{A.13})$$

applying:

$$y(t) = d\varphi/dt \xleftrightarrow{FT} \tilde{y}(f) = f\tilde{\varphi}(f).$$

According to the Wiener-Khintchine-theorem, $S_\varphi(f)$ is related to the signal's autocorrelation function $R_\varphi(\tau) = \langle \varphi(t) - \varphi(t - \tau) \rangle$ for stationary distributed phase fluctuations:

$$S_\varphi(f)^{2\text{-sided}} = \int_{-\infty}^{\infty} R_\varphi(\tau) e^{i2\pi f\tau} d\tau \quad (\text{A.14})$$

Since $R_\varphi(\tau)$ is an even function the spectrum of $S_\varphi(f)$ contains no additional information for Fourier frequencies $-\infty < f < 0$. Therefore, it is often expressed as $S_\varphi(f)^{1\text{-sided}} = 2S_\varphi(f)^{2\text{-sided}}$. Throughout this work, $S_\varphi(f)$ is considered to be $S_\varphi(f)^{1\text{-sided}}$ unless denoted otherwise. From that, the rms-value of the phase fluctuations is given by:

$$\langle \varphi(t)^2 \rangle = \int_0^\infty S_\varphi(f) df \quad (\text{A.15})$$

A.4 Conversion from Time Domain to Frequency Domain

As mentioned in Chapter 2, the Allan deviation can be written as:

$$\sigma_y(\tau) = \sqrt{\left\langle \left(\int_{-\infty}^{\infty} y(t') h(t-t') dt' \right)^2 \right\rangle} \quad (\text{A.16})$$

with a rectangular filter function $h(t)$:

$$h(t) = \begin{cases} -\frac{1}{\sqrt{2\tau}} & \text{for } -\tau < t < 0 \\ \frac{1}{\sqrt{2\tau}} & \text{for } 0 \leq t < -\tau \\ 0 & \text{otherwise} \end{cases} \quad (\text{A.17})$$

Eq.A.16 is the convolution of the two functions $y(t)$ and $h(t)$. For uncorrelated fluctuations $y(t)$ it can be re-written to hold

$$\sigma_y(\tau) = \sqrt{\left\langle \left(\int_{-\infty}^{\infty} y(t')^2 h(t-t')^2 dt' \right) \right\rangle} \quad (\text{A.18})$$

as any term $y(t'_i) \cdot y(t'_j)$ averages to zero for $i \neq j$.

According to the convolution theorem, in the frequency domain this corresponds to a multiplication of the Fourier transforms $\mathcal{F}\{y(t)^2\}$ and $\mathcal{F}\{h(t)^2\}$. The Allan variance hence relates to the phase spectral density $S_y(f)$ as:

$$\sigma_y(\tau)^2 = \int_{-\infty}^{\infty} S_y(f) |H_\tau(f)|^2 df \quad (\text{A.19})$$

For white phase noise, $|H_\tau(f)|^2 = \frac{\sin^4(\pi\tau f)}{(\pi\tau f)^2}$ (see e.g. [17] pp. 61).

Similar to the τ -dependence of the Allan variance the frequency -dependence of $S_y(f)$ uniquely corresponds to a certain noise type.

Appendix B

Optical Frequency Measurements

As frequency can be measured more precisely than any other physical unit it is desirable to relate a measured quantity to a frequency. However optical signals with frequencies of several hundreds of THz are not accessible directly by using electronic devices. The following section describes how optical frequency measurements can be performed anyway by down-converting the signal to the microwave regime.

B.1 Optical Heterodyne Beat Detection

To make an optical frequency ν_1 detectable for electronic devices it can be mixed down using a second well known optical frequency ν_2 nearby. The resulting beat note yields information about frequency, line width, and power levels. This method constitutes the basic principle of the frequency comb technique described at the end of this section.

B.1.1 Optical Beat Notes

The principle of generating a beat note between two optical frequencies is shown in Fig.B.1.

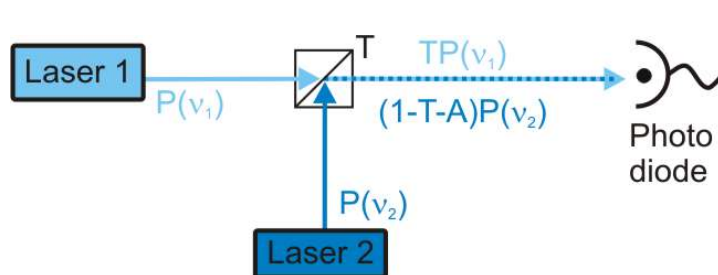


Figure B.1: *Principle of the heterodyne beat detection: Signals with powers $P(\nu_1)$ and $P(\nu_2)$ are overlapped using a beam splitter with transmission T and attenuation A . The resulting beat intensity is detected with an AC coupled photo diode.*

Overlapping two single-frequency electric fields $\mathbf{E}(\nu_1) = \mathbf{E}_1 \cos(2\pi\nu_1 t + \varphi_1(t))$ and $\mathbf{E}(\nu_2) = \mathbf{E}_2 \cos(2\pi\nu_2 t + \varphi_2(t))$ results in a linear superposition $\mathbf{E} = \mathbf{E}(2\pi\nu_1) + \mathbf{E}(2\pi\nu_2)$. The corresponding optical power on a photo detector surface is given by:

$$\begin{aligned} P_{opt} &\propto |\mathbf{E}(2\pi\nu_1) + \mathbf{E}(2\pi\nu_2)|^2 \\ &= \mathbf{E}_1^2 + \mathbf{E}_2^2 + 2\mathbf{E}_1\mathbf{E}_2 \cos(2\pi(\nu_1 - \nu_2)t + \Delta\varphi(t)) \end{aligned}$$

taking into account that the photo diode is not able to detect the fast oscillations at 2ν and $\nu_1 + \nu_2$. By ac-coupling the beat signal of interest can be extracted:

$$P_{beat} \propto \mathbf{E}_1\mathbf{E}_2 \cos(2\pi(\nu_1 - \nu_2)t + \Delta\varphi(t)) \quad (\text{B.1})$$

The corresponding photon flux $\Phi(t)$ has an average power $P_{beat} = N_{photons} \cdot h\nu$ where $N_{photons}$ is the number of photons per second and $h\nu$ is the photon energy. It is converted into an electrical current according to the quantum efficiency η of the photo diode:

$$I_{el} = N_{el} \cdot q = \frac{\eta q}{h\nu} \cdot P_{beat} \quad (\text{B.2})$$

with $q = 1.6 \dots 10^{-19} \text{C}$ being the elementary charge.

Hence, the photo diode can be considered as a frequency mixer with a nonlinear response to the individual input amplitudes \mathbf{E}_1 and \mathbf{E}_2 . The mean electrical power across a load R is given by the intensities of the individual light fields:

$$\langle P_{el} \rangle = \left(\frac{\eta q}{h\nu}\right)^2 \cdot \langle P_{beat}^2 \rangle \cdot R \propto \langle P_1 \rangle \langle P_2 \rangle \quad (\text{B.3})$$

B.1.2 Signal-to-Noise Ratio

The SNR of the beat signal given by [131]:

$$SNR = \frac{P_{signal}}{\sum P_{noise}} = \frac{\langle P_{el} \rangle}{\sum \int_{BW} P_{noise}(\nu) d\nu} \quad (\text{B.4})$$

where all stochastic independent noise processes are summarized after having been integrated over the detection bandwidth BW . For purely shot noise limited signals Eq.B.4 reads:

$$SNR = \frac{\langle P_{el} \rangle}{2q(I_{el1} + I_{el2})BW} \propto \frac{P_{opt1}P_{opt2}}{P_{opt1} + P_{opt2}} \quad (\text{B.5})$$

Eq.B.5 considers the power that impinges on the detector surface which in turn illustrates that the choice of the beam splitter will influence the SNR for given P_1 and P_2 . To optimize the SNR, Eq.B.5 is re-written to account for a beam splitter with transmission T , reflection $R=1-T$ -A with the inherent loss A :

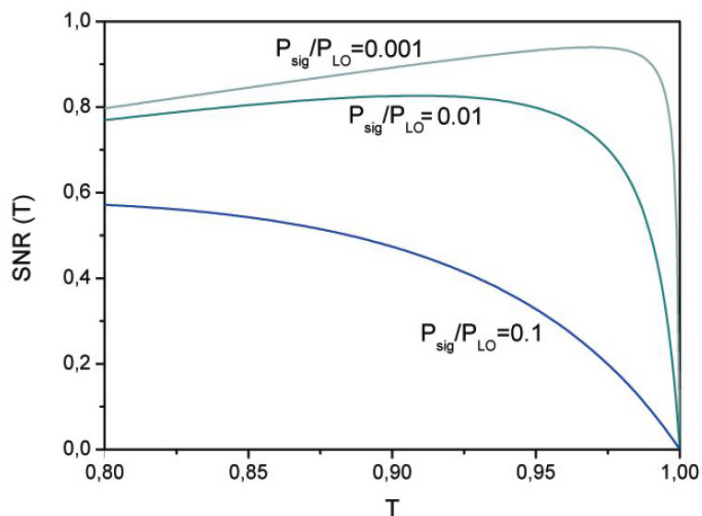


Figure B.2: *Signal-to-Noise ratio for beat notes with varying input powers and for different transmission of the beam splitter.*

$$SNR = \frac{TP_1(1 - T - A)P_2}{2qBW(TP_1 + (1 - T - A)P_2)} \quad (B.6)$$

The SNR is maximized for:

$$T = 1 - A\sqrt{\frac{P_2}{P_1 + P_2}} \quad (B.7)$$

B.1.3 Measuring Weak Signals with a Strong Local Oscillator

Comparison of a weak signal to a strong local oscillator (LO) using the heterodyne technique rather than measuring it directly will result in improved detection efficiency. The reason for that is the square-law behavior of the photo detector described above that causes a current which is amplified by $\sqrt{I_{LO}/I_{SIG}}$ compared to direct detection. Choosing the LO intensity strong can therefore significantly improve the sensitivity. In the regime of shot noise the SNR is determined by the power of the weak signal:

$$SNR \propto P_{sig} \quad (B.8)$$

For given LO power P_{LO} it is maximized using a beam splitter with high transmission according to:

$$T = 1 - A\sqrt{\frac{P_{SIG}}{P_{LO}}} \quad (B.9)$$

which close to 1 is for small fractions of P_{SIG}/P_{LO} (see Fig.B.2).

The heterodyne beat detection technique thus combines amplification of a weak optical signal with phase-coherent down-conversion to the radio frequency domain.

B.1.4 Self-Heterodyne Beat Detection

Another important heterodyne technique is the comparison of a signal with frequency ν_0 to a time-delayed copy of itself. This is for example employed in the interferometric fiber noise cancellation scheme described in Appendix E. The ratio of the arm lengths and the coherence time τ_c of the laser determine the degree of correlation of the two superimposed signals and hence the line width of the resulting beat note as shown below.

A frequency shifter such as an acousto-optic-modulator (AOM) is usually placed in one arm in order to generate the beat note at a convenient radio-frequency. When superimposing both beams the light having passed the long arm is delayed by τ . The detected beat note has a frequency centered on the AOM frequency and its width depends on the ratio of coherence length to the delay τ_c/τ as well as to fiber phase noise arising in the long arm. According to Eq.B.2 the photo current generated in the detector is:

$$I_{el} = \frac{q\eta}{2h\nu_0} P_0 \cos(-2\pi(f_{AOM})t + 2\pi(\nu_0 + f_{AOM})\tau + \varphi(t) + \varphi(t - \tau)) \quad (\text{B.10})$$

From that the autocorrelation function $R_I(\delta\tau, \tau)$ can be determined to be [132]:

$$R_I(\delta\tau, \tau) = \left\langle \frac{1}{2} P^2 e^{-|\tau|/\tau_c} \cos(2\pi f_{AOM} \delta\tau e^{-1/\tau_c(\delta\tau - |\tau|)}) \right\rangle \quad (\text{B.11})$$

Making again use of the Wiener-Kintchine theorem (see above) yields the power spectral density

$$S(\nu, \tau) = \frac{1/2P^2\tau_c}{1 + (2\pi\nu + f_{AOM})^2\tau_c^2} \cdot \left\{ 1 - e^{-|\tau|/\tau_c} \cdot \left[\cos(2\pi\nu \pm f_{AOM}) |\tau| \frac{\sin(2\pi\nu \pm f_{AOM}) |\tau|}{(2\pi\nu \pm f_{AOM})\tau_c} \right] \right\} + \frac{1}{2} P^2 \pi e^{-|\tau|/\tau_c} \cdot \delta(2\pi\nu \pm f_{AOM}) \quad (\text{B.12})$$

Two limits can be considered: if one arm is long compared to the coherence length of the laser the ratio $|\tau|/\tau_c$ approaches ∞ and the resulting beat note is fully uncorrelated. $S(\nu, \tau)$ then simplifies to:

$$S(\nu, \tau) \approx \frac{1/2P^2\tau_c}{1 + (2\pi\nu + f_{AOM})^2\tau_c^2} \quad (\text{B.13})$$

This is a Lorentzian with a FWHM of $1/\tau_c$ which represents the line width of the laser.

Considering the other limit when the coherence length of the laser is long compared to the interferometer arm $S(f, \tau)$ is given by:

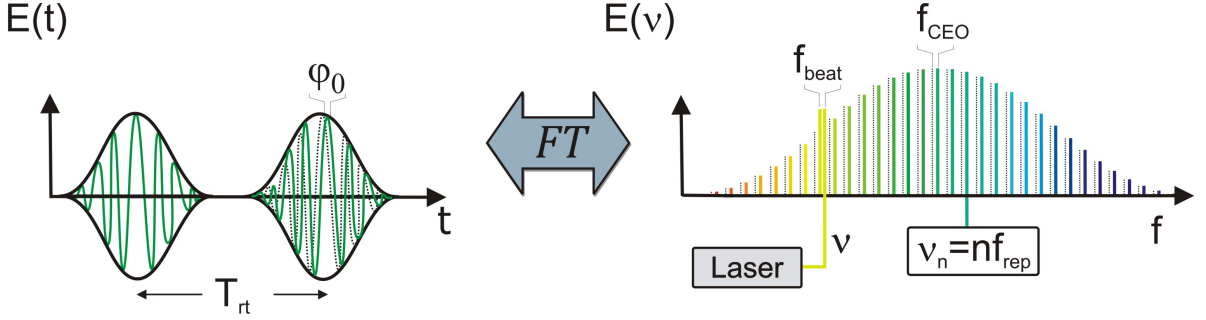


Figure B.3: A phase-coherent pulse train generates a comb-like pattern in frequency domain. Any unknown frequency within the comb-spectrum can thus be calculated according to Eq.B.15. Frequency combs had an unexpected impact on fundamental research, telecommunication and satellite navigation and were awarded the Nobel Prize in 2005 [134].

$$S(\nu, \tau) \approx \frac{1}{2} P^2 \pi \cdot \delta(2\pi\nu \pm f_{AOM}) \quad (\text{B.14})$$

In this limit $S(\nu, \tau)$ is dominated by fiber phase noise.

Two applications come to mind: using a low noise fiber long enough to de-correlate the signal can be used to determine the line width of the laser (according to [132], the required length is about six times the coherence length). Considering narrow line width lasers of a few kHz with coherence lengths of several tens of kilometers it is most applicable to use temperature-stabilized and acoustic shielded fiber spools. In this configuration, the heterodyne beat signal can even be used to stabilize the laser. This was recently demonstrated by [105]. In the fiber link experiment, laser noise is suppressed and Eq.B.14 is purely dominated by fiber phase noise. Hence, the resulting beat note can be used for active stabilization of the fiber path.

B.2 Femtosecond Frequency Combs

A femtosecond frequency comb is provided by a mode-locked laser which emits a pulse train with the very characteristic feature of two subsequent pulses having a fixed phase relationship. In the frequency domain, this pulse train generates a comb-like structure of n frequency modes with amplitudes A_n that are equally spaced by the inverse pulse round-trip time $f_{rep} = T_{rt}^{-1}$. They are further shifted from zero by a certain carrier offset frequency f_{ceo} which results from different phase and group velocities of the pulses inside the resonator. This causes a constant phase shift after one round-trip $\Delta\varphi = 2\pi f_{ceo} T_{rt}$ (see Fig(B.3)).

Any unknown optical frequency ν within the spectral range of this frequency comb can be deduced from three radio frequencies by measuring the beat note to the closest comb

mode $\nu_n = f_{ceo} + n \cdot f_{rep}$ [44]:

$$\nu = f_{ceo} + n \cdot f_{rep} + f_{beat} \quad (\text{B.15})$$

The remarkable feature of this equation is that the optical comb mode ν_n can be expressed by two radio frequencies f_{rep} and f_{ceo} thus determining any optical frequency via the beat note f_{beat} . The repetition frequency f_{rep} is measured in a straightforward manner using a fast photo-diode and appropriate filtering.

The determination of the carrier envelope offset cannot be performed by direct detection such as f_{rep} since it is a 'true' radio frequency offset. Rather, it is usually determined employing a nonlinear interferometer in which one mode out of the 'red' part of the comb spectrum is frequency doubled and measured against its second harmonic. Spectral broadening to reach an octave spanning spectrum is obtained by self-phase modulation using special nonlinear fibers [135]. The resulting beat note equals the offset frequency:

$$f_{beat} = 2(f_m + f_{ceo}) - (f_{2m} + f_{ceo}) = f_{2m} + 2 \cdot f_{ceo} - f_{2m} - f_{ceo} = f_{ceo} \quad (\text{B.16})$$

Having set up this beat note the offset frequency is directly accessible and the comb spectrum is nearly fully determined. The only parameter missing is the mode number n .

If ν can be measured with a wave-meter with a resolution better than half the mode spacing, the actual determination is straightforward. However, the mode spacing typically lies in the range of ~ 100 MHz which requires a wave-meter with very high accuracy. If no such a spectrometer is at hand it can also be obtained by measuring f_{beat} with two different repetition rates f_{rep_1} and $f_{rep_2} = f_{rep_1} + \Delta f_{rep}$ as in detail described in [136]. The mode number is then given by:

$$n = \frac{\Delta f_{beat} + f_{rep_1} + \Delta f_{rep}}{\Delta f_{rep}} \quad (\text{B.17})$$

It should be noted that the radio frequencies f_{rep} and f_{ceo} are not inherently stable enough to produce the periodicity in the pulse train that is necessary to generate the comb pattern. Hence, both need to be stabilized to a superior frequency reference. Here, the stability of f_{ceo} is not as crucial - it just shifts the whole comb along the frequency axis. However, the stability of f_{rep} scales with n ($\sim 10^6$) and strongly influences the quality of the comb mode. From that it becomes clear that the locking scheme has to be designed carefully like for example discussed in [137].

On the other hand, this large scaling between optical and microwave region can be used in a determined manner by stabilizing the comb modes directly to an optical reference cavity. The spacing between the modes can reversely be down-converted using a fast photo-diode to generate a very stable microwave signal [138].

Appendix C

Basics of Phase-locked Loops

The basic principle of any phase-locked loop (PLL) is shown in Fig.C.1. The oscillator to be stabilized has a tuning input that can be controlled by applying a voltage. This is commonly referred to as voltage controlled oscillator (VCO). The VCO frequency is compared to a stable reference by feeding both into a phase detector. The phase detector (e.g. a frequency mixer) returns a voltage V_{PD} that depends on the phase-difference $\varphi_{in} - \varphi_{out}$:

$$V_{PD} = K_{PD} \cdot (\varphi_{in} - \varphi_{out}) \quad (\text{C.1})$$

with the device-dependent gain factor K_{PD} . The loop filter transforms this error signal into a control signal that suppresses noise and high frequency components. The VCO is steered by the control voltage V_C :

$$V_C = h(t) \cdot V_{PD} \quad (\text{C.2})$$

with a transfer function $h(t)$. In the Laplace domain it is transformed into the loop filter response function $H(s)$: $h(t) \xrightarrow{\mathcal{L}} H(s)$ with the complex variable $s = j\omega$

$$H(s) = \int_{-\infty}^{\infty} h(t)e^{-st} dt \quad (\text{C.3})$$

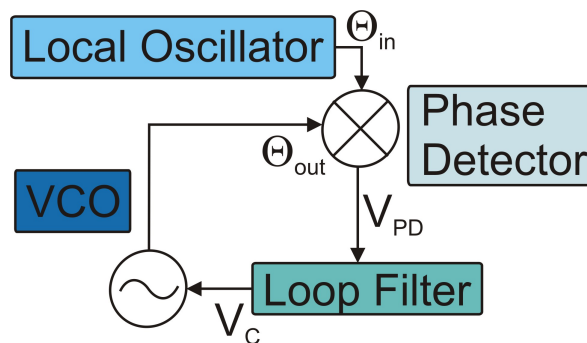


Figure C.1: *Basic scheme of a phase locked loop: The instantaneous frequency of a voltage controlled oscillator (VCO) is compared to a stable reference, the local oscillator (LO).*

For Laplace transform pairs (as for Fourier transform pairs) the following useful relations hold true:

$$\frac{d^n h(t)}{dt} \xleftrightarrow{\mathcal{L}} s^n H(s) \quad (\text{C.4})$$

$$g(t) = \int_{-\infty}^t h(\tau) d\tau \xleftrightarrow{\mathcal{L}} \frac{H(s)}{s} \quad (\text{C.5})$$

$$g(t - \tau) \xleftrightarrow{\mathcal{L}} g(s)e^{-s\tau} \quad (\text{C.6})$$

Using C.1 - C.6 yields the characteristic loop parameters:

$$\tilde{V}_{PD}(s) = K_{PD}[\tilde{\varphi}_{in}(s) - \tilde{\varphi}_{out}(s)] \quad (\text{C.7})$$

$$\tilde{V}_C(s) = F(s)\tilde{V}_{PD}(s) \quad (\text{C.8})$$

$$\tilde{\varphi}_{out}(s) = K_{VCO}\tilde{V}_c(s)/s \quad (\text{C.9})$$

with the loop filter function $F(s)$. The open loop gain $G(s)$ of the system is given by:

$$G(s) = \frac{K_{VCO}K_{PD}F(s)}{s} \quad (\text{C.10})$$

Whereas the transfer function for the closed loop $H(s)$ is:

$$H(s) = \frac{\varphi_{out}(s)}{\varphi_{in}(s)} = \frac{K_{VCO}K_D F(s)}{s + K_{VCO}K_D F(s)} = \frac{G(s)}{1 + G(s)} \quad (\text{C.11})$$

Phase noise is suppressed by [139]:

$$S_{out}(s) = |1 - H(s)|^2 S_{in}(s) = \left| \frac{1}{1 + G(s)} \right|^2 S_{in}(s) \quad (\text{C.12})$$

The loop filter $F(s)$ for a PLL of n-th order is given by the rational function

$$F(s) = \frac{g(s - z_1)(s - z_2) \cdots (s - z_n)}{(s - p_1)(s - p_2) \cdots (s - p_{n-1})} \quad (\text{C.13})$$

with zeros and poles that are determined by the design of the filter components which can be simple RC-elements in a low-pass filter design. For a first-order loop with a frequency independent proportional gain $F(s) = const$.

A very common type of PLL comprises a second order loop filter with active proportional-integral (PI) gain. The corresponding loop filter can be looked up for example in [139]:

$$F(s) = (s\tau_2 + 1)/s\tau_1 \quad (\text{C.14})$$

with $\tau_i = R_i C$. The filter design used in the fiber link experiment is described in Appendix E.

Appendix D

Laser Stabilization: Pound-Drever-Hall Technique

The Pound-Drever-Hall stabilization technique allows for stabilizing a turn-key laser system to line widths of 1 Hz or less by comparing the laser frequency to the free-spectral-range of a high-finesse Fabry-Perot resonator [140]. Lasers stabilized with this method are crucial components of many precision spectroscopy experiments, as well as in interferometric gravitational-wave detectors [141].

Comparing a laser frequency to a cavity mode can simply be accomplished by coupling some laser light into the cavity of length L_{cavity} and finesse \mathcal{F} and observing the reflected signal as depicted in Fig.(D.1): Whenever the laser frequency matches an integer multiple of the free spectral range $\Delta\nu_{FSR}$ all light couples into the cavity and the reflection has a sharp dip according to the Airy-function of the reflected intensity:

$$\frac{I_R}{I_0} = \frac{\mathcal{F} \sin^2(\varphi/2)}{1 + \mathcal{F} \sin^2(\varphi/2)} \quad (\text{D.1})$$

with $\varphi = m4\pi\nu/cL$; $m \in \mathbb{N}$.

Unfortunately, this signal cannot be used to lock the laser since the reflected intensity is symmetric about resonance: it contains no information about the direction in which the lock has to tune the laser in order to stabilize it to minimum reflection. The derivative, however, is anti-symmetric. Hence, periodically changing the frequency of the laser yields the desired information about the position of the laser with respect to the cavity.

In a Pound-Drever-Hall lock this is realized by phase-modulating the laser frequency ν and observing the reflected signal which now comprises the carrier and two modulation

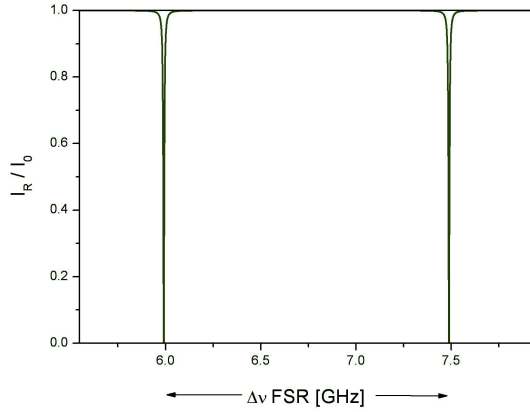


Figure D.1: *Reflectivity of a Fabry-Perot cavity as a function of the incident frequency.*

sidebands at frequencies $\nu - \Omega$ and $\nu + \Omega$. This is true, to first order, for small modulation depths. Mixing this signal to DC yields the characteristic error signal as shown in Fig.(D.2):

$$\epsilon = -2\sqrt{P_C P_S} \cdot \Im \{ F(\nu) F^*(\nu + \Omega) - F^*(\nu) F(\nu + \Omega) \} \quad (\text{D.2})$$

with the reflectivity coefficient $F(\nu) = E_R(\nu)/E_0(\nu)$ and the optical power of the carrier P_C and the sidebands P_S , respectively.

Near resonance the error signal depends linearly on the deviation between laser frequency and cavity resonance $\delta\nu$ [140]:

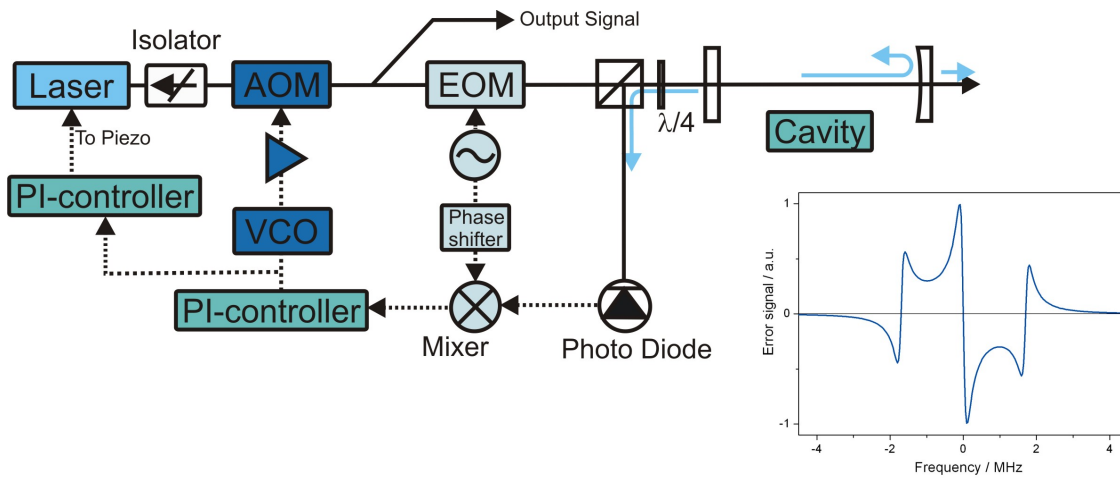


Figure D.2: *Pound-Drever-Hall Lock: An EOM is employed as a phase discriminator for the light reflected from the cavity.*

$$\epsilon \approx -2\sqrt{P_C P_S} \frac{\delta\nu}{\Delta\nu_{FSR}/\mathcal{F}} \quad (\text{D.3})$$

After passing an appropriate low-pass filter and servo amplifier it can be used to control the tuning port of the laser. In a real system two tuning ports are usually employed: fast fluctuations are compensated by an AOM and the laser piezo compensates for slow temperature drifts.

It should be noted that this locking technique is not sensitive to intensity fluctuations of the carrier, to the modulation depth or frequency or the response of the photo diode since the carrier vanishes on resonance. However, shot noise will also affect the sidebands and hence constitutes the fundamental limit for the PDH-locking technique.

Appendix E

Fiber Noise Cancellation: Phase-Locked-Loop with Delay

The Doppler noise cancellation scheme assures stable and accurate frequency transmission via the fiber link. This section discusses the implementation of an appropriate feedback loop for active fiber stabilization.

E.1 Delay Unsuppressed Fiber Noise

The scheme of the Doppler noise cancellation is shown in Fig.E.1: The signal accumulates phase noise $\varphi_{fiber}(z, t)$ while traveling the fiber link of length L which is given by [142]:

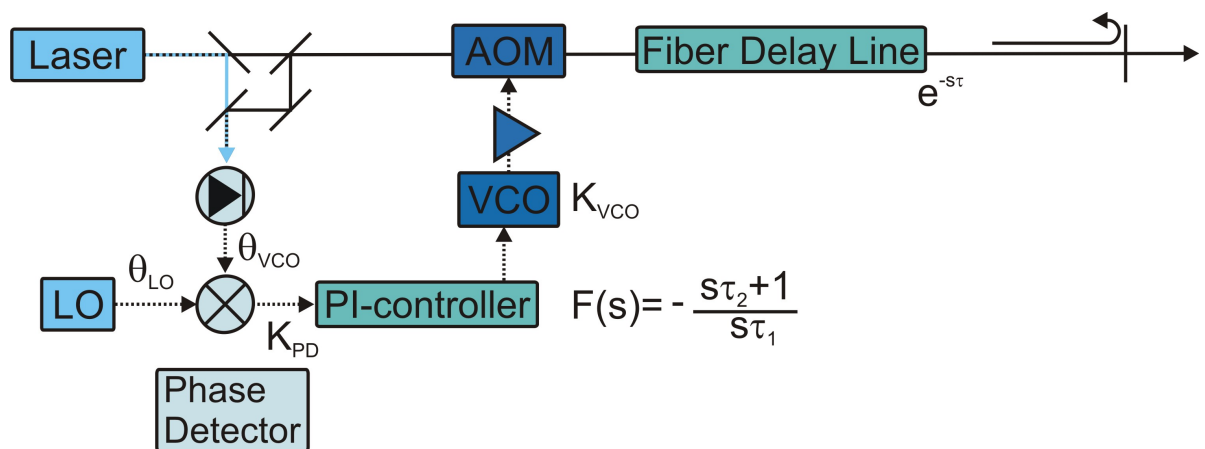


Figure E.1: Basic scheme of the fiber noise compensation scheme comprising a second order loop filter. See text for details.

$$\varphi_{fiber}(z, t) = \int_0^L \delta\varphi(z, t - (\tau - \frac{nz}{c})) dz \quad (\text{E.1})$$

For Doppler noise compensation, part of the light is reflected back within the same fiber and consequently has accumulated twice the phase noise after one round-trip:

$$\varphi_{fiber_{RT}}(z, t) = \int_0^L \left[\delta\varphi(z, t - (\tau - \frac{nz}{c})) + \delta\varphi(z, t - (2\tau - \frac{nz}{c})) \right] dz \quad (\text{E.2})$$

In the Fourier domain, the time delays simply transform into phase shifts

$$\tilde{\varphi}_{fiber}(\omega) = \int_0^L e^{-i\omega(2\tau - nz/c)} \delta\tilde{\varphi}(z, \omega) dz \quad (\text{E.3})$$

$$\tilde{\varphi}_{fiber_{RT}}(\omega) = \int_0^L [e^{-i\omega\tau} \cos(\omega(t - nz/c)) \tilde{\varphi}(z, \omega)] dz \quad (\text{E.4})$$

From that one derives the power spectral densities $S_{fiber}(\omega)$ and $S_{fiber_{RT}}(\omega)$ according to Eq.(A.15):

$$S_{fiber}(\omega) = \int_0^L \langle |\delta\varphi(z, (\omega))|^2 \rangle dz \quad (\text{E.5})$$

and

$$S_{fiber_{RT}}(\omega) = 2S_{fiber}(\omega)(1 + \text{sinc}(2nL/c\omega)) \quad (\text{E.6})$$

Note that, for low frequencies $\text{sinc}(0) \approx 1$ and the round-trip phase noise is four times larger than the one-way noise at the remote end.

The round-trip signal is compared to a local copy of itself that is assumed to have no delay and negligible phase noise. Therefore, the derived fiber phase fluctuations are converted into voltage fluctuations with a conversion gain factor K_{PD} (see Appendix

C). After being filtered with a certain loop filter function $F(s)$ (see below) they are converted into frequency fluctuations with conversion factor K/s . This signal steers a double-pass AOM at the fiber input in order to compensate for the one-way fiber phase noise. The corresponding open loop gain $G(s) = G(i\omega)$ hence becomes:

$$G(\omega) = K_{PD}F(\omega)\frac{K}{\omega}(1 + e^{-2i\omega\tau}) \quad (\text{E.7})$$

After closing the loop, the residual PSD after one round-trip $S_{inloop}(\omega)$ is according to Eq.(C.12) given by:

$$S_{inloop}(\omega) = \left| \frac{1}{1 + G(\omega)} \right|^2 S_{fiberRT}(\omega) \quad (\text{E.8})$$

As will be shown below, $G(\omega)$ and especially $F(\omega)$ have to be chosen carefully to assure stable loop operation. However, even for an optimized loop filter the one-way phase fluctuations are not perfectly canceled due to the large delay. This is denoted as *delay unsuppressed fiber noise*. The residual phase error $\tilde{\varphi}_{remote}(\omega)$ at the remote end is given by the subtracting the compensated one-way phase noise from the uncompensated one. Here, the compensated phase noise is given by $H(\omega)e^{-i\omega\tau}\tilde{\varphi}_{inloop}(\omega)$ [139] and hence [142]:

$$\tilde{\varphi}_{remote}(\omega) = \tilde{\varphi}_{fiber}(\omega) - H(\omega)e^{-i\omega\tau}\tilde{\varphi}_{inloop}(\omega) = \tilde{\varphi}_{fiber}(\omega) - \frac{G(\omega)}{1 + G(\omega)} \frac{1}{2\cos(\omega\tau)} \tilde{\varphi}_{fiberRT}(\omega) \quad (\text{E.9})$$

According to Eq.(A.12) and after some algebraic manipulation that can be reviewed in [142] one derives the corresponding power spectral density (PSD):

$$S_{remote}(f) = \frac{4\pi^2}{3} \left(f \frac{nL}{c} \right)^2 S_{fiber}(f) \quad (\text{E.10})$$

Eq.(E.10) only holds for stationary phase fluctuations and equal light propagation times $\tau_1 = \tau_2 = 1/2\tau_{rt}$. Further it is assumed that the loop filter suppresses phase noise with infinite gain within the loop bandwidth.

If the driving frequency coincides with a resonance, the oscillator will respond with a 180° phase shift and become instable. Noise will be enhanced rather than suppressed. This determines the loop bandwidth that can - other than the delay unsuppressed fiber noise - get increased by choosing an appropriate loop filter.

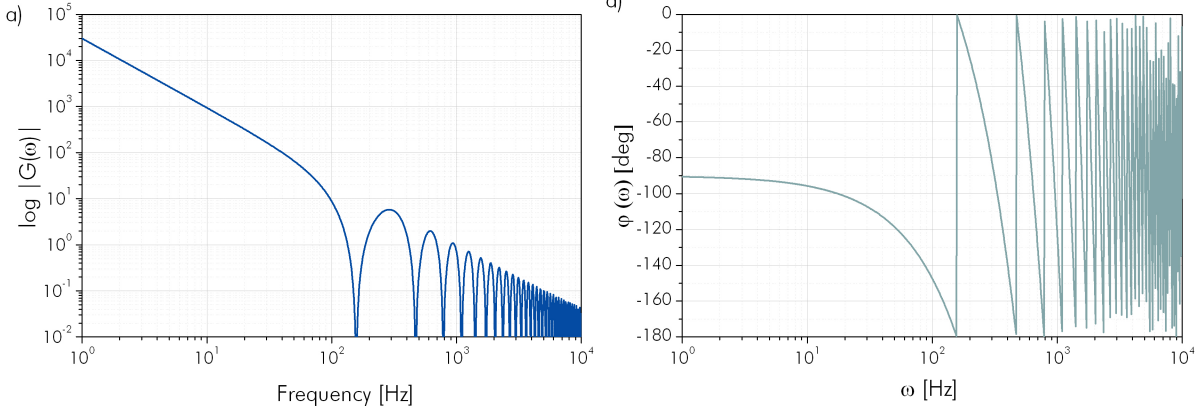


Figure E.2: Bode plots for a 920 km fiber interferometer (round-trip delay ~ 10 ms) comprising a second order loop filter as described in Appendix C and $R_1=R_2=1$ k Ω , $C=100$ nF, $K_{PD}=150$ kHz/rad. At multiple integers of $1/4\tau$ the gain amplitude is zero (a) and the phase diverges (shown here as $\text{mod}(\Pi)$).

E.2 Loop Filter Design

To identify the region of stable operation it is useful to display the open loop gain graphically separated in magnitude $A(G)$ and phase $\varphi(G)$ (Bode-plots):

$$A(\omega) = |G(s)| = \sqrt{\Re\{G(s)\}^2 + \Im\{G(s)\}^2} \quad (\text{E.11})$$

while the phase writes:

$$\varphi(\omega) = \arctan\left(\frac{\Re\{G(s)\}}{\Im\{G(s)\}}\right) \quad (\text{E.12})$$

For the link setup this turns into:

$$A(\omega) = \frac{2K_{PD}|F(s)|}{\omega} \cos^2(\omega\tau) \quad (\text{E.13})$$

and

$$\varphi(\omega) = -(\omega\tau + \pi/2) \quad (\text{E.14})$$

The Bode plots for a fiber link with round-trip time 10 ms and a second order loop filter $F(s) = \frac{1+i\omega R_2 C}{i\omega R_1 C}$ with $R_1 = R_2=1$ k Ω , $C=100$ nF, and $K_{PD}=150$ kHz/rad are shown in Fig.E.2a) and Fig.E.2b). For frequencies equal to integer multiples of $1/4\tau$ the gain amplitude becomes zero (unity gain) and the phase starts to diverge.

An optimized loop filter with alternating poles and zeros as e.g. suggested by [143] can be capable to increase the bandwidth over many interferometer nulls. Following

this approach, a loop filter particularly for the 920 km link was designed by [101]. It comprises 5 poles at 2 Hz, 50 Hz, 500 Hz, and 1.5 kHz 2.5 kHz and zeros at 15 Hz, 150 Hz, 850 Hz, 2.1 kHz, and 10 kHz. Unfortunately, the technical realization could not be operated in a stable mode and will need further refinement in future.

Bibliography

- [1] C.W. Chou, et al., *Frequency Comparison of Two High-Accuracy Al⁺ Optical Clocks*, PRL **104**, 070802 (2010).
- [2] C. W. Chou, et al., *Optical Clocks and Relativity*, Science, **329**, 1630 (2010).
- [3] T. Rosenband, et al., *Frequency Ratio of Al⁺ and Hg⁺ Single-Ion Optical Clocks; Metrology at the 17th Decimal Place*, Science **19**, 1808 (2008).
- [4] C.G Parthey, et al., *Improved Measurement of the Hydrogen 1S - 2S Transition Frequency*, Phys. Rev. Lett. **107**, 203001 (2011).
- [5] S. Schiller, et al., *Optical clocks in space*, Nuclear Physics B Proceedings Supplements **166**, 300 (2007).
- [6] P. and F. Riehle, *On Secondary Representations of the Second*, Proc. 20th European Frequency and Time Forum (2006).
- [7] A. Bauch, *Comparison between frequency standards in Europe and the USA at the 10⁻¹⁵ uncertainty level*, Metrologia **43**, 109 (2006).
- [8] A. Matveev, et al., *Using two well-timed hydrogen 1S - 2S measurements to set limits on electron boost Lorentz invariance violation*, in prep.
- [9] S. Weyers, et al., *Uncertainty evaluation of the atomic caesium fountain CSF1 of the PTB*, Metrologia **38**, 343 (2001).
- [10] A. Scheibe, and U. Adelsberger, *Schwankungen der astronomischen Tageslänge und der astronomischen Zeitbestimmung mit den Quarzuhren der Phys.-Techn. Reichsanstalt*, Phys. Z. **37**, 185 (1936).
- [11] A. Scheibe, and U. Adelsberger *Die Gangleistungen der PTR-Quarzuhren und die jährliche Schwankung der astronomischen Tageslänge*, Zeitschrift für Physik **127**, 416 (1950).
- [12] I.I. Rabi, *Radiofrequency spectroscopy*, Richtmyer Memorial Lecture, New York, (1945).

-
- [13] L. Essen and J. Parry, *An Atomic Standard of Frequency and Time Interval: A Caesium Resonator*, Nature **176**, 280, (1955).
- [14] Comptes Rendus de la 13e CGPM (1967/68), 103 (1969).
- [15] M. Takamoto, et al., *An optical lattice clock*, Nature **435**, 321 (2005).
- [16] N. Huntemann, et al., *High-Accuracy Optical Clock Based on the Octupole Transition in $^{171}\text{Yb}^+$* , Phys. Rev. Lett **108**, 090801 (2012).
- [17] F. Riehle, *Frequency Standards - Basics and Applications*, Wiley-VCH Verlag GmbH, Weinheim (2004).
- [18] D. W. Allan, *Statistics of atomic frequency standards*, Proc. IEEE **54**, 221 (1966).
- [19] W. J. Riley, NIST Special Publication 1065 (NIST, Boulder, CO, 2008).
- [20] D.W. Allan and James Barnes, *A modified Allan variance with increased oscillator characterization ability*, Proc. of the 35th Ann. Freq. Control Symposium, 470, (1981).
- [21] ISO, *Guide to the Expression of Uncertainty in Measurement*, (International Organization for Standardization, Geneva, Switzerland, 1993).
- [22] E. Rubiola, *On the measurement of frequency and of its sample variance with high-resolution counters*, Rev. Sci. Instrum. **76**, 054703, (2005).
- [23] S.T. Dawkins, et al., *Considerations on the Measurement of the Stability of Oscillators with Frequency Counters*, IEEE Trans. Ultrason. Ferroelectr. Freq. Control **54**, 918, (2007).
- [24] Th. Udem, et al., *Accuracy of Optical Frequency Comb Generators and Optical Frequency Interval Divider Chains*, Opt. Lett. **23**, 1387 (1998).
- [25] A. Bauch, *Caesium atomic clocks: function, performance, and applications*, Measurement Science and Technology **14**, 1159 (2003).
- [26] Ch. Affolderbach, et al., *Experimental Demonstration of a Compact and High-Performance Laser-Pumped Rubidium Gas Cell Atomic Frequency Standard*, IEEE Transactions on Instr. and Meas. **55**, 429 (2006).
- [27] W. Demtröder, *Laser Spectroscopy*, Springer-Verlag, Berlin, Heidelberg, New York, ISBN 3-540-52601-3, (1991).
- [28] M. A. Lombardi, et al., *NIST Primary Frequency Standards and the Realization of the SI Second*, Measure **2**, 74, (2007).

- [29] A. Bauch, *The PTB primary clocks CS1 and CS2*, Metrologia **42**, 43 (2005).
- [30] K. Gibble and S. Chu, *Laser-Cooled Cs Frequency Standard and a Measurement of the Frequency Shift due to Ultracold Collisions*, Phys. Rev. Lett. **70**, 1771 (1993).
- [31] A. Clarion, et al., *A cesium fountain frequency standard: Recent results*, IEEE Transactions on Instr. and Meas. **44**, 128 (1995).
- [32] R. Wynands, S. Weyers, *Atomic Fountain Clocks*, Metrologia **42**, 64 (2005).
- [33] C. Vian, et al., *BNM-SRYTE Fountains: Recent Results*, IEEE Transactions on Instr. and Meas. **54**, 833 (2005).
- [34] F. Levi, et al., *IEN-CsF1 Accuracy Evaluation and Two-Way Frequency Comparison*, IEEE Transactions on Ultrasonics, Ferroelectrics, and Frequency Control **51**, 1216 (2004).
- [35] S. Weyers, et al., *The atomic caesium fountain CSF1 of PTB*, Proc. of the 6th Symposium on Frequency Standards and Metrology, ISBN 981-02-4911-X, World Scientific, Singapore, 64 (2001).
- [36] F. Levi, et al., *Reduction of the Cold Collisions Frequency Shift in a Multiple Velocity Fountain: A New Proposal*, IEEE Transactions on Ultrasonics, Ferroelectrics, and Frequency Control **48**, 847, (2001).
- [37] G. Santarelli, et al., *Quantum Projection Noise in an Atomic Fountain: A High Stability Cesium Frequency Standard*, Phys. Rev. Lett. **82**, 4619 (1999).
- [38] C.R. Locke, et al., *Design techniques and noise properties of ultrastable cryogenically cooled sapphire-dielectric resonator oscillators*, Rev. Sci Instr. **79**, 051301 (2008).
- [39] J.G. Hartnett, and N.R. Nand, *Ultra-Low Vibration Pulse-Tube Cryocooler Stabilized Cryogenic Sapphire Oscillator With 10^{-16} Fractional Frequency Stability*, IEEE Trans. on Microwave Theory and Techniques **10**, 420, (2010).
- [40] Y. Y. Jiang, et al., *Making optical atomic clocks more stable with 10^{-16} -level laser stabilization*, Nature Photonics **5**, 158 (2011).
- [41] T. M. Fortier, et al., *Generation of ultrastable microwaves via optical frequency division*, Nature Photonics **5**, 425 (2011).
- [42] H. Katori, *Optical lattice clocks and quantum metrology*, Nature Photonics **5**, 203 (2011).

- [43] W.D. Phillips, *Laser Cooling and Trapping of Neutral Atoms*, Nobel Lecture, (1987).
- [44] Th. Udem et al., *Optical Frequency Metrology*, Nature **416**, 233 (2002).
- [45] G. Wilpers, et al., Absolute frequency measurement of the neutral ^{40}Ca optical frequency standard at 657 nm based on micro-Kelvin atoms, *Metrologia* **44**, 146 (2007).
- [46] J. A. Sherman and C. W. Oates, *Stability limits of an optical frequency standard based on free Ca atoms*, arXiv:1108.3293v1 [physics.atom-ph] (2011).
- [47] M. Takamoto, et al., *Frequency comparison of optical lattice clocks beyond the Dick limit*, Nature Photonics **5**, 288 (2011).
- [48] G. Wilpers, *Optical Clock with Ultracold Neutral Atoms*, Phys. Rev. Lett. **89**, 230801 (2002).
- [49] R. Li, et al., *Improved accuracy of the NPL-CsF₂ primary frequency standard: evaluation of distributed cavity phase and microwave lensing frequency shifts*, *Metrologia* **48**, 283 (2011).
- [50] A. D. Ludlow, et al., *Sr Lattice Clock at 1×10^{-16} Fractional Uncertainty by Remote Optical Evaluation with a Ca Clock*, Science **319**, 1805 (2008).
- [51] L. Lorini, et al., *Recent atomic clock comparisons at NIST*, Eur. Phys. J. Special Topics **163**, 19 (2008).
- [52] D. Piester, et al., *Special Topic: 50 years of time dissemination with DCF77*, Special Issue / PTB-Mitteilungen **119**, 217 (2009).
- [53] <http://www.bipm.org/en/scientific/tai/>
- [54] <http://www.iag-aig.org>
- [55] H. Drewes, *Science rationale of the Global Geodetic Observing System (GGOS)*. Dynamic Planet, Internat. Ass. of Geodesy Symposia **130**, Eds: P. Tregoning, C. Rizos, Springer, 703 (Berlin 2007).
- [56] <http://www.fs.wettzell.de/>
- [57] J.-P. Uzan, *The fundamental constants and their variation: observational status and theoretical observations*, Rev. Mod. Phys. **75**, 403 (2003).
- [58] J. K. Webb, et al., *Search for Time Variation of the Fine Structure Constant*, Phys. Rev. Lett. **82**, 884 (1999).

- [59] E. Peik, *Laboratory Limits on Temporal Variations of Fundamental Constants: An Update*, arXiv:physics/0611088v1 [physics.atom-ph], (2006).
- [60] T. M. Fortier, et al., *Precision Atomic Spectroscopy for Improved Limits on Variation of the Fine Structure Constant and Local Position Invariance*, Phys. Rev. Lett. **98**, 070801 (2007).
- [61] J. Alfaro, et al., *Loop quantum gravity and light propagation*, Phys. Rev. D **65**, 103509 (2002).
- [62] L. Cacciapuoti, and Ch. Salomon, *Space clocks and fundamental tests: The ACES experiment*, Eur. Phys. J. Special Topics **172**, 57 (2009).
- [63] R.F.C. Vessot, et al., *Test of Relativistic Gravitation with a Space-Borne Hydrogen Maser*, Phys. Rev. Lett. **45**, 2081 (1980).
- [64] M. A. Lombardi, et al. *Time and Frequency Measurements Using the Global Positioning System*, Cal. Lab. Int. J. Metrology **8**, 26 (2001).
- [65] <http://www.glonass-ianc.rsa.ru/en/>
- [66] http://www.esa.int/esaNA/SEM1MURMD6E_galileo_0.html
- [67] E. Peik and A. Bauch, *More Accurate Clocks - What are they Needed for?*, Special Issue / PTB-Mitteilungen **119**, pp.18 (2009).
- [68] J. Levine, *Time and frequency distribution using satellites*, Rep. Prog. Phys. **65**, 1119 (2002).
- [69] <http://tf.nist.gov/time/twoway.htm>
- [70] D. Piester and H. Schnatz, *Novel Techniques for Remote Time and Frequency Comparisons*, Special Issue / PTB-Mitteilungen **119**, pp.33 (2009).
- [71] D. Piester, et al., *Remote atomic clock synchronization via satellites and optical fibers*, Adv. Radio Sci. **9**, 1 (2011).
- [72] T. Feldmann, *Advances in GPS based Time and Frequency Comparisons for Metrological Use*, Dissertation, Leibniz Universität Hannover (2011).
- [73] M. Schioppo, *Development of a transportable laser cooled strontium source for future applications in space*, Proceedings of EFTF, (2010).
- [74] Ph. Laurent, et al., *Design of the cold atom PHARAO space clock and initial test results*, Appl. Phys. B **84**, 683 (2006).

-
- [75] J. Guéna, et al., *Recent Atomic Fountain Clock Comparisons at LNE-SYRTE*, Frequency Control and the European Frequency and Time Forum, 2011 Joint Conference of the IEEE International (San Francisco, 2011).
- [76] M. Chwalla, et al., *Absolute frequency measurement of the $^{40}\text{Ca}^+ 4s^2S_{1/2} - 3d^2D_{5/2}$ clock transition*, Phys. Rev. Lett. **102**, 023002 (2009).
- [77] S. M. Foreman, et al., *Remote transfer of ultrastable frequencies via fiber networks*, Rev. Sci. Instr. **78**, 021101 (2007).
- [78] O. Lopez, et al., *Fiber frequency dissemination with resolution in the 10^{-18} range*, Eur. Phys. J. D **48**, 35 (2008).
- [79] G. Grosche, et al., *Transmission of an Optical Carrier Frequency over a Telecommunication Fiber Link*, in Conference on Lasers and Electro-Optics, paper CMKK1, (2007).
- [80] G. Marra, et al., *High-stability microwave frequency transfer by propagation of an optical frequency comb over 50 km of optical fiber*, Opt. Lett., **35**, 1025 (2010).
- [81] K.W. Holman, et al., *Remote transfer of a high-stability and ultralow-jitter timing signal*, Opt. Lett. **30**, 1225 (2005).
- [82] M. Musha, et al., *Coherent optical frequency transfer over 50-km physical distance using a 120-km-long installed telecom fiber network*, Opt. Express **16**, 16459 (2008).
- [83] G. Grosche, et al., *Optical frequency transfer via 146 km fiber link with 10-19 relative accuracy*, Opt. Lett. **34**, 2270 (2009).
- [84] H. Jiang, et al. *Long-distance frequency transfer over an urban fiber link using optical phase stabilization*, J. Opt. Soc. Am. B **25**, 2029 (2008).
- [85] O. Terra, et al., *Brillouin amplification in phase coherent transfer of optical frequencies over 480 km fiber*, Opt. Express **18**, 16102 (2010).
- [86] 18. Yamaguchi et al., *Direct Comparison of Distant Optical Lattice Clocks at the 10^{-16} Uncertainty*, Appl. Phys. Express **4**, 082203 (2011).
- [87] H. Schnatz, et al., *Phase-Coherent Frequency Comparison of Optical Clocks Using a Telecommunication Fiber Link*, IEEE Trans on UFF **57**, 175 (2010).
- [88] F. Tauser, et al., *Amplified femtosecond pulses from an Er: fiber system: Nonlinear pulse shortening and self-referencing detection of the carrier-envelope phase evolution*, Opt. Express **11**, 594 (2003).

- [89] T. Wilken et al., *Low Phase Noise 250 MHz Repetition Rate Fiber fs Laser for Frequency Comb Applications*, in 2007 Conference on Lasers and ElectroOptics, CLEO (2007).
- [90] P. Kubina, et al., Long term comparison of two fiber based frequency comb systems, *Opt. Express* **13**, 904 (2005).
- [91] T. Kessler, et al., *A sub-40 mHz linewidth laser based on a silicon single-crystal optical cavity*, arXiv:1112.3854v2 [physics.optics] (2011).
- [92] D. Leibrandt, et al., *Spherical Reference Cavities for Ultra-Stable Lasers in Non-Laboratory Environments*, *Opt. Express* **19**, 3471 (2011).
- [93] M. Notcutt, et al., *Simple and compact 1-Hz laser system via an improved mounting configuration of a reference cavity*, *Opt. Lett.* **30**, 1815 (2005).
- [94] J. Alnis, et al., *Subhertz linewidth diode lasers by stabilization to vibrationally and thermally compensated ultralow-expansion glass Fabry-Perot cavities*, *Phys. Rev. A* **77**, 053809 (2008).
- [95] T. Legero, et al., in prep.
- [96] <http://www.itu.int/rec/T-REC-G.652-200911-I/en>
- [97] G. B. Hocker, *Fiber-optic sensing of pressure and temperature*, *Appl. Optics* **18**, 1445 (1979).
- [98] http://saekular.pik-potsdam.de/2007_de
- [99] L. S. Ma, et al., *Delivering the same optical frequency at two places: accurate cancellation of phase noise introduced by an optical fiber or other time-varying path*, *Opt. Lett.* **19**, 1777, (1994).
- [100] P. A. Williams, et al., *High-stability transfer of an optical frequency over long fiber-optic links*, *Opt. Soc. Am. B* **25**, 1284, (2008).
- [101] E. Rubiola, private communication (2010).
- [102] D. Derrickson, *Fiber Optic- Test and Measurement*, Prentice Hall PTR (1997).
- [103] G.P. Agrawal, *Fiber Optic- Communication Systems*, John Wiley & Sons (2002).
- [104] R. Tkach, and A. Chraplyvy, *Fibre Brillouin amplifiers* *Opt. Quantum Electron.* **21**, 105 (1989).
- [105] H. Jiang, et al., *An agile laser with ultra-low frequency noise and high sweep linearity*, *Opt. Express* **18**, 3284 (2010).

-
- [106] K. Predehl et al., A 920 km Optical Fiber Link for Frequency Metrology at the 19th Decimal Place, accepted for publishing in Science (2012).
- [107] B. Bernhardt, et al., *Implementation and characterization of a stable optical frequency distribution system* Opt. Express **17**, 16849 (2009).
- [108] A. Pape, et al., *Long-distance remote comparison of ultrastable optical frequencies with 10^{-15} instability in fractions of a second*, Opt. Express **18**, 21477 (2010).
- [109] M. Niering et al., *Measurement of the Hydrogen 1S- 2S Transition Frequency by Phase Coherent Comparison with a Microwave Cesium Fountain Clock*, Phys. Rev. Lett. **84**, 5496 (2000).
- [110] M. Fischer, et al., *New Limits on the Drift of Fundamental Constants from Laboratory Measurements*, Phys. Rev. Lett. **92**, 230802 (2004).
- [111] Ch. G. Parthey, *Precision spectroscopy on atomic hydrogen*, PhD thesis (2011).
- [112] F. Biraben, et al., *The Hydrogen Atom. Precision Physics of Simple Atomic Systems*, S. G. Karshenboim, F. S. Pavone, G. F. Bassani, M. Inguscio, and T. W. Hänsch, eds., Berlin: Springer, 17 (2001).
- [113] U.D. Jentschura, et al., *Hydrogen-deuterium isotope shift: From the 1S- 2S-transition frequency to the proton-deuteron charge-radius difference*, Phys. Rev. A. **83**, 042505 (2011).
- [114] N. Kolachevsky, et al., *Measurement of the 2S Hyperfine Interval in Atomic Hydrogen*, Phys. Rev. Lett. **102**, 213002 (2009).
- [115] R. Pohl, et al., *The size of the proton*, Nature **466**, 213 (2010).
- [116] J. J. Balmer, *Notiz über die Spectrallinien des Wasserstoffs*, Annalen der Physik **261**, 80, (1885).
- [117] N. Bohr, *On the Constitution of Atoms and Molecules, Part I*, Philosophical Magazine **26**, 1 (1913).
- [118] W. E. Lamb, and R. C. Retherford, *Fine Structure of the Hydrogen Atom by a Microwave Method* Phys Rev. **72**, 241 (1947).
- [119] M. Fischer, *Höchstauflösende Laserspektroskopie an atomarem Wasserstoff*, PhD thesis, (2004).
- [120] T.W. Hänsch, et al., *Doppler-Free Two-Photon Spectroscopy of Hydrogen 1S-2S*, Phys. Rev. Lett. **34**, 307 (1975).

BIBLIOGRAPHY

- [121] V.A. Kostelecky and S. Samuel, *Spontaneous breaking of Lorentz symmetry in string theory*, Phys. Rev. D **39**, 683 (1989).
- [122] R. Gambini and J. Pullin, *Nonstandard optics from quantum space-time*, Phys. Rev. D **59**, 124021 (1999).
- [123] B. Altschul, *Testing Electron Boost Invariance with 1S-2S Hydrogen Spectroscopy*, Phys. Rev. D **81**, 041701 (2010).
- [124] Th. Middelmann et al., *Tackling the blackbody shift in a strontium optical lattice clock*, IEEE T. Instrumentation and Measurement **60**, 2550 (2011).
- [125] W. Lee, et al., *The uncertainty associated with the weighted mean frequency of a phase-stabilized signal with white phase noise*, Metrologia **47**, 24, (2010).
- [126] T. Musha, *1/f fluctuations in biological systems*, Proceedings of the Sixth International Conference on Noise in Physical Systems, 143 (1981).
- [127] R.T. Baillie, *Long memory processes and fractional integration in econometrics*, J. Economet. **73**, 5 (1996).
- [128] R.F. Voss, and J. Clarke, *1/f noise in music and speech*, Nature **258**, 317 (1975).
- [129] L.M. Ward, *Dynamical Cognitive Science*, Cambridge, MA: MIT Press (2002).
- [130] *Characterization of Frequency and Phase Noise, Report of the International Radio, Consultative Committee (C.C.I.R) 580*, 142 (1986).
- [131] G.P. Agrawal, *Lightwave Technologies*, John Wiley & Sons (2005).
- [132] L.E. Richter, et al., *Linewidth determination from self-heterodyne measurements with subcoherence delay times*, IEEE Quant. Electr. **22**, 2070 (1986).
- [133] F. Keffian, et al., *Ultralow-frequency-noise stabilization of a laser by locking to an optical fiber-delay line*, Opt. Lett. **34**, 914 (2009).
- [134] T.W. Hänsch, *Nobel Lecture: Passion for precision*, Rev. of mod. physics, **78**, (2006).
- [135] R. Holzwarth, et al., *Optical Frequency Synthesizer for Precision Spectroscopy*, Phys. Rev. Lett. **85**, 2264, (2000).
- [136] L.-S. Ma, et al., *A New Method to Determine the Absolute Mode Number of a Mode-Locked Femtosecond-Laser Comb Used for Absolute Optical Frequency Measurements*, IEEE J. Sel. Top. Quant. Elec. **9**, 1066 (2003).

- [137] Scott A. Diddams, et al., *Direct Link between Microwave and Optical Frequencies with a 300 THz Femtosecond Laser Comb*, Phys. Rev. Lett. **84**, 5103, (2000).
- [138] J. Millo, et al., *Ultralow noise microwave generation with fiber-based optical frequency comb and application to atomic fountain clock*, Appl. Phys. Lett. **94**, 141105 (2009).
- [139] F.M. Gardner, *Phaselock Techniques* John Wiley & Sons (2005).
- [140] E. Black *An introduction to Pound-Drever-Hall laser frequency stabilization* Am. J. Phys. **69**, 79 (2001).
- [141] A. Abromovici, et al., *LIGO: The laser interferometer gravitational-wave observatory*, Science **256**, 325 (1992).
- [142] O. Terra, *Dissemination of ultra-stable optical frequencies over commercial fiber networks*, PhD thesis (2010).
- [143] B. S. Sheard et al., *Laser frequency stabilization by locking to a LISA arm*, Phys. Lett. A **320**, 9 (2003).
- [144] O.Lopez, et al., *Cascaded multiplexed optical link on a telecommunication network for frequency dissemination*, Optics Express **18**, 16849 (2010).
- [145] J. Frisch, et al., *A high stability, low noise RF distribution system*, Proc. 2001 Particle Accelerator Conf. **2**, 816 (2001).
- [146] W. Shillue, *Fiber distribution of local oscillator for Atacama Large Millimeter Array*, Proc. Optical Fiber Communication Conf. / National Fiber Optic Engineers Conf., San Diego, CA, 1 (2008).
- [147] K. H. Sato, et al., *Application of phase-stabilized optical fiber in transmission of reference and IF signals in VLBI observation*, IEEE Trans. Instrum. Meas. **41**, 385 (1992).
- [148] M. Calhoun, et al., *Stable photonic links for frequency and time transfer in the Deep Space Network and antenna arrays*, Proc. IEEE **95**, 1931 (2007).
- [149] S . W. Lee, et al., *A study on the common-view and all-in-view GPS time transfer using carrier-phase measurements*, Metrologia **45**, 156 (2008).

List of Publications

1. K. Predehl, G. Grosche, S. M. F. Raupach, S. Droste, Th. Legero, J. Alnis, O. Terra, Th. Udem, T.W. Hänsch, R. Holzwarth, and H. Schnatz *A 920 km optical fiber link for frequency metrology at the 19th decimal place*, accepted for publication in Science (2012).
2. M. Lezius, K. Predehl, W. Stöwer, A. Türlér, M. Greiter, Ch. Hoeschen, P. Thirolf, W. Assmann, D. Habs, A. Prokofiev, C. Ekström, T. W. Hänsch, and R. Holzwarth *Radiation induced absorption in rare-earth doped optical fibers*, IEEE Trans. on Nucl. Sci. **PP**, 1 (2012).
3. A. Matveev, C.G. Parthey, K. Predehl, J. Alnis, A. Beyer, R. Holzwarth, Th. Udem, T. Wilken, N. Kolachevsky, M. Abgrall, D. Rovera, C. Salomon, Ph. Laurent, G. Grosche, Th. Legero, H. Schnatz, S. Weyers, B. Altschul, and T. W. Hänsch *Using two well-timed hydrogen 1S-2S measurements to set limits on electron boost Lorentz invariance violation*, in preparation
4. C.G. Parthey, A. Matveev, J. Alnis, A. Beyer, R. Pohl, K. Predehl, Th. Udem, N. Kolachevsky, M. Abgrall, D. Rovera, C. Salomon, P. Laurent, and T. W. Hänsch *Precision spectroscopy on atomic hydrogen*, Proc. SPIE **8132**, 813202 (2011).
5. C.G. Parthey, A. Matveev, J. Alnis, B. Bernhardt, A. Beyer, R. Holzwarth, A. Maistrou, R. Pohl, K. Predehl, Th. Udem, T. Wilken, N. Kolachevsky, M. Abgrall D. Rovera, C. Salomon, P. Laurent, and T.W. Hänsch, *Improved measurement of the hydrogen 1S-2S transition frequency*, Phys. Rev. Lett. **107**, 203001 (2011).
6. A. Pape, O. Terra, J. Friebe, M. Riedmann, T. Wübbena, E. M. Rasel, K. Predehl, T. Legero, B. Lipphardt, H. Schnatz, and G. Grosche *Long-distance remote comparison of ultra stable optical frequencies with 10^{-15} instability in fractions of a second*, Opt. Expr. **18**, 2021477 (2010).
7. H. Schnatz, O. Terra, K. Predehl, T. Feldmann, T. Legero, B. Lipphardt, U. Sterr, G. Grosche, T. W. Hänsch, R. Holzwarth, T. Udem, Z. H. Lu, L. J. Wang, W. Ertmer, J. Friebe, A. Pape, E. - M. Rasel, M. Riedmann, and T. Wübbena *Phase-coherent frequency comparison of optical clocks using a telecommunication fiber link*, Trans. on Ultra. Ferr. & Freq. Contr. **57**, 175 (2010).

8. G. Grosche, O. Terra, K. Predehl, R. Holzwarth, B. Lipphardt und H. Schnatz *Measurement noise floor for a long-distance optical carrier transmission via fiber*, PROC 7th Symp. of Freq. Standards & Metrology, 432 (2009).
9. O. Terra, G. Grosche, K. Predehl, R. Holzwarth, Th. Legero, U. Sterr, B. Lipphardt, H. Schnatz *Phase-coherent comparison of two optical frequency standards over 146 km using a telecommunication fiber link*, Appl. Phys. B **97**, 541 (2009).
10. G. Grosche, O. Terra, K. Predehl, R. Holzwarth, B. Lipphardt, F. Vogt, U. Sterr, and H. Schnatz *Optical frequency transfer via 146 km fiber link with 10^{-19} relative accuracy*, Opt. Lett. **34**, 2270 (2009).
11. M. Zimmermann, Ch. Gohle, P. Fendel, M. Herrmann, K. Predehl, B. Bernhardt, B. Stein, D. Walker, R. Holzwarth, Th. Udem, and T. W. Hänsch, *Optische Frequenzkämme und der Physiknobelpreis 2005*, Praxis der Naturwiss., Physik in der Schule **55**, 38 (2006).

Conference Contributions

- 2011 ESA workshop on Optical Clocks, Trani, Italy
- 2011 Workshop on Astrophysics, Clocks, and Fundamental Constants, Bad Honnef, Germany
- 2011 IEEE International Frequency Control Symposium & European Time and Frequency Forum (IFCS), San Francisco, USA
- 2011 Spring congress of the German Physics Society, Dresden (DPG), Germany
- 2010 Conference on Lasers and Electro- Optics (CLEO), San Jose, USA
- 2010 European Forum for Time and Frequency (EFTF), Noordwijk, Netherlands
- 2009 Conference on Lasers and Electro- Optics (CLEO), Baltimore, USA
- 2009 Spring congress of the German Physics Society (DPG), Hamburg, Germany
- 2006 Spring congress of the German Physics Society (DPG), Düsseldorf, Germany

Awards

- 2011 IEEE International Frequency Control Symposium & European Time and Frequency Forum student paper competition award for the paper *Absolute Frequency Measurement of the 1S-2S Transition in Atomic Hydrogen Using a 900 km Remote Frequency Reference*

- 2010 European Forum for Time and Frequency student paper competition finalist for the paper *A 900 km Fiber Link for the Dissemination of Optical References from PTB to MPQ*

Acknowledgments

So many people have contributed to this project! Some of you directly and some in a more subtle way. Looking back, every single one of you was invaluable.

First I would like to thank you, Professor Hänsch, for the confidence you placed in my skills to entrust me such a (literally) big project (I think we both were doubtful every now and then if this was a good idea). After all, I have to say that this was a great experience for me that I enjoyed a lot.

Ronald Holzwarth has supervised my PhD. Thank you, Ronald, for keeping the big picture in mind when the rest of us struggled with the nasty details of the experiment. It was more than once that we briefly discussed things that had kept me busy for days and your 'why not try... ?'-suggestion provided the right solution. Your energy to get the best out of your professional as well as your private life is incredible and inspiring.

Harald Schnatz from PTB was my backup supervisor and has become a friend, too. Together we installed (/retrieved/again installed) a major part of the link equipment and spent a lot of time on German autobahns. Harald, I like to thank you for teaching me the dirty tricks of PLL electronics and for your endurance in the lab. Without you, the link would probably still not be running. Also, I greatly appreciate your and Christina's warm hospitality during my stays in Braunschweig.

Thomas Udem is not only an excellent physicist who never gets tired understanding and explaining the world and the physics behind. He is also a reliable partner for all kinds of mountain activities such as back-country skiing, rock climbing, and cycling. I appreciate your passionate contributions to the 'how to perform a frequency measurement' discussion a lot. 10^{-19} would have never been possible without your careful analysis.

Gesine Grosche is the principal investigator of the link experiment at PTB site. Gesine, you have a great curiosity for how things work and your questions (Moment, Moment, nun mal langsam...) usually revealed the end of my own understanding quite quickly. I cannot remember one single discussion with you that did not teach me something new about our experiment.

Stefan Droste is the 'new' PhD student in the MPQ link team. Stefan, it was an amazingly short time that it took you to get an overview of the setup. Only after a few weeks you were able to acquire and evaluate the data on your own. I think that Ronald hired exactly the right person to continue the project efficiently. I wish you great success with the future experiments. I also enjoyed hilarious coffee breaks, movie nights, and whiskey tastings with you and the other members of the party office D0.27, Guido Saathoff and Andy Vernaleken.

Osama Terra started his PhD together with me and though his main project was to set up the link from PTB to Hanover, we discussed and encouraged each other a lot, especially when designing the fiber interferometer for the Doppler-noise cancellation.

After he left, Sebastian Raupach has joined the link team at PTB site as a post-doc. Sebastian, you started right after the tedious hydrogen measurement campaign in November bringing enthusiasm and new ideas exactly when the rest of us was entirely burned out. You forced us back to the link characterization and together we could increase the measurement time in which we did not lose one single optical cycle to several hours. Of course, I also wish you lots of very, very small numbers in future link experiments.

The link project would have never been realized without the fruitful collaboration with the German Research Network DFN and Gasline GmbH. In particular, I would like to emphasize the encouragement of Hans-Josef Duda, Andreas Kaiser, Carsten Werner-Rakowsky, Peter Beeking, and all team members of DFN Erlangen and Leipzig.

Christian Parthey came to MPQ's hydrogen team, saw, and won (including the hearts of all female physicists in the group). Together, we have coordinated the Nov 2010 Hydrogen/Link measurements. Christian, I enjoyed your strong and cheerful personality, the climbing trips (even the one to Blaueishütte!), the beers, the slacklining, the never-ending tofu jokes and the discussions of how to keep a long-distance relationship alive. I wish you and Uli all the best for your future and I expect both of you to be back in Munich as soon as I celebrate my defense.

The Russian part of the hydrogen team consists of Arthur Matveev and Nikolai Kolachevsky. Arthur, you have been available 24/7 to answer my questions about the hydrogen experiment and you patiently corrected my poor attempts to refresh my Russian. Nikolai, I really like your smart sense of humor, your anecdotes, and your creativity to improvise a measurement when components are missing. It has been lot of fun setting up the stable laser system with you.

Together with Nikolai, Janis Alnis has taught me how to set up a stable laser system. He has been working on the hydrogen experiment for many years and has a great knowledge of all kinds of electronics as well as an impressive patience to get them running. Thank you, Janis, for being so supportive, especially in optimizing the locking electronics for the link.

Axel Bayer has joined the hydrogen team as a master student and for some reason decided to do his PhD there as well. Axel, you have shown great endurance and enthusiasm and I really hope that you and the other hydrogen guys will break the 10^{-16} threshold soon. Thank you for helping us during the November measurements and for preventing me from falling into bad habits such as, for example, following the lately strongly increased desire for smoking.

I further like to thank Andy Thaller and Rainer Scheunemann from Menlo Systems GmbH for (long-term!) support with the EDFA systems, and especially with the remote control.

My former lab mates Tobias Wilken and Tilo Steinmetz regularly had to spent a lot of time on the phone¹ trying to perform remote diagnostics on my experiment whenever I was on the road without seeing a signal. Thank you so much for your patience and also for your good, solid taste in music! Tobias, I enjoyed our various trips to the alps be it in summer or in winter and be it with shoes or without.

This experiment would have never been realized without the competence of our technicians Karl *Charlie* Linner and Wolfgang Simon as well as our electronics engineer Helmut Brückner. Furthermore, the whole group would probably collapse without the diligence of our secretaries Ingrid Hermann (MPQ) and Gabriele Gschwendtner (LMU). Thank you all so much for your help!

The Hänsch group in general is a bunch of great people to work with. I greatly appreciate your supportive attitude, the team spirit, and the well organized repertoire of spare-time activities. Two Hommelhoff-thumbs up for you, guys! Especially Johannes Hoffrogge, Tobias Nebel, and Elisabeth Peters I have taken into my heart.

I also like to thank my dear office mate Birgitta *Gitti* Bernhardt whom I have already known from my studies at LMU. For the last ten (!) years we have gone through good times and trough bad times together. We have discussed physics, boys, movies, and the latest fashion. Together, we have produced a couple of legendary MPQ Christmas movies which is something I will always keep in a good memory.

¹wireless since Tobias got in rage with the too short cable.

Albert Schliesser and Christoph *Chris G.* Gohle never hesitated to provide extended brain capacity whenever I got stuck with physical problems. I hope we stay in contact for more 'late night discussions' (or should I better say 'percussions'?).

During the course of this project, I had the chance to discuss with a variety of very smart persons from all around the world. In particular, I would like to thank Enrico Rubiola, Giorgio Santarelli, Burghard Lipphardt, Uwe Sterr, and Fritz Riehle for teaching me their understanding of frequency metrology.

There is a small number of people that have strongly contributed to this work by mainly providing emotional support. First, I would like to thank my dear girls Susanne, Helene, Sara, and Nana. You will always reset my brain back in perspective whether I feel bad or whether I feel too good. Your friendship is just priceless!

I am further in the lucky position to have my parents Luise and Peter and my sister Sabine living nearby. Their advice and encouragement have enabled all this. Be it history lessons accompanied with fancy food or a place to sleep nearby the lab whenever it got late - I really appreciate having you around!

Jens, thank you for the great support and for bringing so much joy to my life. I am still not sure if I like the adventurous part but I definitely like the feeling of having survived so far.

